5-24-2010

Determination of the Structural and Functional Mechanisms of Perfluorocarbon-based Nanoemulsion Particle Interactions with Model Biomembrane Systems

Sun Joo Lee
Washington University in St. Louis

WASHINGTON UNIVERSITY IN ST. LOUIS

Division of Biology and Biomedical Sciences

Department of Biochemistry and Molecular Biophysics

Thesis Examination Committee:
Nathan A. Baker, Chair
Paul H. Schlesinger, Chair
Elliot L. Elson
Guy M. Genin
Katherine A. Henzler-Wildman
Jay W. Ponder
Samuel A. Wickline

DETERMINATION OF THE STRUCTURAL AND FUNCTIONAL

MECHANISMS OF PERFLUOROCARBON-BASED NANOEMULSION

PARTICLE INTERACTIONS WITH MODEL BIOMEMBRANE SYSTEMS

by

SUN JOO LEE

A dissertation presented to the Graduate School of Arts and Sciences
of Washington University in partial fulfillment of the
requirements for the degree of

DOCTOR OF PHILOSOPHY

December 2010
Saint Louis, Missouri

ABSTRACT OF THE DISSERTATION

Determination of the Structural and Functional Mechanisms of

Perfluorocarbon-based Nanoemulsion Particle Interactions with Model

Biomembrane Systems

by

SUN JOO LEE

Doctor of Philosophy in Biophysics

Washington University in St. Louis, 2010

Research Advisor: Professor Nathan A. Baker

Perfluorocarbon based nanoemulsion particles (PFC-NEPs) are very small sized ($\sim$ 250 nm in diameter) greasy droplets that are enclosed by emulsifying phospholipid monolayer. PFC-NEPs have been extensively developed for target-specific delivery of therapeutic agents such as imaging agents and drug molecules. Because of the extremely small sizes of PFC-NEPs and fluid nature of their surface, the structure of these particles at atomic resolutions has yet to be determined by experimental approaches. The aim of this thesis is to determine the atomistic structure of PFC-NEP interfaces with a particular focus on their interaction with model target bilayers. The goal of this work is to help understand the molecular mechanisms for PFC-NEP cargo binding and delivery. Such understanding will enable the rational design of PFC-NEPs for optimal delivery and eventually lay a foundation to customize the particles for delivery of specific cargo molecules.

To achieve this goal, we have used molecular dynamics (MD) simulations at both atomistic and coarse-grained levels using in-house force field parameters developed for a perfluorocarbon molecule that forms the emulsion core. By employing atomistic simulations, the PFC-NEP interface structure was determined in the absence and presence of a model cargo. The interface structure featured the intercalation of the PFC molecules into the emulsifying monolayer and differential cargo binding to the PFC-NEP interface as a consequence of the intercalation, which expressed the need to modulate the level of mixing of PFC with the emulsifying monolayer for cargo binding to PFC-NEPs. Coarse-grained MD simulations have been employed to test a proposed "hemifusion" mechanism for PFC-NEP delivery of cargo to target bilayers. Our simulations showed that PFC-NEP and liposome particles fused after encounter; distinct molecular details were observed from the fusion mechanism between two bilayers.

This thesis research has not only provided the detailed structure to elucidate molecular mechanisms for cargo binding and delivery but also laid a foundation to decipher the correlation between the structure and function of PFC-NEPs for more systematic studies in the future.

Acknowledgments

<div align="right">SUN JOO LEE</div>

Washington University in Saint Louis
December 2010

This dissertation is dedicated to my parents

Byung-Hee Lee and Tae-Sup Jung.

Contents

List of Tables

List of Figures

Chapter 1

Background and Introduction

The foundation of disease diagnosis, treatment, and prevention has been changed by the application of broad spectra of nanoscale technologies. These nanoscale technologies involve the generation, characterization, and optimization of so-called nanoparticles, in the nanometer scale size range (often $200 \sim 300$ nm or smaller). These small-sized particles can act as biological mimetics, biomaterials, sensors, and vectors for delivery of a variety of substances to specific biological targets. Nanomedicine promises high resolution imaging and efficient treatment by enabling target specific delivery of imaging or therapeutic agents, offering advantages over traditional small molecule therapies. However, these promises have been substantially delayed due to the lack of crucial groundwork to decipher physicochemical and physiological processes. Difficulty in obtaining structural details at the molecular level places an obstacle to understanding physicochemical properties.

The molecular-scale details can be obtained through computational methods such as molecular dynamics simulations. However, physicochemical and, in particular, physiological processes span several orders of magnitude in temporal and spatial scales and thus make it difficult to simulate the processes at an atomic resolution within reasonable computation times. Therefore, multi-scale computational methods have been devised to dissect a process into wide range of lengthscales and timescales. The focus of this thesis work is to lay a foundation for application of multi-scale computational methods to understand the molecular details of the structure and functional mechanisms of a specific class of nanoparticles.

1.1 Perfluorocarbon based Nanoemulsion Particles (PFC-NEP)

Perfluorocarbon (PFC) based nanoemulsion particles (PFC-NEPs) are promising platforms for the cellular delivery of imaging and therapeutic agents to specific targets. Numerous successful *in vitro* and *in vivo* applications of these particles for imaging and treatment have been made. PFC-NEPs with ligands against $\alpha_\nu\beta_3$-integrin have been used to image neovasculature upon tumor growth,(1; 2; 3) atherosclerosis,(4; 5; 6) and therapeutic treatment.(7; 8) The particles have been used to track the movement of cells in the body, which will greatly help the development of cellular therapeutics.(9; 10) PFC-NEPs have been also applied to treat tumor,(2; 11) thrombosis,(12) and atherosclerosis.(5; 6) Taking advantage of the dual functionality of PFC-NEPs for imaging and treatment offers great promise for individualized therapeutics by enabling the quantification of the local concentration of therapeutic agents at the intended target.(13) In addition, the application of PFC-NEPs with different perfluorocarbon cores has opened new possibilities for simultaneous detection of multiple epitopes.(14; 10) Despite these successful applications, the underlying molecular mechanisms for the action of these particles are largely unknown.

Cargo loading and delivery across the plasma membrane are the most crucial steps of nanoparticle action and need to be understood at a molecular level as these processes are strongly influenced by the structure of the particles and their constituent molecules. Therefore, in the following sections, introduced are the structure of the PFC-NEPs, their constituent molecules as well as the crucial processes for the actions of PFC-NEPs.

1.1.1 Structure

Nanoscale PFC emulsion droplets are enclosed by a stabilizing phospholipid monolayer with targeting ligands on their surface. as illustrated in Figure 1.1.1.
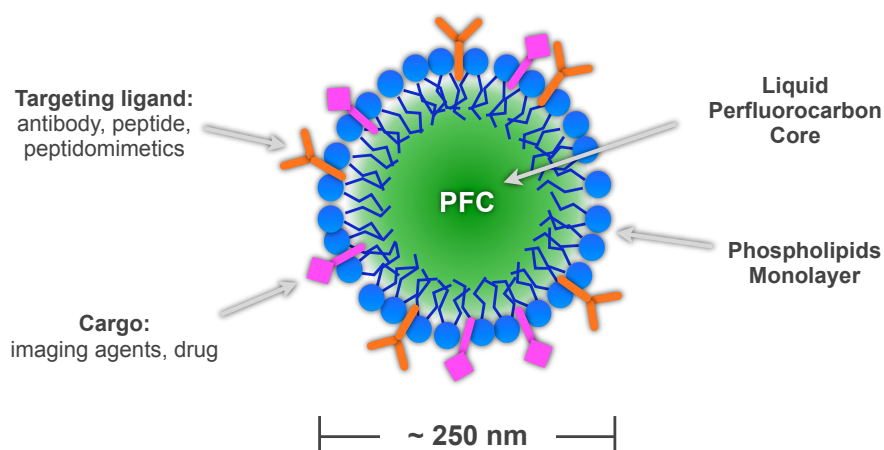
Figure 1.1: A schematic diagram of a multifunctional perfluorocarbon nanoemulsion particle. The perfluorocarbon emulsion core is enclosed by an emulsifying phospholipid monolayer. Targeting ligands are attached to the phospholipids either by covalent or non-covalent bonds. Cargo molecules are attached to the phospholipids, embedded in the monolayer, or dissolved in the emulsion core in the case of strongly hydrophobic molecules. This diagram is adapted from Kaneda et al (13).

Nanoemulsion core

PFCs are synthetic fluids that are structurally the same as hydrocarbons but with fluorine atoms replacing the hydrogen atoms. These compounds can be produced in large amounts with high purity.(15) PFCs are biologically inert, chemically stable, non-degradable, and non-toxic when ingested or inhaled.(16; 13; 17; 18; 19) Strong hydrophobicity is the paramount property of PFCs to form emulsion cores in aqueous solution and to maintain stable emulsions over time. Indeed, PFC-NEPs show very long shelf life (12-months at $4\,^{\circ}$C) with phospholipid emulsifiers.(20)

Perfluorooctylbromide   Perfluorooctylbromide ($C_8F_{17}Br$;PFOB) is a perfluorocarbon with one terminal fluorine atom replaced by bromine and it is under investigation in this thesis as an emulsion core-forming PFC molecule. PFOB is widely used for its following advantageous properties. First, PFOB is rapidly excreted from body with a half-life of 3 days, which is long enough to be practical and short enough to be safe.(17) Second, its low vapor pressure is important for forming stable emulsions

3

with phospholipids. Finally, it can be easily manufactured at high purity.(21) Emulsion particles based on PFOB, with egg-yolk lecithin as the surfactant, are in use for clinical trials to supply oxygen(21; 22) in a biocompatible manner.

Emulsifiers

Bare PFC droplets are thermodynamically unstable. Therefore, emulsion droplets aggregate and coalesce as they minimize energetically unfavorable contacts and eventually form a separate phase. Emulsifiers are molecules with amphipathic characteristics such as phospholipids, surfactants, denatured human serum albumin or synthetic polymer. Emulsifying molecules can stabilize the unstable PFC droplets.(23)

Emulsifiers stabilize small emulsion droplets by reducing the surface tension and by increasing the repulsive force between particles. In the case of PFC-NEPs, the emulsifying layer encloses the hydrophobic PFC cores and generates hydrophilic surface, thereby improving the solubility of these particles.(24; 25) While the physicochemical properties of emulsifiers are critical for the emulsion stability, the surface properties of nanoemulsion particles can be modulated by the interaction of cargo molecules and electrolytes, which will eventually affect the nanoemulsion stability.(25) Therefore, elucidating the interaction of cargo and electrolytes is important in predicting the emulsion stability and selecting emulsifiers.

Phospholipids Phospholipids are used as one possible emulsifier for PFC-NEPs due to the following advantages. Phospholipids can generate smaller emulsion particles because of their strong plasticity and ability to adopt high curvature.(26) Small particle size is an important criterion to offer greater surface area, deeper penetration into tissue, and longer retention in the blood stream.(26; 23; 27) Some sources of phospholipids are egg-yolk and soybean lecithins that have similar phospholipids compositions as human cells: zwitterionic phosphatidylcholine (PC) and phosphatidylethanolamine (PE) in major quantities, lysophosphatidylcholine (LPC) and sphingomyelin (SM) in minor quantities.(28) Therefore, emulsion droplets made with these phospholipids are less likely to trigger an immune responses(21) by providing similar biochemical surface as human cells.(22)

In addition to their role as emulsifiers, the phospholipid monolayer on the surface of PFC-NEP plays important roles in cargo binding, attaching targeting ligands to the NEPs, and cargo delivery. Each of these functional aspects is addressed in the following section in detail. Chapter 3 is devoted to elucidating the surface structure of PFC-NEP, which is very difficult to achieve with current experimental tools due to their small size and inhomogeneous, dynamic nature.

1.1.2 Targeting

Targeting is a unique feature of many nanoparticles. Targeting can be passive or active. Passive targeting takes advantage of the defense mechanism of the host so that the nanoparticles are delivered to phagocytic cells.(29) Active targeting is mediated by target-specific ligands that are attached to the nanoparticle surface either covalently or non-covalently.(13) Biological molecules such as small peptides, monoclonal antibodies, Fab as well as aptamers, peptidomimetics have been used as targeting ligands to provide nanoparticle specificity. Specific ligand-receptor interactions can occur with very low dissociation constant in the nanomolar range.(13)

The surface of particles typically can hold 20-40 monoclonal antibodies or 200-400 small molecule ligands.(29; 30) Multivalent ligand-receptor interactions will enhance not only specificity but also delivery presumably by perturbing membrane structure in a similar manner to SNARE. The conformational changes of SNARE bring the membrane into close proximity and locally perturb the two adjacent lipid bilayers. In doing so, SNARE induces the formation of a fusion pore or neck.(31) Hence, nanoparticle targeting by ligands provides 1) sensitive and selective binding, 2) long residence time at a targeted site, 3) prominent contrast-to-noise enhancement, and 4) accelerated delivery by perturbing membrane structure.(29; 31)

1.1.3 Cargo binding

The interaction of cargo with PFC-NEPs varies based on their physiochemical properties.(25) Amphiphilic or hydrophobic molecules are good candidates for emulsion formulations and most of them may remain at the surface of PFC-NEPs due to

very strong hydrophobicity of PFCs. Therefore, understanding the structure at the PFC-NEP surface enclosed by a phospholipid monolayer will provide insight into how hydrophobic and amphiphilic cargo molecules interact with PFC-NEPs.

Melittin

Melittin has been most extensively studied among many cytolytic peptides that are found as an innate host defense mechanism in invertebrates, vertebrates, and plants.(32; 33) The most crucial function of these peptides is to porate the cell membrane and abolish the low dielectric barrier between extra- and intra-cellular compartments, which eventually leads to cell death. Common biophysical properties of these peptides include: 1) many of the peptides are positively charged, 2) the peptides undergo conformational change from random coil to amphipathic helix upon binding to membrane surface, 3) their pore forming activity is highly cooperative.(32; 33; 34)

Cytolytic peptides have promising potential as an anticancer therapeutic if their premature degradation by peptidase and non-specific cytolytic activity can be controlled. PFC-NEPs have been implemented to resolve these two main obstacles in order for *in vivo* application of melittin, and it was shown to be successful. Soman et al. demonstrated that the melittin AMP could be stably bound to PFC-NEPs without disruption of NEP morphology nor destabilization of the PFC emulsion. Furthermore, they showed that NEP-bound melittin retains its biological activity: it can lyse liposomes and induce apoptosis *in vitro* and, more importantly, significantly reduce tumor size in *in vivo* mouse studies.(35; 11)

These experiments discovered intriguing aspects that the phospholipid monolayer on the PFC-NEP surface was intact even after the binding of melittin and that the fluorescence of tryptophan residue was quenched when melittins bound to PFC-NEPs. Molecular determinants for the differential interaction of melittin with a target bilayer and the emulsifying monolayer on the surface of PFC-NEPs have yet to be determined. Chapter 4 addresses the structural details of differential melittin interaction to a bilayer and the emulsifying monolayer of PFC-NEP.

1.1.4   Cargo delivery

The final destinations of cargo molecules are mostly cytoplasm or sub-cellular organelles. To achieve efficient delivery to these final destinations, one has to understand the molecular mechanisms for internalization of nanoparticles across a plasma membrane. Phagocytosis and endocytosis are the most common internalization mechanisms of various nanoparticles such as liposomes and polymer-based nanoparticles.(36) However, these internalization mechanisms involve lysosomal degradation that attenuates therapeutic efficiency, particularly of therapeutic biomolecules such as nucleic acids, small peptides, and proteins. Hence, alternative strategies have been developed to avoid the lysosomal pathway and to directly insert cargo molecules into the cytoplasmic space. These strategies include the conjugation of therapeutic cargo to a cell-penetrating peptide(37; 38), electroporation(39; 40), and therapeutic ultrasound with microbubbles.(41; 42; 43) However, these methods have limitations such as a lack of specificity, difficulty for *in vivo* application, limited spectrum of cargo molecules to carry, and potential cell damage.(38; 40; 44; 45; 46)

Delivery using PFC-NEPs promises a mechanism overcoming these limitations by providing specificity, high capacity to load diverse cargo molecules, and a non-invasive mode of action to cross a plasma membrane. Macroscopic experimental observations suggest a two-step mechanism for the delivery of cargo molecules from PFC-NEPs to the cytoplasm of the target cells (47). First, cargo molecules are delivered from NEPs to target plasma membranes via passive diffusion, so called "contact-facilitated" delivery that takes place after the NEPs bind to or closely approach the target cell surface.(48) The diffusion of cargo molecules is thought to be mediated by a hemifusion lipid complex connecting the PFC-NEP to the target cell (see Fig. 1.1.4). The formation of the hemifusion lipid complex was hypothesized based on the well-studied fusion process between two bilayers, which progresses in the following pathway: close apposition, a hemifusion stalk formation, stalk expansion into a disc-shaped hemifusion diaphragm, and pore formation.(49; 50; 51; 52; 53; 54; 55; 56) Next, the cargo molecules are transported from the plasma membrane into the cytoplasm by active raft-dependent internalization at the cost of ATP hydrolysis.(47) However, the molecular details of both steps are largely unknown and must be understood in order to rationally design nanoparticles.
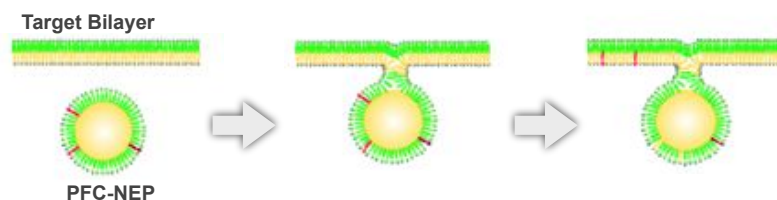
Figure 1.2: A schematic diagram of "contact-facilitated" delivery mechanism. PFC-NEP closely apposes a target bilayer. Two closely apposed monolayers form a hemifusion complex. Cargo molecules (red) diffuse to the target bilayer through the hemifusion complex.

1.2   Multi-scale computational approaches

1.2.1   Molecular dynamics (MD) simulations

Molecular dynamics simulations generate the time evolution of a system by numerically integrating Newton's equations of motion with the force computed for each atom.(57; 58; 59) The force acting on each atom is calculated based on an underlying force field that contains a set of parameters and equations to describe the interaction between atoms.(60; 61; 62; 63) The trajectory from MD simulations provides molecular details, from which various time dependent structural, dynamic, and thermodynamic properties are determined based on statistical mechanics.

Molecular dynamics simulations have been powerful tools to determine the dynamics and structures of lipid aggregates because they depend on the molecular aspects of the individual lipids and are intrinsically disordered to some degree.(64; 65) Experimental techniques can elucidate only highly averaged conformations while most of molecular details are ignored. The advantage of MD simulations become more pronounced when studying non-lamellar states that frequently appear for biologically important processes such as pore formation,(66; 67; 68) membrane genesis,(69; 70) membrane fusion and fission.(54; 71; 72)

Multi-scale MD simulations need to be used because the phenomena pertaining to membranes occur over a wide range of temporal and spatial scale. Figure 1.2.1 addresses the wide temporal ranges of lipid motions in pure biomembranes. Figure 1.2.3
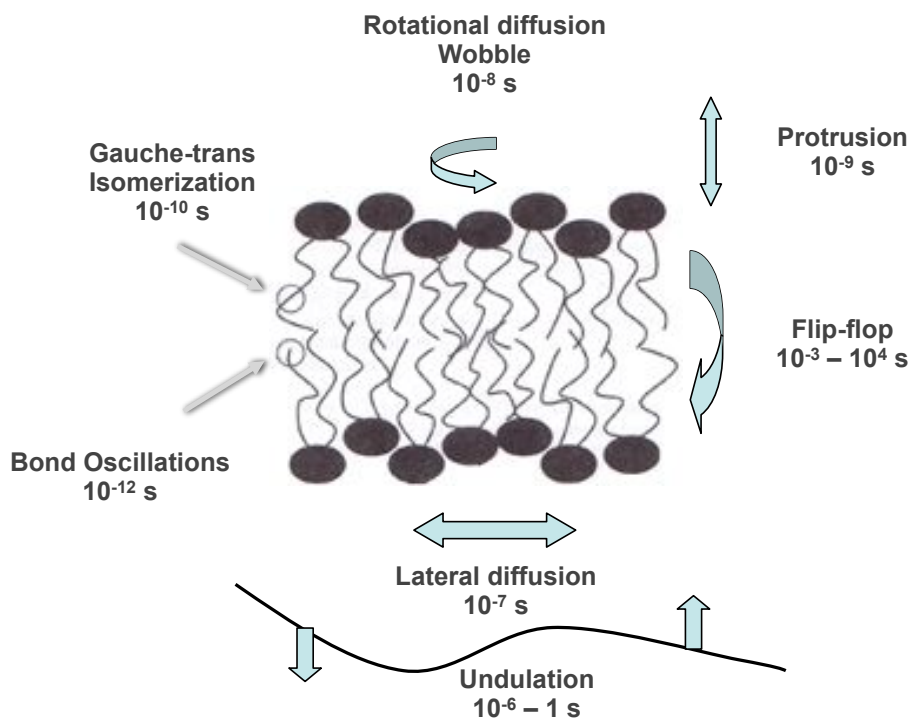
Figure 1.3: The wide range of time scales for lipid dynamics in a biomembrane. The time scale of the lipid motions in a pure membrane ranges from a ps level to a few hours, spanning 16 orders of magnitude difference. The figure is adapted from (73).

shows an example of multi-scale modeling to manifest the simplification of a molecule upon coarsening.

1.2.2 Atomistic simulations

All-atom simulations treat every atom explicitly, which provides the most detail. The most commonly used all-atom force field for membrane simulations is the CHARMM force field.(60; 74) However, due the large number of atoms in each lipid, an all-atom representation requires very high computational cost and significantly limits the accessible system size. United-atom representations were developed to resolve this high computational cost while keeping reasonably high levels of detail. United atoms are made by combining nonpolar hydrogen atoms and an aliphatic carbon into a single pseudo-atom.(75) The most commonly used united atom lipid model is based

on a combination of OPLS and GROMOS force fields, which is called the Berger lipid model.(76) This particular lipid model has been commonly used in combination with all-atom water model. Recently the combination of an all-atom protein model and the Berger lipid model was suggested.(77) Hence, simulations incorporating all-atom and united-atom models are often called "atomistic".

Even after implementing the united atom model, atomistic simulations are normally limited to small scale simulations such as a bilayer or monolayer simulations within the dimensions of several tens of nanometers for less than a few hundred nanoseconds.(69; 78; 79; 80) Such small scales can capture only limited biological phenomena such as the dynamics of pure membrane, binding of small molecules or ions,(80; 81) lipid mixing,(79) membrane protein fluctuation for very short time scales.(82) Recently, however, advance in computation techniques and abundant computing resources enabled vesicle fusion simulations at an atomic level.(55) This report shows that atomistic simulations will be more extensively used for large scale simulations because of its better accuracy than coarser models.

1.2.3   Coarse-grained simulations

Coarse-grained models can be categorized into two groups depending on the level of detail that a model confers. The first group uses very simple models such that a lipid is modeled by two beads, one hydrophilic and the other hydrophobic, and disregards electrostatic interactions.(83; 84) Despite the simplicity, these highly coarse-grained models are able to simulate mesoscopic phenomena such as self-assembly, phase transition, and domain formation. The coarse-grained models of the second group incorporate more details of individual lipids and are developed based on corresponding atomistic simulations and relevant experimental data including densities, mutual solubilities, and relative diffusion rates.(85; 86; 87) Generally these models contain divers types of beads and take account of electrostatic interactions and explicit solvent. Three major contributions to coarse-grained lipid have been made by Klein et al.(86) Izvekov and Voth,(87) and Marrink et al. (85; 88; 89) All models are able to reproduce self-assembly (90; 86) and obtain comparable structures as determined by atomistic simulations.(87).
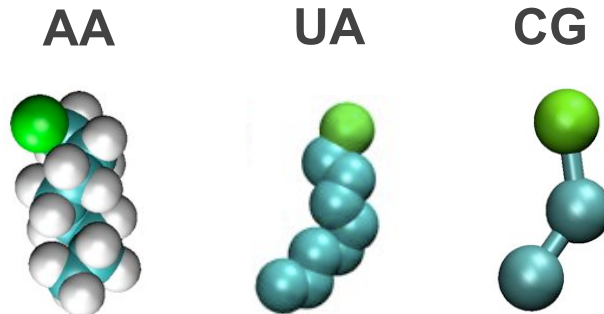
Figure 1.4: Modeling of a perfluorocarbon, perfluorooctylbromide (PFOB), with varying levels of molecular details: A) all-atom, B) united-atom, C) coarse-grained model. The number of atom reduces from 27 to 9 and 3 upon coarsening.

The MARTINI force field developed by Marrink et al. has been far more widely used than the other two due to several advantages. First of all, the parameterization of the interaction potentials is not tailored to a specific lipid type, and the small set of building blocks can be used to model different lipids.(85) Furthermore, systematic modifications of the interaction potentials allowed development of additional beads in accordance with the existing force field parameters.(89) Expansion of the bead types enabled modeling of proteins and small molecules such as cholesterol. Second of all, the MARTINI force field provides the easiest accessibility by using the same force field functions as GROMOS force field,(91) and hence the GROMACS simulation package can be used without any modifications.(92) The MARTINI force field has been extensively used to model mesoscopic phenomena pertaining to the membrane: bilayer self-assembly of DPPC(69) and mixed DPPC/DPPE lipids,(70) transition from the lamellar to inverted hexagonal phase,(93) domain formation,(94) pore formation,(66; 67; 68) bending, buckling, and curing of membrane.(95; 54; 71; 72) Therefore, we have employed the MARTINI force field to run coarse-grained molecular dynamics simulations of a closely apposed PFC-NEP and liposome. Chapter 5 reports the force field parameterization of a PFC molecule (PFOB) at a coarse-grained level, and molecular details observed during the fusion event.

1.3 Goal of Thesis

The goals of this thesis are to determine the molecular structure of the PFC-NEP interface and to elucidate the "contact-facilitated" delivery mechanism using multi-scale molecular dynamics simulations. These molecular details will help us understand the underlying mechanisms and optimize PFC-NEPs for more efficient delivery. The thesis is organized into the following chapters:

- Chapter 1 provides the introduction to PFC nanoemulsion particles and the technique applied for this thesis work, multi-scale molecular dynamics simulations.

- Chapter 2 is devoted to presenting my earlier research that is indirectly related to the stated goal of the thesis by addressing the general ion-membrane interactions and suggests the usage of K^+ over Na^+ ions in molecular dynamics simulations to prevent strong adsorption of Na^+ to the zwitterionic neutral lipids.

- Chapter 3 reports the force field parameterization of a perfluorocarbon, perfluorooctylbromide (PFOB) and atomistic structural details of the PFC-NEP interface described with the new in-house model.

- Chapter 4 presents the atomistic structural details of a melittin cargo molecule bound on the PFC-NEP interface in comparison with melittin bound to a bilayer.

- Chapter 5 reports the force field parameterization of PFOB at a coarse-grained level, spontaneous emulsion formation, fusion between PFC-NEPs and model liposomes, and molecular details over the course of fusion process.

- Chapter 6 provides the conclusion of the thesis and future direction based on the current research.

- Chapter 7 provides supplementary materials for Chapter 3, 4 and 5.

Chapter 2

Molecular dynamics simulations of asymmetric NaCl and KCl solutions separated by phosphatidylcholine bilayers: potential drops and structural changes induced by strong Na$^+$-lipid interactions and finite size effects.

2.1 Introduction

Membranes are among the most basic structures of cells and subcellular organelles. Direct interactions of cations with membranes have been extensively studied due

This chapter is reproduced from my paper published in Biophysical Journal in 2008 May 1, 2010.

to the prevalence of ions in biological milieu and the significant effects of ions on membrane properties such as phase transitions (96; 97; 98; 99), aggregation and fusion (100), surface charge densities and potentials (101; 102), structure and mechanical strength (103; 104; 99), and lipid mobilities (97). The nature of ion-lipid interactions has been studied by several methods, including infrared spectroscopy (96; 105), ζ-potential measurements (106), X-ray standing wave experiments (107), NMR spectroscopy (108), atomic force microscopy (104; 103), small angle X-ray diffraction (99), and molecular simulations (109; 110; 111; 112; 113; 97). Most of these studies conclude that higher valency ions have greater affinity and larger effects on biomembranes (96; 99); however, recent results have suggested that monovalent cations can also interact with biomembrane lipid moieties and alter bilayer properties (96; 104; 109; 111; 113; 97; 99).

Previous reports (111; 110; 114) have indicated that asymmetric Na^+ and Cl^- concentrations around bilayer systems can generate electrostatic potential differences as large as -85 mV across lipid bilayers in molecular dynamics simulations. These reports, in part, motivated the current study which was originally designed as a control for studying asymmetric applications of salicylate around bilayers to extend our previous work in this area (115). To this end, we designed a simulation that contained two bilayers separating chambers with differing NaCl and KCl concentrations but with the same net ionic strength. Simple analysis of this system on the basis of ion activities and the symmetries of the solutions suggests that, at steady state, the Nernstian transmembrane potential (e.g., the potential drop at infinite separations of the two bilayers) for this system should be negligible. However, as discussed in detail throughout the remainder of this manuscript, we observed a significant potential drop across DPPC (dipalmitoylphosphatidylcholine) bilayers due to selective Na^+ binding to the lipid carbonyls. Although there is some indirect experimental evidence which may suggest some degree of Na^+-carbonyl interactions (105), both the finite size of our simulation and the non-equilibrium nature of the system caution against over-interpretation of these observations. This paper addresses the possible effect due to the finite size on the calculation of membrane potentials and the issue on the force field parameters of ions on the electric properties and structures of membranes.
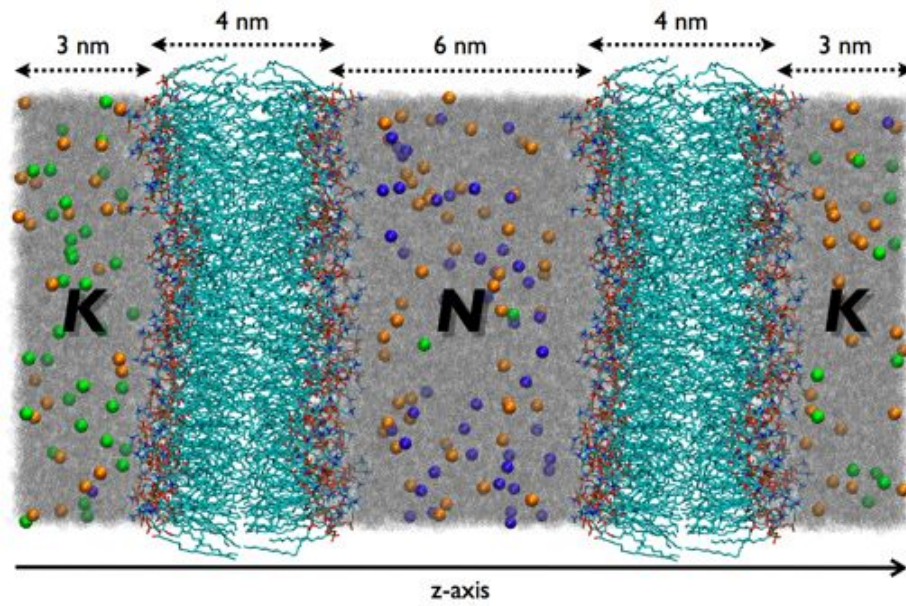
Figure 2.1: Diagram of "double bilayer" simulation geometry with approximate dimensions along z-axis labeled. Left and right boundaries are periodic (e.g., K is a single contiguous chamber in the simulation). As described in the text, the N chamber contains 48 Na$^+$, 2 K$^+$, and 50 Cl$^-$ ions while the K chamber contains 2 Na$^+$ (blue), 48 K$^+$ (green), and 50 Cl$^-$ (orange) ions.

2.2   Methods

2.2.1   Molecular dynamics simulations

GROMACS 3.2.1 (116) was used for the molecular dynamics (MD) simulations and preparation of the starting structures; GROMACS 3.3.1 was used for all analyses. DPPC (dipalmitoylphosphatidylcholine) lipids were simulated using the parameters of Berger and Lindahl (117) together with SPC water (118) and Straatsma-Berendsen sodium, potassium, and chloride ion parameters (119). This combination of force field parameters have been successfully used in a number of previous studies (115; 120; 121; 117) and show good agreement with experimental observables such as area per lipid head group and tail order parameters.

Following the work of Sachs et al (111), Gurtovenko (110), and Vernier et al (112), the starting structure of the DPPC double bilayer system shown in Fig. 2.1 was generated by duplicating a previously-equilibrated DPPC single bilayer system of 9.5 nm $\times$ 8.5 nm $\times$ 10.0 nm dimensions (115) along the bilayer normal direction. The hydration level of 60 waters per lipid provided a spacing of approximately 6 nm between the two bilayers. These two bilayers, together with the periodic boundary conditions used in this simulation, provided two separated water chambers, denoted "N" and "K" (see Fig. 2.1). Ions were inserted into the two water chambers by replacement of existing water molecules. In particular, 100 random water molecules in the N chamber were replaced by 48 Na^+, 2 K^+, and 50 Cl^- ions while 100 water molecules in the K chamber were replaced by 2 Na^+, 48 K^+, and 50 Cl^- ions. This placement of ions resulted in an electroneutral system with solutions of $\sim$ 150 mM ionic strength in both chambers but with different species ratios. The final simulation system was comprised of 512 DPPC, 30568 SPC water, 50 Na^+, 50 K^+, and 100 Cl^- molecules. The membrane system was equilibrated as described previously (115): the starting structure was subject to an energy minimization followed by a series of MD simulations to increase the system temperature to 323 K. After the system reached 323 K, the MD simulation was continued for 172 ns.

All MD simulations were performed with Lennard-Jones interaction cutoffs of 1 nm. Long-range electrostatic interactions were calculated using the particle-mesh Ewald

method (122) with conducting boundary conditions and a direct space cutoff of 1 nm. Simulations were performed in an isobaric-isothermal ensemble (NpT). The system pressure was maintained at 1 atm with a Parrinello-Rahman barostat (123) using a 2 ps coupling time. The temperature was maintained at 323 K through a Nosé-Hoover thermostat (124) with 0.5 ps coupling frequency. All bonds between hydrogen and heavy atoms were constrained using the SHAKE algorithm (125) which permitted a 2 fs time step. The simulations were performed on Intel Xeon cluster nodes at the National Biomedical Computation Resource and at the Texas Advanced Computing Center. Snapshots from the simulations were stored for analysis at 16 ps intervals.

To determine the effect of the monovalent cations, the properties of our present double bilayer system were compared with the those of an ion-free DPPC membrane simulation which has been described previously (115). The ion-free system is equivalent to the half of the double bilayer system along the z-axis and was simulated for 50 ns at the same conditions with the present simulation. The last 20 ns portion of the trajectory was used to analyze equilibrium observables for this system.

2.2.2 Statistical tools

Time averages were used to calculate expectation values for system observables. In general, these averages were computed over the 62 ns "stationary" portion of the 172 ns simulation, as described in Sec. 2.3.1. To compare the measured quantities between different systems or between different parts within the same system, the statistical errors of each quantity were calculated as explained below.

To estimate errors, the trajectory was divided or re-sampled into statistically-independent smaller blocks. In order to determine the size of these blocks for a particular observable, the autocorrelation time (126) of the observable was calculated for different delay times τ using the following equation:

$$C_A(\tau) = \frac{N}{N - \ell_\tau} \frac{\sum_{i=1}^{N-\ell_\tau} \left(A_i - \langle A \rangle\right)\left(A_{i+\ell_\tau} - \langle A \rangle\right)}{\sum_{i=1}^{N} \left(A_i - \langle A \rangle\right)^2}, \tag{2.1}$$

for N time points $\{t_1, t_2, \ldots t_N\}$ with equal spacing $\Delta t = t_{i+1} - t_i$ and a lag ℓ_τ such that $\tau = \ell_\tau \Delta t$. This autocorrelation function is for an observable A with mean value

$\langle A \rangle$ evaluated at each of the time points such that $A_i = A(t_i)$. A characteristic correlation time τ_A was calculated for each observable A as the smallest $|\tau|$ for which $C_A(\tau) = e^{-1}$. We wish to point out that, due to the use of an NpT ensemble for our molecular dynamics calculations, these correlation times are used strictly for resampling purposes and not intended for a description of the dynamics of this bilayer system.

To ensure statistical independence, decorrelation times of 2τ were used to generate new datasets for calculating observable statistics. In particular, following similar analyses by Chen and Pappu (127), bootstrap-style sampling-with-replacement (128) was used to generate new resampled datasets of size $N_r = \frac{t_{\max}}{2\tau}$ (rounded to the nearest integer) given the original evenly-spaced snapshots from a trajectory of length $t_{\max}$. Each resampled set was used to estimate averages for system observables. The distribution of these averages over all resampled sets was then used to estimate the variability of the observables and calculate variances and confidence intervals. Finally, the statistical significance between any two samples was assessed by the Student t-test with a 99.5 % confidence interval, using the error and the size of the resampled datasets.

Table 2.1: Ion distributions across the regions labeled in Fig. 2.3B as obtained from the 110-172 ns portion of the simulation. Unlisted correlation times imply no change in ion numbers during this simulation time. Averages and standard errors determined using the bootstrap resampling procedure described in the text with the specified correlation times.

Region	Ion	Correlation time (ps)	Number (average $\pm$ error)
N_1	Na^+	3968	16.2 ± 0.3
N_1	K^+	256.6	0.03 ± 0.01
N_1	Cl^-	31.7	0.51 ± 0.02
N_2	Na^+	5571.2	15.5 ± 0.5
N_2	K^+	160	1.95 ± 0.01
N_2	Cl^-	28.8	48.68 ± 0.03
N_3	Na^+	5332	16.2 ± 0.5
N_3	K^+	98.5	0.188 ± 0.005
N_3	Cl^-	28.5	0.82 ± 0.02
K_1	Na^+	–	2 ± 0
K_1	K^+	–	48 ± 0
K_1	Cl^-	–	50 ± 0

(A)

(B)

(C)

(D)
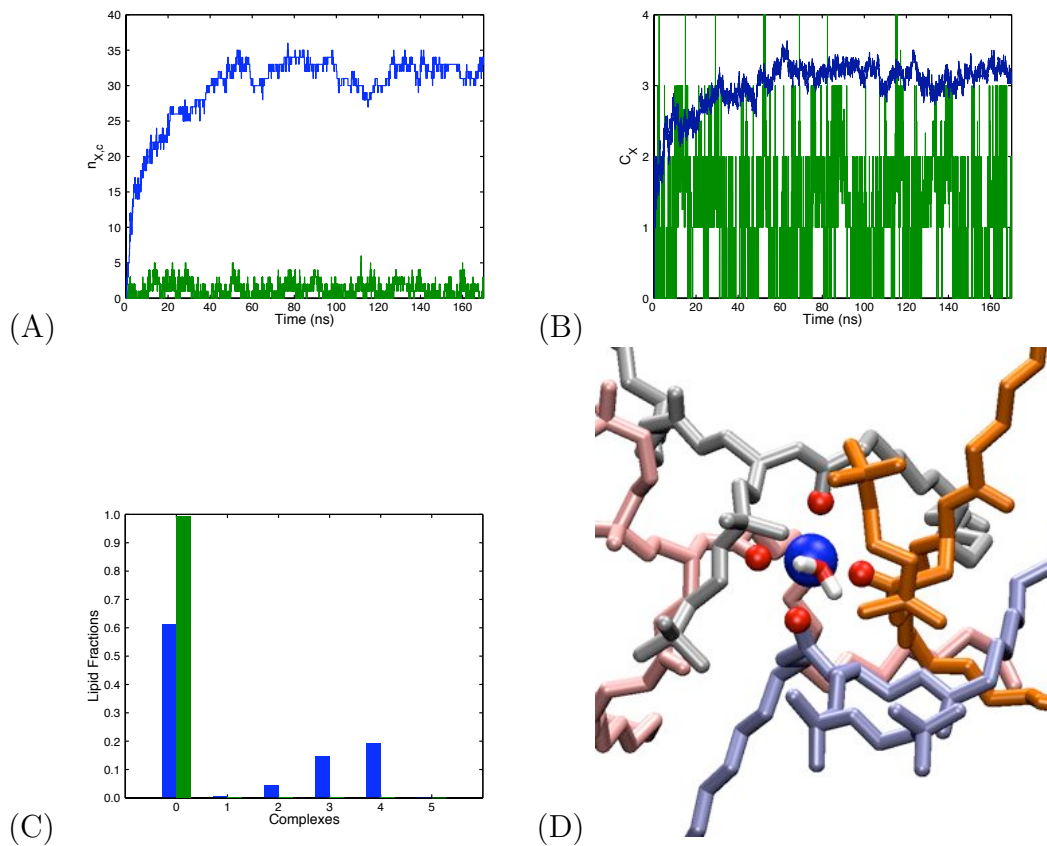
Figure 2.2: Phospholipids coordination by monovalent ions. A) Total number of lipid-coordinated ions as a function of time for Na^+ (blue) and K^+ (green). B) Average lipid-ion coordination numbers, defined in Eq. 2.2, as a function of time for Na^+ (blue) and K^+ (green). C) Lipid:ion ratios for coordinated Na^+ (blue) and K^+ (green) ions. The average fraction of the complex comprised of five DPPC molecules is 0.003 ± 0.007, so the bar is not visible in the figure. D) Example of a representative 4-coordinate lipid carbonyl-ion interaction from. Any residues within 3.2 Å from a Na^+ ion are displayed. The carbonyl oxygens coordinating the ion are shown red spheres.

(A)   (B)
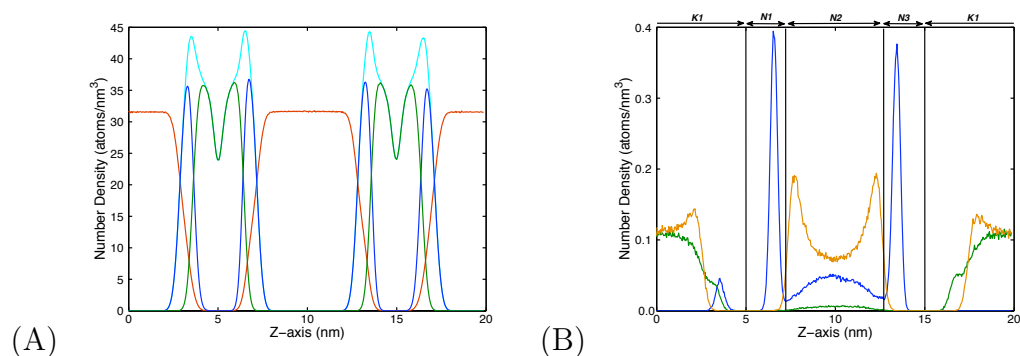
Figure 2.3: Relative number densities depicting fraction of total species as a function of distance along the bilayer norm (see Fig. 2.1 for coordinate definition). A) Distribution of lipid moieties (polar portion of lipid, dark blue; nonpolar portion of lipid, green; total lipid density, cyan) and water (red). B) Distribution of ions (Na$^+$, blue; K$^+$, green; Cl$^-$, orange) with specific regions labeled for binding analysis (see text).
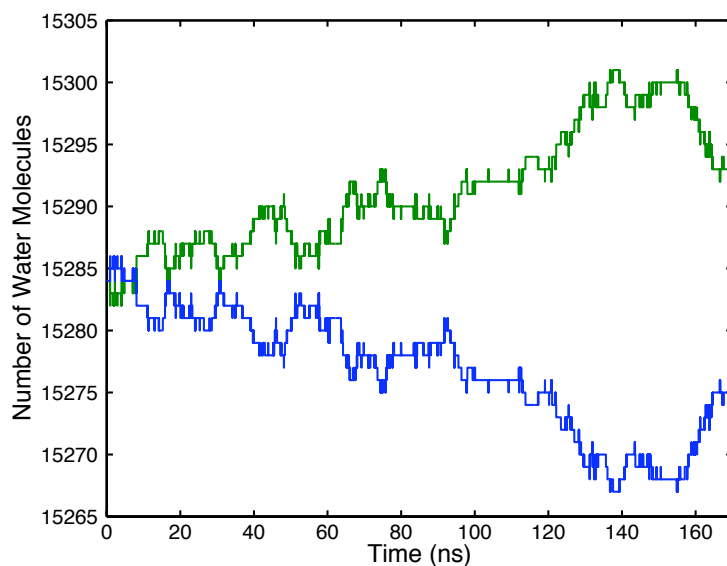
Figure 2.4: Water distribution in the double bilayer system. Number of waters in each chamber (K green, N blue) as a function of simulation time.

21

2.3   Results

2.3.1   Reaching steady-state

The non-identical nature of the N and K chambers throughout our simulation indicate that we are studying a non-equilibrium system at steady-state rather than the equilibrium observations associated with most molecular dynamics simulations. Monitoring macroscopic thermodynamics parameters is a standard procedure to verify the equilibrium or steady state of the system. In our simulation, parameters such as temperature, box pressure, and total energy of the system reached stationary values at an early stage of the simulation (e.g., less than 10 ns); however, several other system properties took much longer to stop drifting. Previous reports have shown that adsorption and coordination of cations by carbonyl oxygens is one of the slowest processes in the simulation of salt-containing zwitterionic bilayer systems (129; 97; 110). Given these observations, we examined the time course of absorption and coordination of Na$^+$ and K$^+$ by the DPPC headgroups using the methods described below (see Eq. 2.2 and description in Sec. 2.3.2). As shown in Fig. 2.2A and 2.2B, the total number of lipid-coordinated ions and the average coordination number increased throughout the initial 65 ns of the simulation; no significant drift was observed after 65 ns. For our simulation, however, the most slowly-converging observables were net water flux across the bilayers (see Sec. 2.3.3 and Fig. 2.4) and box area (see Sec. 2.3.4 and Fig. 2.5), which reached the steady-state only after 110 ns. Although the changes in area were very small, they occurred over the same timescales as "fast" ion binding and water flux through the membrane. While such small area changes alone may not warrant concern about simulation convergence, their appearance together with other slowly-relaxing properties, led us to confine our analysis to the last 62 ns of our 172 ns trajectory.

2.3.2   Ion-lipid interactions

To assess the specific interaction of each cation with the lipid, the average DPPC-cation coordination number (c_X) for each cation (X is Na$^+$ or K$^+$) was calculated in
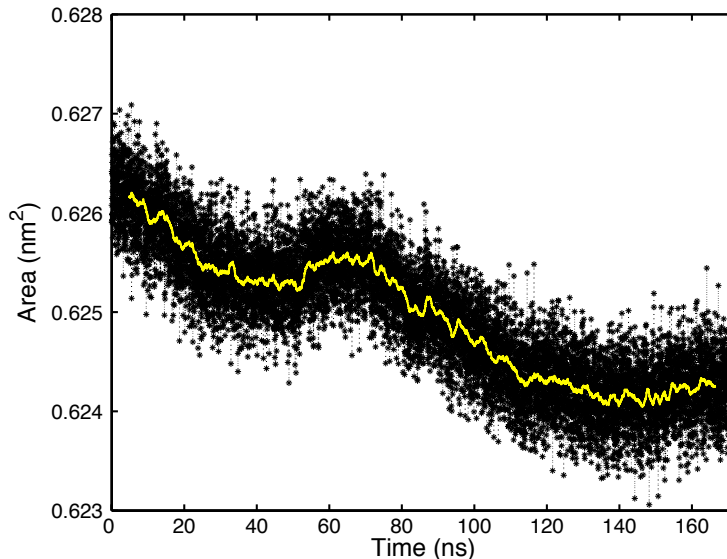
Figure 2.5: Plot of simulation box cross-sectional area (in the bilayer planes) over the course of the molecular dynamics run. Figure includes individual snapshots (every 16 ps, dots) and 1.6-ns running average (line).

a manner similar to Gurtovenko (110) by

$$c_X = \frac{n_C}{n_{X,c}} \tag{2.2}$$

where n_C is the number of carbonyls within a cutoff distance $r_{X,c}$ of any ion of species X and $n_{X,c}$ is the number of ions of species X within a cutoff distance $r_{X,c}$ of any lipid carbonyl group. We chose $r_{c,\text{Na}^+} = 0.322$ nm and $r_{c,\text{K}^+} = 0.375$ nm as determined from the first minima of the Na^+- or K^+-DPPC carbonyl oxygen radial distribution function (data not shown). The results from this analysis are illustrated in Fig. 2.2 and summarized in Table 2.2. Na^+ coordination numbers varied from 3.11 ± 0.03 in the N chamber to 3.2 ± 0.4 in the K chamber while K^+ coordination numbers were much smaller: 0.008 ± 0.002 in the N chamber and 1.2 ± 0.1 in the K chamber. The distribution of ion coordination states is shown in Fig. 2.2C. The primary mode of Na^+ coordination was via DPPC carbonyl oxygens, as illustrated in Fig. 2.2D.

Our average Na^+-lipid coordination number (3.11 ± 0.03) is comparable to the results of Gurtovenko (110). However, we also observed complexes involving 4 and 5

(A)   (B)
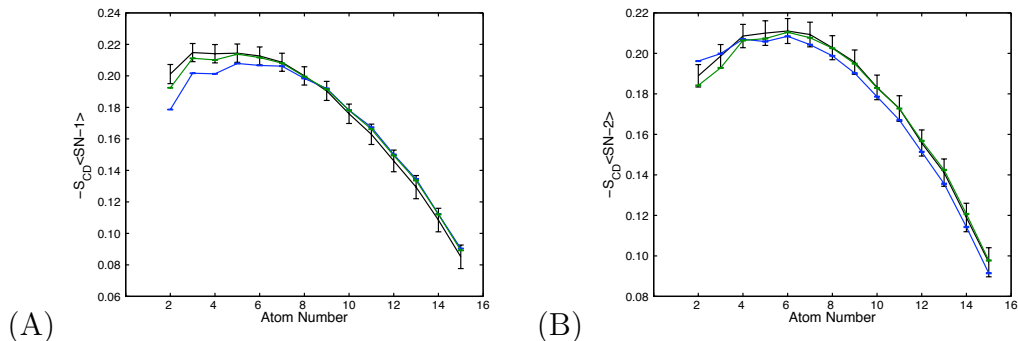
Figure 2.6: DPPC A) SN-1 and B) SN-2 tail order parameters for N chamber DPPC leaflets (blue), K chamber DPPC leaflets (green), and a DPPC bilayer surrounded by pure water (black).

lipid molecules and found that 4-coordinate Na^+ was the most common. Gurtovenko observed 3-coordinate Na^+ most frequently and did not report any 5-coordinate complexes. There are a number of potential reasons for these differences; the most likely is sampling (45 ns for Gurtovenko vs. 172 ns here). In particular, 5-coordinate lipid-Na^+complexes were observed only after 130 ns of simulation, suggesting a much slower rate of formation.

2.3.3 Ion and water distributions

Figure 2.3 shows number densities for water and lipid moieties (Fig. 2.3A) as well as individual ion species (Fig. 2.3B) as a function of distance along the bilayer normal. These figures clearly demonstrate significant adsorption of Na^+ to the polar region of the DPPC bilayers. This adsorption is quantified in Table 2.1, which summarizes the numbers of ions observed in each region of the simulation domain. As discussed below, the specific association of Na^+ with the bilayer appears to be due to coordination by the DPPC carbonyl oxygens (Sec. 2.3.2) and leads to a significant dipole moment at the interface of the N chamber DPPC leaflets (Sec. 2.3.5).

Time-dependent changes in water distribution in the double bilayer system are illustrated in Fig. 2.4. Over the first 110 ns of the simulation, water redistributed from the initial configuration of 15284 water molecules in each chamber to 15271 ± 3 in the N chamber and 15297 ± 3 in the K chamber. Even though the ionic strengths of

(A)

(B)

(C)

(D)
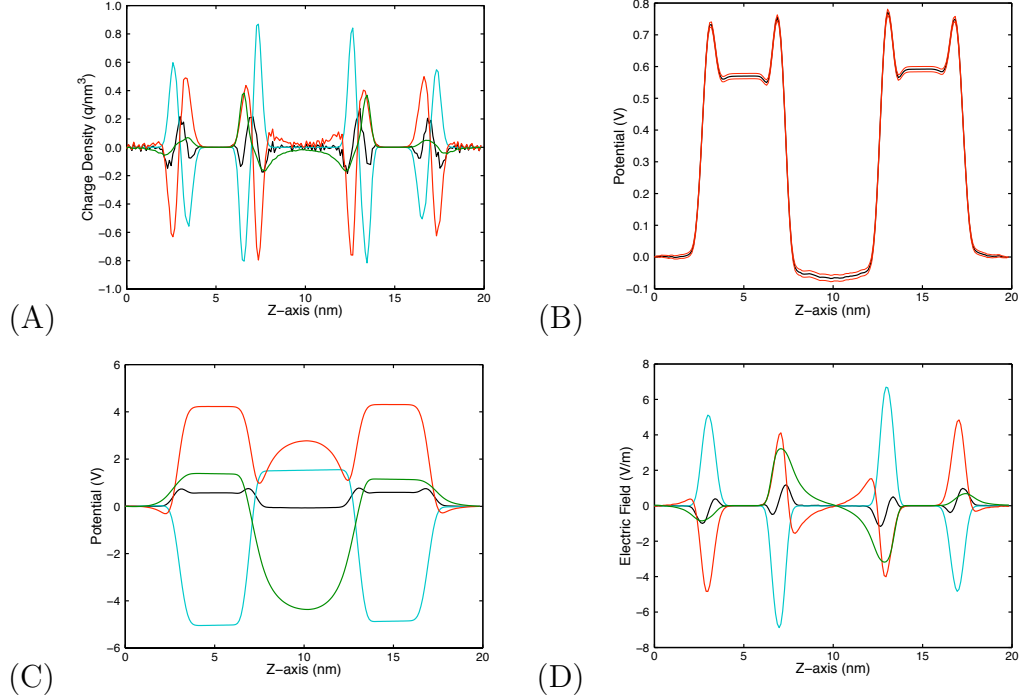
Figure 2.7: Electrostatic potentials in the double bilayer system. A) Charge density components of bilayer system; the entire system (black), lipids (cyan), water (red), and ions (Na^+, K^+, and Cl^-; green) B) Total electrostatic potential (black line) with standard deviations (red) calculated as described in the text. The potential drop across the bilayer is calculated from the potential value of -70 mV (-0.07 V) at $z = 10$ nm. C) Electrostatic potential components due to the lipids (cyan), water (red), ions (Na^+, K^+, and Cl^-; green), and the entire system (black). D. Electric field components due to lipids (cyan), water (red), ions (Na^+, K^+, and Cl^-; green), and the entire system (black).

the two chambers were the same, adsorption of Na^+ ions onto membrane likely generated an osmotic imbalance between the two chambers. This argument is supported by the observation that the net water flux started at around 10 ns, which is after a significant number of Na^+ ions had adsorbed onto the membrane. By 110 ns, a net of 13 ± 3 water molecules (0.083% of total) had transferred across the membrane; after this time, fluctuations in N and K chamber water numbers were observed but without a net change over the last 62 ns of simulation. Note that this net water flux is small and, unlike similar work with stronger fields and ion asymmetries (112; 114), not related to the formation of pores in the bilayer structure.

25

(A) (B)
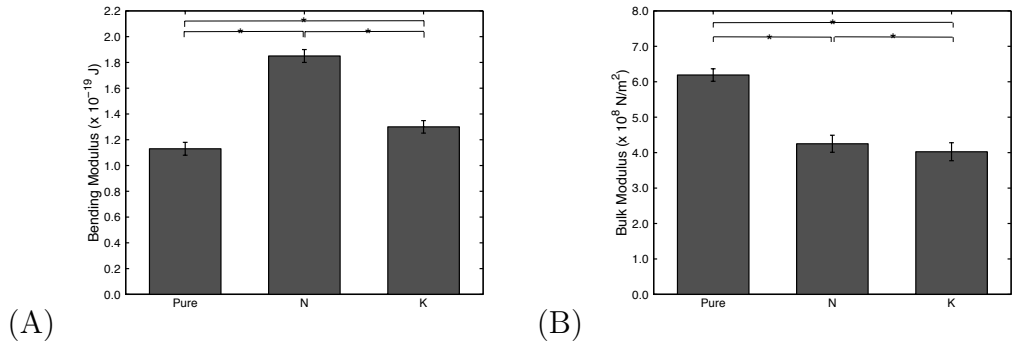
Figure 2.8: Membrane mechanical properties changed due to ion interactions. A) Bending and B) bulk moduli for leaflets facing the N and K chambers in the double bilayer setup (see Fig. 2.1) and for leaflets of a 128-lipid DPPC bilayer in pure water. Brackets and asterisks denote differences that are statistically significant (Student t-test, $\geq 99.9\ \%$ confidence level).

2.3.4 Lipid structure: head group area and tail order parameters

The area per head group $\langle A \rangle$ is a fundamental characteristic of the membrane and provides an important comparison to available experimental structural data (120; 130; 131). The area per head group was calculated by dividing the projected box area in the xy-plane by the 128 lipids in each leaflet. As shown in Fig. 2.5, the area per headgroup started at 0.6295 nm^2 and, over a period of approximately 110 ns, decreased very slightly to a value of 0.6255 $\pm$ 0.0001 nm^2 (as calculated over the last 62 ns trajectory by using the bootstrap method with a correlation time of 16 ps). In our simulation, this drift occurs over a much longer period than the 65 ns required for steady-state ion binding and, instead, has timescales similar to the transfer of water between the N and K chambers (see Fig. 2.4). Despite this small change in bilayer area due to Na$^+$ binding, the range of $\langle A \rangle$ is in reasonable agreement with experimental data (131) and previous simulations (115; 132). Other simulations of lipid bilayers in the presence of aqueous Na$^+$ ions have reported a much larger decrease in membrane area associated with Na$^+$ binding (110; 97; 132) than the small contraction observed in this work. These differences are discussed in more detail in Sec. 2.4.3.

The lipid tail order parameters of the two acyl chains of DPPC were calculated for comparison against published data (133). The order parameters were calculated separately for each leaflet to distinguish the effect of different local ion concentrations in the N and K chambers. The algorithms for calculating order parameters and descriptions of their interpretations have been described previously (115; 134). We generated order parameters from our simulation data using the resampling method described above, using every snapshot of the trajectory. This statistical independence was identified by examining the correlation time of $\langle A \rangle$, an important determinant of lipid tail order. This area correlation time was shorter than the sampling rate of 16 ps, allowing us to use every snapshot of the simulation in our analysis. As shown in Fig. 2.6, the overall shapes of the order parameter profiles are similar between the three different leaflet environments (N chamber, K chamber, and a DPPC bilayer in pure water) and are reasonably close to experimentally measured order parameters (133). The SN-1 tail of DPPC was disordered in the N and K chamber leaflets relative to the DPPC bilayer in pure water near the carbonyl oxygens (Student t-test, 99.5 % confidence interval). On the other hand, the SN-2 tails of N leaflet lipids showed slight ordering of carbons near the carbonyl oxygens (Student t-test, 99.5 % confidence interval), presumably due to the higher participation of SN-2 carbonyl oxygens in coordination of Na^+ (data not shown).

Table 2.2: Ion-carbonyl coordination statistics calculated according to Eq. 2.2. Averages and standard errors determined using the bootstrap resampling procedure described in the text with the specified correlation times.

Chamber	Ion	Correlation time (ps)	Coordination number (average ± error)
N	Na^+	2131	3.11 ± 0.03
N	K^+	42	0.008 ± 0.002
K	Na^+	12592	3.2 ± 0.1
K	K^+	832	1.2 ± 0.1

2.3.5 Electrostatic potential

The membrane potential was calculated from the total charge density to examine the
effect of the asymmetric ion distributions on the electrostatic properties of the mem-
brane. Given the zero potential difference boundary conditions implied by "conduct-
ing boundary" particle-mesh Ewald electrostatics (135; 122), the electric displacement
was calculated according to

$$D(z) = \int_0^z \rho(z')dz' + D_0 \tag{2.3}$$

and the potential difference was calculated according to

$$\phi(z) - \phi(0) = -\frac{1}{\epsilon} \int_0^z \left(\int_0^{z'} \rho(z'')dz'' + D_0 \right) dz', \tag{2.4}$$

where ϵ is a *homogeneous* dielectric constant, $\rho(z)$ is the charge density. For a net neu-
tral system with the boundary conditions described above, the displacement constant
D_0 is defined by

$$D_0 = -\frac{1}{L} \int_0^L \int_0^z \rho(z'')dz''dz, \tag{2.5}$$

This constant D_0 is related to the total polarization of system and is similar to that
obtained by Sachs et al (111). For our simulation, $D_0 = 0.0142$ $z \cdot$ nm^{-1} $= 2.27$
$\times 10^{-12}$ C$\cdot$ m^{-1}.

The simulation box was divided into 200 slabs parallel along the bilayer normal (z)
direction. Potentials calculated at every 16 ps showed no correlation between snap-
shots at every slab along the z-axis, which implies that the correlation time is much
smaller than 16 ps. To verify this short correlation time, an additional short sim-
ulation was performed with a much more frequent output rate of 4 fs. From this
simulation, the correlation times of membrane potential were determined to be less
than 1 ps at all slabs, indicating a rapidly-fluctuating potential across the entire
membrane system. Since the correlation time was much shorter than the sampling
rate (16 ps), all snapshots were statistically independent from each other, and the
bootstrap resampling protocol described above was performed with all 4062 snapshots
of the trajectory. Charge densities (Fig. 2.7A) were used to calculate the potential

Table 2.3: The Lennard-Jones interaction parameters of Na$^+$and K$^+$ions. The FFGMX parameters were obtained from the GROMACS package(116). We have also included Åqvist (137) and CHARMM parameters for comparison. The Åqvist parameters are reproduced from Chen et al.(127). The CHARMM parameters for Na$^+$ are obtained from Gurtovenko et al. (114), and the modified CHARMM parameters for K$^+$ are from Roux (138).

Ion	FFGMX		Åqvist		CHARMM	
	σ (nm)	ϵ (kJ mol^{-1})	σ(nm)	ϵ(kJ mol^{-1})	σ(nm)	ϵ(kJ mol^{-1})
Na$^+$	0.25752	6.17743$\times10^{-2}$	0.33305	1.15980$\times10^{-2}$	0.24299	1.96290$\times10^{-1}$
K$^+$	0.64541	5.66508$\times10^{-5}$	0.49346	1.37235$\times10^{-3}$	0.35275	3.64251$\times10^{-1}$

(Fig. 2.7B) by trapezoidal rule integration (136) according to the formulæ above with $L = 20$ nm and $\epsilon = \epsilon_0$, the permittivity of free space.

The resulting potentials were averaged and plotted in Fig. 2.7B which shows a net potential drop across the bilayers of -70 $\pm$ 10 mV between the K and N chambers. Fig. 2.7C decomposes this potential into separate contributions from lipid, water, and ions. This figure demonstrates that both lipids and water contribute to a net positive potential drop while the ions provide a large negative contribution. The origins of the negative ion contribution can be deduced from Fig. 2.3B which shows a clear layering or separation of Na$^+$ and Cl$^-$ ions at the membrane-water interface of leaflets in the N chamber, leading to a large surface dipole moment. On the other hand, K$^+$ and Cl$^-$ ions in the K chamber are much more uniformly mixed and generate smaller surface dipoles. These differing surface dipoles are clearly evident in Figure 2.7A, which plots charge densities across the simulation domain.

2.3.6   Membrane mechanics

Ions are known to affect membrane fusion and phase transitions (139; 140). Divalent ions have also been demonstrated to change the bulk modulus of DPPC bilayers (141). Such effects can be quantified in our simulations by calculating mechanical moduli related to the deformation of membrane in different modes such as membrane bending and volume fluctuation. To compare the effects of different ionic environments, all

mechanical measurements were made on each leaflet separately and then averaged over the two leaflets which share the same water chamber (see Fig. 2.1).

The bending modulus denotes the energy required to bend the membrane and was calculated on a per-leaflet basis, therefore including both peristaltic and undulatory types of motion (142). The methods to describe the calculation of bending modulus have been described previously (115; 121), although these previous studies focused on mechanics of bilayers rather than individual leaflets. Briefly, a per-leaflet height function was constructed by the position of the glycol carbon (C12) of each lipid. These heights were mapped on a 0.5 nm grid which was then Fourier-transformed to give $\hat{h}(\mathbf{q})$. Each resulting $\hat{h}(\mathbf{q})$ field was averaged over the two leaflets sharing the same water chamber. The bending modulus k_c was calculated according to

$$K_{\text{bend}} = \frac{k_B T A}{8.3\pi^3} \int d\mathbf{q} \left| \hat{h}(\mathbf{q}) \right|^2 , \tag{2.6}$$

where k_B is Boltzmann's constant, T is the temperature, A is the (average) area, and $\left| \hat{h}(\mathbf{q}) \right|^2$ is the square modulus of $\hat{h}(\mathbf{q})$. Figure 2.8 illustrates the differences in bending modulus for the lipid leaflets facing the N and K chambers and for a DPPC bilayer in pure water. All numbers are in reasonable agreement with the experimental bending modulus of 1.0×10^{-19} J (143). Figure 2.8 shows large and significant differences (Student t-test, 99.9% confidence interval) in the N leaflet bending modulus when compared to the K leaflets or the leaflets of the DPPC bilayer in pure water. Conversely, differences between the K leaflet and the pure water DPPC bending moduli are much smaller, although still statistically significant. Errors on the bending modulus were calculated using the bootstrap method described above with 78 (single DPPC bilayer leaflets), 177 (N chamber leaflets), and 96 (K chamber leaflets) snapshot sample sizes based on 128 (single DPPC bilayer leaflets), 176 (N chamber leaflets), and 240 (K chamber leaflets) ps correlation times for the integral of $\left| \hat{h}(\mathbf{q}) \right|^2$.

The bulk modulus describes the (volume) compressibility of the membrane and can be determined from the fluctuation of the membrane volume through the following relationship (144):

$$K_{\text{bulk}} = \frac{k_B T V}{\sigma_V^2} \tag{2.7}$$

where K_{bulk} is the bulk modulus, V is the average volume of a leaflet, k_B is Boltzmann's constant, T is the temperature, and σ_V^2 is the variance in leaflet volume. The volume of the membrane was calculated for each leaflet separately by multiplying the box area with the thickness of each leaflet. The thickness of a leaflet was determined from the average distance between phosphorus atom and the center of bilayer (145; 131). Based on Student t-tests with a 99.9% confidence interval, the average volume of the leaflets were significantly different: 308.16 ± 0.04 nm^3 for the single DPPC bilayer system, 305.8 ± 0.1 nm^3 for the N chamber leaflets, and 305.2 ± 0.1 nm^3 for the K chamber leaflets. This volume data was used to calculate the bulk modulus according to Eq. 2.7 above with errors assessed using the resampling methods described above with 1250 (single bilayer), 324 (N chamber), and 243 (K chamber) snapshot sample sizes based on 8 (single bilayer), 96 (N chamber), and 128 (K chamber) ps correlation times for volume. Figure 2.8 shows the bulk moduli and associated errors for each of the leaflets; both the N and K chamber leaflets showed significant differences with respect to the pure water DPPC bilayer leaflets. The N and K leaflets had significantly different bulk moduli, although these differences were much smaller than deviations from the pure water DPPC bilayer.

2.4   Discussion

Our results show that the asymmetric distributions of different NaCl and KCl solutions within our small double bilayer system can generate net potential differences across DPPC membranes. In our simulation, this potential drop arose from imbalances in the magnitudes of induced dipoles on both sides of the membrane caused by differing levels of adsorption of monovalent cations to the DPPC bilayer surfaces. The process of monovalent ion adsorption and water redistribution was extremely slow, requiring 65 ns before our non-equilibrium simulation reached an apparent steady state. At steady state, we observed high levels of Na^+ bound to the headgroup region of the DPPC bilayers through coordination by lipid carbonyl groups. Adsorption of Na^+ to the headgroup region was accompanied by accumulation of Cl^- at the membrane surface, leading to a net dipole on N chamber leaflets of the double bilayer system (see Fig. 2.3). K^+ ions showed significantly less affinity for the bilayer and thus created a much smaller surface dipole moment. The net result of these dipoles was a field across the bilayer which, in turn, led to the observed -70 $\pm$ 10 mV potential drop.

2.4.1   Other observations of membrane cation binding

As observed in previous computational simulations, we saw extensive coordination of Na^+ ions by DPPC carbonyl oxygens (114; 97) throughout our simulations resulting in high densities of Na^+ ions at the lipid carbonyl region of the membrane-water interface (97; 132; 146). Conversely, K^+ showed significantly less coordination by lipid carbonyl oxygens and, as a result, was distributed more uniformly away from the carbonyl region of the lipid-water interface. Finally, as observed in previous simulations (132; 97), Cl^- ions were largely excluded from the interface region.

Recent experimental work has also observed specific monovalent ion-lipid interactions, some of which provide indirect support for the interactions observed in our simulations. First, recent atomic force microscope work by Fukuma and coworkers (104) revealed specific interactions of Na^+ ions with the headgroups of gel-phase DPPC lipids. The primary site of these interactions appears to be the DPPC phosphate

groups, a mode of Na$^+$-DPPC interaction not observed in our molecular dynamics simulations but observed in other molecular dynamics simulations of Sachs et al using the CHARMM force field in a different thermodynamic ensemble (113). However, Fukuma and co-workers observed interesting regions of interactions between neighboring DPPC molecules at heights below the sites of Na$^+$-phosphate interactions (104); these lower-height interactions could be due to water molecules or Na$^+$ ions bridging adjacent DPPC carbonyls (Jarvis, personal communication). Second, infrared spectroscopy measurements were made on 1-palmitoyl-2-oleoyl-*sn*-glycero-3-phosphocholine (POPC) vesicles in solutions of various metal chlorides. Addition of LiCl, NaCl, and KCl to highly-hydrated POPC vesicles showed decreases in C=O vibrational frequencies but little change in the asymmetric PO$_2$ stretching mode frequencies, indirectly suggesting possible interactions between the cations and POPC carbonyls. Note that these experiments revealed significant effects for Li$^+$, Na$^+$, and K$^+$, while our simulations only showed significant carbonyl association for Na$^+$ (Li$^+$ was not included in our simulations). These differences in putative carbonyl association could be due to a number of reasons, including differences between POPC and DPPC and possible simulation artifacts (discussed below). However, it is important to note that these experiments were carried out at ion-to-lipid mole ratios of 1.6 which are much higher than the 0.2 ion-to-lipid (or 0.1 Na$^+$-to-lipid and 0.1 K$^+$-to-lipid) ratios used in our simulations. Third, Böckmann et al (97) used excess heat capacity measurements to demonstrate how increasing NaCl concentrations shift POPC gel-to-liquid phase transition temperatures to higher temperatures and broaden the overall calorimetric profile. Such broadening suggests decreased cooperativity of the phase transition due to the presence of NaCl (147). The same authors also studied the diffusion constant of POPC molecules at different NaCl concentration. The appearance of populations of lipids with much lower diffusion constants was matched to the complexation of the lipids by coordinating Na$^+$ ions. Finally, Pabst and co-workers (99) used small angle X-ray diffraction to observe structural and mechanical changes in POPC bilayers, albeit at higher concentrations (> 1 M) than used here.

Table 2.4: Partial charges (in e) for lipid carbonyls were adpated from Chandrasekhar et al. (151) for FFGMX parameters and from Heller et al. (152) for CHARMM parameters.

	FFGMX		CHARMM	
	sn-1	sn-2	sn-1	sn-2
Ester oxygen	-0.7	-0.7	-0.34	
Carbonyl carbon	0.8	0.7	0.63	
Carbonyl oxygen	-0.6	-0.7	0.52	

2.4.2   Force field sensitivity

The proper force field parameters are critical to reproduce the chemico-physical properties of the ions during the simulations (127). The Lennard-Jones interaction parameters for Na^+ and K^+ ions were obtained from the GROMACS FFGMX force field (116) which contains parameters loosely related to values from Straatsma and Berendsen (119), in which the parameters of these ions were fit to reproduce the gas-phase energetics for ion monohydrates calculated by *ab initio* SCF calculations. These parameters were implemented in the GROMACS force field and have been widely used for ion-membrane interactions (148; 110; 149; 132), despite problems accurately describing K^+-protein interactions when used with protein GROMOS force field parameters (150). Additionally, although popular, these Straatsma-Berendsen parameters yield ion solvation free energies which are significantly more negative than experimental values (119; 137). As shown in Table 2.3, these FFGMX parameters used in our simulations are significantly different from the Åqvist parameters often used in protein and nucleic acid simulations (137) and also differ from the modified ion parameters of Roux (138). It is possible that these particular ion parameters may have contributed to the strong adsorption of Na^+ ions to the membrane. Comparative analysis of ion force field effects on these results is underway; however, interested readers should also refer to the recent work of Gurtovenko and Vattulainen for similar comparisons (114).

Another potential source of concern lies in the high dipole moment of the lipid carbonyl group (see Table 2.4) used in our and many other GROMACS-based simulations (110; 114; 146; 153; 154; 97; 129; 155). The high partial charges associated with the lipid headgroup were determined by ab initio SCF calculations and resulted

34

in good agreement with experimental areas per head group when simulated in constant pressure ensembles (156; 151). However, it is possible that this high carbonyl dipole moment could also influence Na^+ interaction with the lipid headgroups and lead to the high surface dipoles observed in the current simulations. Comparison of GROMACS lipid parameters with other force fields is currently underway.

Of course, most fixed charged force fields are faced with a fundamental flaw: their inability to accurately predict transfer free energies for multiple types of media (e.g., water, vacuum, protein, lipid, etc.) simultaneously due to their lack of atomic polarizability (157; 158; 159; 160). One consequence of this lack of atomic polarizability in the context of lipid bilayers is an artificially-low dielectric coefficient in the lipid tail region. In particular, the neutral united-atom alkane model used in the current fixed charge lipid force field yields an effective dielectric coefficient of 1 for the lipid tail region; however, a polarizable model for the alkane tails would yield an dielectric coefficient for this region of approximately 2 (158). Such differences in dielectric coefficients have been shown to significantly affect ion permeation through gramicidin A channels (161; 158) and may have an impact on the localization of ions in the DPPC bilayers considered here. Another potential consequence of the fixed charge force field is an incorrect affinity of Na^+ and K^+ for the lipid headgroup region; a symptom of the inaccurate transfer free energies of fixed charge force fields discussed above. The inclusion of polarizability in a force field comes at the expense of additional computation time which would have made the 172 ns of simulation reported here prohibitively expensive. However, we look forward to the advances in polarizable force field simulation methodology and computational power which should make the routine use of polarizable force fields feasible in the near future.

2.4.3 Finite size effects

Our double bilayer system was relatively large. We included 256 lipids per bilayer (512 lipids total), to allow for reasonable membrane undulations (121). Additionally, we used much larger water chambers than other recent double bilayer studies (110; 111; 112). However, despite these precautions, there are important finite size artifacts which effect this work and should serve as a precaution to other groups interested in simulating asymmetric aqueous solutions in similar double bilayer configurations.

Electrostatic properties. One finite size artifact in this simulation arises from the finite extent of our water chambers between lipids, despite their relatively large size as compared to recent simulations (110; 111; 112). Both the ion distributions and the water polarization data presented earlier demonstrate the influence of finite size effects. The counterion distributions (Fig. 2.3B) do not reach "bulk" or constant values anywhere within the simulation domain. Given large enough water chambers, we would expect a region of nearly constant ion densities between the bilayers, corresponding to a weak electrostatic field and nearly constant ion concentrations. Likewise, the electric field (Fig. 2.7D) also lacked a region of constant (small) values and, instead, was zero only at the center of the water chambers. Since the electric field due to the water molecules is expected to be proportional to their polarization, this implies that the water in these systems was strongly influenced by their proximity of the bilayer surfaces. As such, it is highly unlikely that our current simulation is measuring Nernst "transmembrane" potentials; e.g., the net drop in potential observed in "bulk" solution at some distance from the membrane surface associated with net differences in ion chemical potentials. Instead, it is much more probable that the results of this simulation reflects a combination of surface potentials due to (1) asymmetric double layers induced by strong DPPC-Na$^+$ interactions in the GROMACS force field and (2) potential artifacts from the finite size of the simulations.

Structural properties. A second finite size artifact in this simulation arises from the finite number of lipids in the bilayer leaflets. Other simulations of lipid bilayers in the presence of aqueous Na$^+$ ions have reported a much larger decrease in membrane area associated with Na$^+$ binding (110; 97; 132) than the small contraction observed in this work. It is important to keep in mind that our system was set up with equal numbers of lipids in the N and K chambers, unlike recent work by Gurtovenko and Vattulainen (162) on lipids of asymmetric composition, but similar to the pore formation simulations of Gurtovenko (114) as well as past simulations of asymmetric ionic solutions by Sachs et al (111), Gurtovenko (110), and Vernier et al (112). However, significant ion binding was only observed for leaflets in the N chamber. The periodicity of our system, together with its relatively small size, prevents an asymmetric compression of the N and K chamber leaflets in response to ion binding. This finite size artifact is present in common double bilayer setups where asymmetric aqueous solutions are expected to induce asymmetric structural changes in bilayer leaflets but

are unable to do so due to periodic constraints and (relatively) small system size. In the present case, the finite number of lipids in our setup prevented the asymmetric change in area between the N and K chamber leaflets resulting the observed area decrease which was much smaller than previous symmetric Na^+ solution simulations. Note that this lack of change in area could also possibly compound the finite size effects on electrostatic properties described above by alternating the dipole moment densities associated with each leaflet. This finite area artifact could likely be overcome in future simulations by simulating systems with fewer lipids in the K chamber leaflet, in a manner similar to the simulations by Gurtovenko and Vattulainen (162) on bilayers of asymmetric composition. We are exploring configurations for future simulations.

2.5   Conclusions

An atomic-detail MD simulation has been used to demonstrate the influence of ion imbalance on the properties of a lipid membrane while maintaining electroneutrality and equal ionic strength in each water chamber surrounding the lipid bilayer. The unexpected effects of the ions on the structural and electrical properties of the membrane mainly originated from the strong adsorption of Na^+ ions. Even though some experimental observations indirectly support specific interactions of Na^+ ions with the zwitterionic lipid headgroup, the extensive binding and concomitant -70 mV potential drop observed in our simulations also suggests cautious examination of force field parameters and finite size effects. Finally, it is important to note the extremely long "equilibration" time required for this asymmetric (and non-equilibrium) system to reach steady state. In particular, slow processes related to Na^+ headgroup binding, small changes in the bilayer area and, water permeation across the lipid bilayers resulted in relaxation times of approximately 110 ns. Overall, our results show that potential drops across membrane interfaces can be highly sensitive to both ion species and concentration due to specific lipid-ion interactions. This work also suggests that, while the multilamellar membrane simulation methodology pioneered by Sachs, Crozier, and Woolf (111) is an excellent mechanism for simulating asymmetric membrane solution environments and electrostatics, care must be taken in

assessment of force field parameterization, finite size effects, and sampling artifacts when interpreting the simulation results.

Acknowledgments

Chapter 3

Characterization of Perfluorooctylbromide-Based Nanoemulsion Particles Using Atomistic Molecular Dynamics Simulations

3.1   Introduction

Nanoscale particles have been developed for wide range of applications in medicine (163). Medical applications include drug delivery (164), therapy (165; 166), *in vivo* imaging (4; 167), *in vitro* diagnostics (168), biomaterials research (169), and active implants (170). Among those applications, many studies have been focused on the development of nanoparticles as carriers of therapeutic and imaging agents. In nanomedicine, the delivery of therapeutic and imaging agents (cargo) is often accomplished by functionalized nanoscale particles (carriers) to which target-specific ligands are attached. Nanoparticle-based delivery using functionalized particles offers

This chapter is reproduced from my paper published in Physical Chemistry B, July 17, 2010.
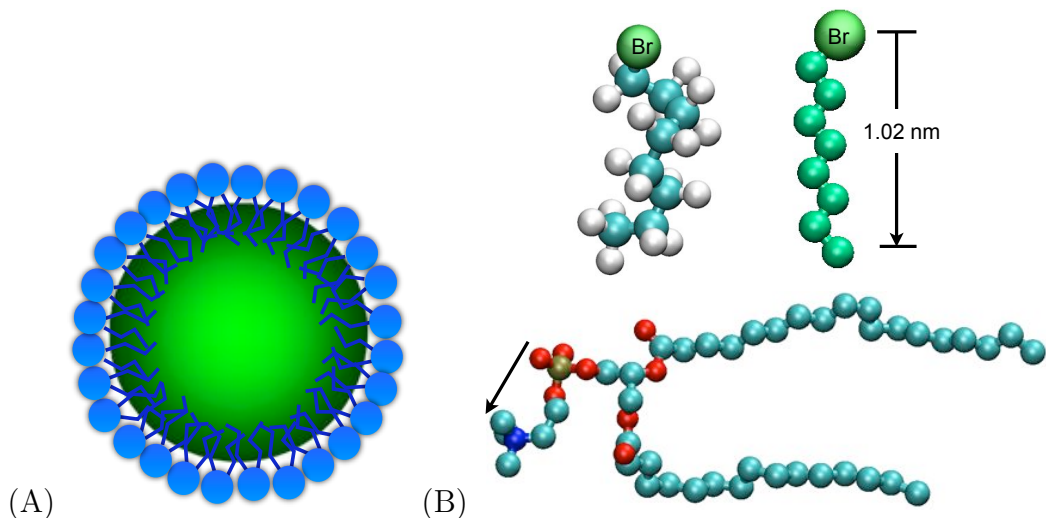
Figure 3.1: The molecular structure of a PFOB-NEP interface and its constituent molecules. A) Schematic diagram of a PFOB-NEP interface. PFOB droplet in water is shown as a green sphere. The emulsifying phospholipid monolayer is shown in blue (sphere for head group and lines for lipid tails). B) The structures of constituting molecules. The structure of PFOB is shown with all atoms (green: Br, cyan: carbon, white: fluorine) on the left and with united atoms on the right (large green: Br, small green: perfluorocarbons CF_2, CF_3). The length of the molecule in its fully extended conformation is 1.02 nm, and the molecular vector is shown with a black arrow. 1-palmitoyl-2-oleoyl-phosphatidylcholine lipid is shown with united atoms at the bottom (cyan: hydrocarbon, red: oxygen, blue: nitrogen, gold: phosphorus). The P-N vector is designated by a black arrow.

advantages over traditional small molecule therapies in that it can improve solubility, protect molecules from premature degradation and non-specific interactions, and increase the effective concentration of drugs in target tissues (171). Such advantages enhance the therapeutic efficacy while decreasing dosages and side effects (5).

One example of functionalized nanoparticles are nanoemulsion particles (NEPs): emulsion droplets with nanoscale dimensions. In particular, perfluorocarbon-based NEPs have been studied and developed for the delivery of therapeutic agents (13) and are the focus of the current study. We are particularly interested in a class of NEPs where the emulsion core is formed by hydrophobic perfluorooctylbromide (PFOB, C_8BrF_{17}) (see Figure 3.1B) and the core is enclosed by a phospholipid monolayer that functions as an emulsifier to stabilize the droplets (13; 35) (see Figure 3.1A). Perfluorocarbons (PFCs) are biologically inert, chemically stable, non-degradable,

non-toxic, and non-volatile, which are all characteristics that make nanoemulsions biocompatible (16; 13; 17; 18; 19). In particular, PFOB has been most commonly used due to its low vapor pressure that will reduce the likelihood of evaporation and the production of pulmonary emphysema (172; 17). In addition, the short half-life of PFOB in the body makes the molecule more practically applicable (18; 19). Finally, the emulsifying phospholipid monolayer is typically derived from either egg- or soybean-lecithin. Such phospholipid preparations have been used for many purposes in cosmetic, food, and drug applications (173).

There are already many biomedical applications of perfluorocarbon-based NEPs for imaging, diagnosis, and therapy. Perfluorocarbon-based NEPs have been used in magnetic resonance imaging (MRI) studies to detect and quantify fibrin protein, to define vessel geometry, and to track stem or progenitor cells(14; 174; 10). Fumagillin-loaded NEPs functionalized to target $\alpha_\nu \beta_3$ integrin significantly suppress neovasculature, thereby inhibiting tumor growth (5). Recently PFOB-NEP has been developed as a platform to deliver melittin, a cytolytic peptide, to cancer cells, illustrating the potential of using cytolytic peptides for chemotherapy (11; 35).

Macroscopic experimental observations suggest a two-step mechanism for delivery of cargo molecules from perfluorocarbon-based NEPs to the cytoplasm of the target cells (47). First, cargo molecules are delivered from NEPs to target plasma membranes via passive diffusion, so called "contact-facilitated" delivery that takes place after the NEPs bind to or closely approach the target cell surface (48). Next, the cargo molecules are transported from the plasma membrane into the cytoplasm by active raft-dependent internalization at the cost of ATP hydrolysis (47). However, the molecular details of both steps are largely unknown and must be understood in order to rationally design particles which achieve optimal delivery efficiency.

Our long term goal is to describe and understand the molecular details of cargo delivery from PFOB-NEP to target membranes via this contact-facilitated mechanism. A lipid complex, resembling the hemifusion stalk intermediate from bilayer fusion, was hypothesized to form between the PFOB-NEP phospholipid monolayer and the outer monolayer of the target cell plasma membrane. Considering the relatively small dimensions of hemifusion stalks (175), we plan to use computational simulations at
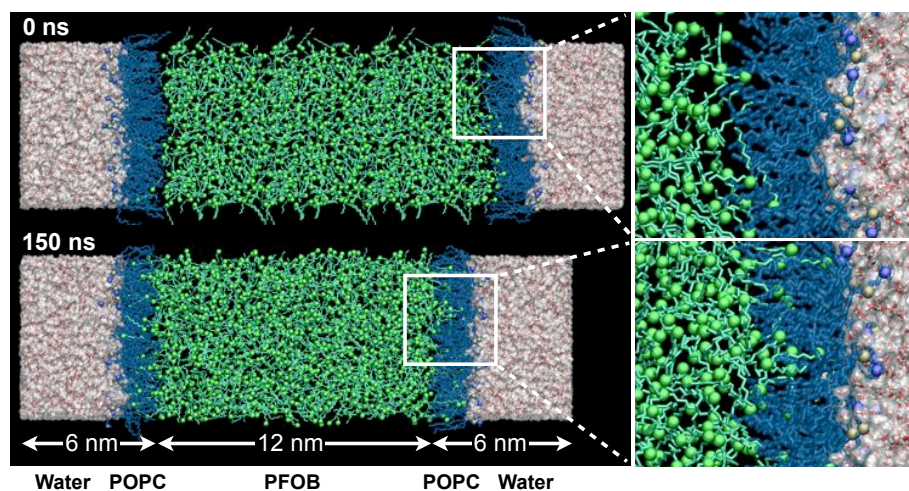
Figure 3.2: Two snapshots of the modeled planar PFOB-NEP interface. The top figure shows the starting structure at time 0 ns, and the bottom one shows the structure at time 150 ns in equilibirum. The zoomed in figures on the right show the intercalation of PFOB into the emulsifying monolayers over time. The POPC monolayers with the head groups oriented toward water regions and with lipid tails oriented toward PFOB region are shown in blue. Water is shown in red and white and PFOB is shown in green.

both atomistic and coarse-grained levels to examine the structural details of this intermediate as well as the functional roles of the component molecules.

As a first step towards this long-term goal, we parameterized the PFOB core at an atomistic level. We simulated a model PFOB-NEP interface in a planar configuration using our new PFOB parameters. The accuracy of our parameters was tested against several experimental measurements while the accuracy of our PFOB-NEP interface was examined using melittin as a molecular ruler in the following manner. Efficient tryptophan (Trp) fluorescence quenching by bromine atoms can occur only when the two molecules appose very closely (176), and we observe this quenching when melittin binds to the surface of PFOB-NEPs (35). In our simulations, PFOB bromine was observed to approach the melittin Trp side chain closely enough to quench Trp fluorescence. This observation provides a viable mechanism for the melittin Trp quenching by resolving a contradiction in assumptions about PFOB-NEP structure (177). Furthermore, the model provides insight into the roles of the molecular components on

PFOB-NEP structure and function, thus offering a basis for future engineering and design of PFOB-NEPs.

3.2 Methods

3.2.1 Parameterization

Force field parameters for perfluorocarbons (CF_2 and CF_3) were developed at the united atom level of resolution for consistency with the Berger et al. lipid force fields (76) commonly used in biomembrane simulations (178; 77; 179; 79). United atom force field parameters for perfluorocarbons were previously developed by Shin et al., using σ values for the Lennard-Jones (LJ) interaction obtained from lattice spacing of solid perfluoroalkanes and ϵ values derived by modulating the ϵ of CH_2-CH_2 and CH_3-CH_3 based on the polarizability of the bond (180). Hariharan and Harris modified the parameters introduced by Shin et al. by decreasing σ and slightly increasing ϵ values (181). Hariharan and Harris reported that the modified parameters reproduced the experimental density within 2% error; however, the surface tension was much larger than the experimentally measured, indicating the parameters still needed improvement (181). Cui et al. independently developed perfluorocarbon parameter sets that had very similar σ values to the Harihan model but a smaller ϵ for CF_2 and a greater ϵ for CF_3. The Cui et al. parameters reproduced experimental density and vapor-liquid equilibria (182); however, these could only reproduce liquid phase densities with 95% accuracy. None of the pre-existing force field parameters modeled pure perfluorocarbons with the accuracy desired for our study; therefore, they were not tested to see if they properly modeled the interface between perfluorinated molecules, emulsifying lipids, and water. In our study, the emulsifying interface between PFOB and water is the most important region because of its role in NEP functions including cargo binding and delivery. Therefore, in this study, new parameter sets were generated with a particular emphasis on PFOB interfacial behavior, while maintaining or improving the thermodynamic behavior described by past force fields.

Table 3.1: The force field parameters of PFOB. The bond stretching and angle bending parameters were borrowed from the OPLS-AA force field (183). The energy p rofiles along the torsional angle were calculated from model molecules: $BrCF_2$-$CF_2CF_3^a$ and CF_3CF_2-$CF_2CF_3^b$.

Bond Stretching Parameters						
bond					$k_b(\text{kJ mol}^{-1} \text{ nm}^{-2})$	$r_0(\text{nm})$
Br-PC					205016.0	0.19450
PC-PC					224262.4	0.15290
PC-PEC					224262.4	0.15290
Angle Bending Parameters						
angle					$k_0(\text{kJ mol}^{-1} \text{ rad}^{-2})$	$\theta_0(\text{deg})$
Br-PC-PC					577.392	110.0
PC-PC-PC					488.273	112.7
PC-PC-PEC					488.273	112.7
Coefficients of the Torsional Potential Energy Function (kJ mol^{-1})						
dihedral angle	C_0	C_1	C_2	C_3	C_4	C_5
Br-PC-PC-PC^a	-21.5787	22.5726	0.9644	-29.3050	2.8832	-10.8271
PC-PC-PC-PC^b	-22.1519	2.6823	-7.1261	12.2544	14.8433	-31.0271
PC-PC-PC-PEC^b	-22.1519	2.6823	-7.1261	12.2544	14.8433	-31.0271
Lennard-Jones Parameters for Non-Bonded Interactions						
atom type					σ (nm)	ϵ (kJ mol^{-1})
PC					0.4824	0.3367
PEC					0.4824	0.4789
Partial Charges for Long-Range Coulomb Interactions						
atom name						charge (q)
Br1						0.065
PC2						-0.205
PC3						0.03
PC4						0.03
PC5						0.03
PC6						0.03
PC7						0.03
PC8						0.02
PEC9						-0.03

PFOB molecules were modeled with an explicit bromine atom and two united atom types: PC (intermediate CF_2) and PEC (terminal CF_3). Bond and angle terms were taken from the OPLS-AA force field (183). Torsional parameters were derived from the rotational energy profiles of two model compounds: Br-CF_2-CF_2-CF_3 and CF_3-CF_2-CF_2-CF_3. Single point energies were calculated after structural optimization with torsional angles fixed at $15°$ increments, using *ab initio* calculations with the B3LYP functional in combination with the $_{cc-p}VTZ$-PP basis set (184). The coefficients of the Ryckaert-Bellemans (RB) dihedral potential function (185) were fit to the potential profiles by a linear least squares method (see p.132 figure 7.1 of the Supplementary materials) .

Electrostatic potential (ESP) charges (186) were determined for an optimized PFOB molecule in vacuum by *ab initio* calculations with the B3LYP functional in combination with the $_{cc-p}PVTZ$-PP basis set. Charges for the united atoms were obtained by summing the partial charges of the atoms comprising each united atom. The LJ parameters for PC and PEC united atoms were taken and optimized from the previous work (180); in particular, the size parameters (σ) were systematically varied to reproduce the density and heat of vaporization of liquid PFOB. The resulting force field parameters are summarized in Table 3.1, while tests of these parameters are summarized in the Table 3.2 the details of the tests are described in the Supplementary materials. We observed much better accuracy in the united-atom perfluoromethane solvation energies in united atom *n*-hexane models rather than an all-atom perfluoromethane model. The united atom *n*-hexane models closely resemble the tail region of the lipid models used in our simulations. Therefore, these results support the compatibility of our model with the current lipid models.

Table 3.2: The bulk properties of liquid PFOB. The references for each experimental bulk properties are Riess et al.(21) and Andre et al. (19) for density (ρ), Riess et al. (21), Gregor et al. (187), Faithful et al. (188) for heat of vaporization ($\Delta_{vap}H$), Song et al. (189) for solvation free energy of CF_4 in liquid *n*-hexane (ΔG).

Properties	Experiment	Simulation
ρ (kg L^{-1})	1.925 ($\pm$ 0.007)	1.891 ($\pm$ 0.001)
$\Delta_{vap}H$ (kJ mol^{-1})	42.67 ($\pm$ 1.276)	41.05 ($\pm$ 0.26)
ΔG (kJ mol^{-1})	2.056	2.00 ($\pm$ 0.02)

3.2.2   Simulations

Initial structures

Planar PFOB-based nanoemulsion interface model   A PFOB-based nanoemulsion particle (PFOB-NEP) interface was modeled in a planar configuration (see Figure 3.2). A similar "sandwich" topology was previously used by other researchers to simulate an emulsion composed of a triglyceride core and a phospholipid monolayer in water (190). The interface model was constructed from structures of POPC monolayers composed of 64 1-palmitoyl-2-oleoyl phosphatidylcholine (POPC) lipids extracted from a previous POPC bilayer simulation (79). These two POPC monolayers were then placed in a periodic box in an arrangement that separated lipid tails by 15.3 nm and the headgroups by 6 nm. The space flanked by tails (inside) was filled with 1310 PFOB molecules while the other space facing the head groups (outside) was filled with 11,678 water molecules. The system was fully hydrated with 91.2 waters per lipid (191). The dimensions of the box were 6.2 nm x 7.2 nm x 27.1 nm along the x, y and z directions. Two replica simulations were performed for 150 ns. This system will be referred to as PFOB-NEP throughout this report.

Melittin peptides bound to the planar PFOB-NEP interface   The initial structure was prepared with an equilibrated PFOB-NEP interface structure obtained from the simulations described above and a model of bilayer-bound melittin provided by the Hristova and White groups.(192) A single melittin peptide was inserted into each POPC monolayer to the depth of the glycerol groups (see Figure 3.11) as suggested by experimental results (192). The peptide was inserted so that its non-polar residues faced the hydrophobic interior while its polar residues faced the NEP-water interface. POPC lipids that significantly overlapped with the inserted melittin peptides were deleted, leaving 55 POPC lipids remaining in each monolayer. No PFOB molecules had direct contact with the inserted melittin peptides and hence none of them were deleted. 19,958 water molecules were added to solvate the system. To neutralize the +5 formal charge of each melittin peptide, ten randomly chosen water molecules were replaced by chloride ions. The hydration level of the system was approximately 90 water molecules per lipid. The dimensions of the systems were 6.0nm

x 6.9 nm x 24.8 nm along the x, y and z directions. A single simulation was carried out for 190 ns.

Force field parameters

POPC was modeled with the united atom force field parameters optimized by Berger et al. (76) and Chiu et al. (193). Water was modeled by the simple point charge SPC model (194).

Generally mixing of two different force fields is not recommended and sometimes not feasible due to different functional forms and combination rules. However, Tieleman et al. (77) have reported that OPLS-AA (195) all-atom protein representations could be successfully used in combination with the united-atom lipid model described above. In our system, such a combination of parameters prevents artificial condensation of the membrane by eliminating overly favorable lipid-protein interactions; otherwise, use of standard GROMOS united atom types may cause significant condensation of the membrane.(77) Therefore, the melittin peptides used in these simulations were modeled with the OPLS-AA force field (195). The combination of these two different force fields for lipids and peptides was made possible by using a half-epsilon and double pair list method (82) to resolve the different 1-4 interaction scaling factors used by the two force fields (92). Our simulation used OPLS-AA combination rules; however, the parameters for van der Waals (vdW) interaction energy for the 1-4 interaction pairs were listed by their half magnitude in the parameter file for non-bonded interactions. The 1-4 interaction pair list was repeated twice in the lipid topology file. By doing so, the 1-4 interaction energy of lipid that originally use GROMACS combination rule could be scaled properly while the combination rule of OPLS-AA force field was used. This method was tested using both a pure POPC bilayer and bulk PFOB, and both the bilayer area and the bulk PFOB density were identical within error to identical simulations using standard combination rules (data not shown).

Simulation parameters

Molecular dynamics simulations and analyses of the trajectory were performed with GROMACS version 4.0 (92). The starting structures were subjected to previously described equilibration procedures (78). First, an energy minimization was performed using a steepest descent method and the system was then gradually heated from 50 K to 303 K through a series of short molecular dynamics (MD) simulations. After the system reached the production temperature of 303 K, the MD simulation was continued for at least 150 ns of production simulation. The cutoffs for LJ interaction and for direct space for electrostatic interactions were 1.0 nm. The particle-mesh Ewald method (196) with conducting boundary conditions was used for long-range electrostatic interactions. The simulation was performed in an isobaric-isothermal ensemble (NpT). A Parrinello-Rahman barostat (197) with 2 ps coupling time was used to maintain the system pressure at 1 bar. The pressure coupling type varied depending on the systems: isotropic pressure coupling was used for simulations of bulk solutions, semiisotropic for simulations of PFOB-NEP interface and POPC bilayer systems, and anisotropic for the simulation of melittin bound membranes. A Nosé-Hoover thermostat (198) with 0.5 ps coupling frequency was applied to each molecule type separately. Hydrogen atoms bonded to heavy atoms were constrained with the LINCS algorithm (199), allowing a 2 fs time step to be used.

3.2.3   Analysis

Block averaging

To perform statistical analysis, each trajectory was divided into small blocks with the block size chosen based on the standard error so that each block was independent of one another (200). The standard error $\varepsilon(f, n)$ in observable f for a block of length n was calculated according to the formula $\varepsilon(f, n) = \sigma/\sqrt{M}$, where n is the block length, σ is mean standard deviation, and M is the number of blocks in the simulation. When the block size is large enough; e.g., much greater than the correlation time of an observable, the standard errors become independent of the block size and the true

standard error is obtained. The block size for sub-sampling was determined by the value of n where $\varepsilon(f, n)$ for observable f reached a plateau.

3.3   Results

3.3.1   Characterization of the PFOB-NEP interface

Equilibration and sub-sampling

Two independent simulations of the PFOB-NEP interface shown in Figure 3.2 were performed for 150 ns; a control POPC bilayer was simulated for 300 ns. After equilibration, the PFOB in the PFOB-NEP "sandwich" became denser than in the more loosely distributed initial state. This change was accompanied by the intercalation of PFOB into the monolayer as shown in the right panel of Figure 3.2 and in the number density profile of the molecules along the z-axis (Figure 3.3).

The cross-sectional area of total membranes was used to determine the equilibration of the system. The three simulated systems showed no significant area drifts throughout the simulations, implying that the systems quickly reached equilibrium during the temperature equilibration steps (see p.139 figure 7.5 of the Supplementary materials). To further ensure unbiased results, the first 10 ns of each trajectory was discarded for analysis to remove any possible bias from the starting structure.

The fluctuation of the cross-sectional area of total membrane was also used to determine the statistically-independent block size for each trajectory to calculate standard error as explained in the section 3.2.3. For the two PFOB-NEP interface simulations, the standard error reached a plateau with a 14 ns block size and, beyond that size, the increase in standard errors was marginal. Therefore, 10 independent blocks of 14 ns each were generated from each trajectory and results from each block were combined to compute means and standard errors.

The same test was performed for the control POPC bilayer, and with 14 ns block size, the standard error stopped increasing drastically and only small increases were
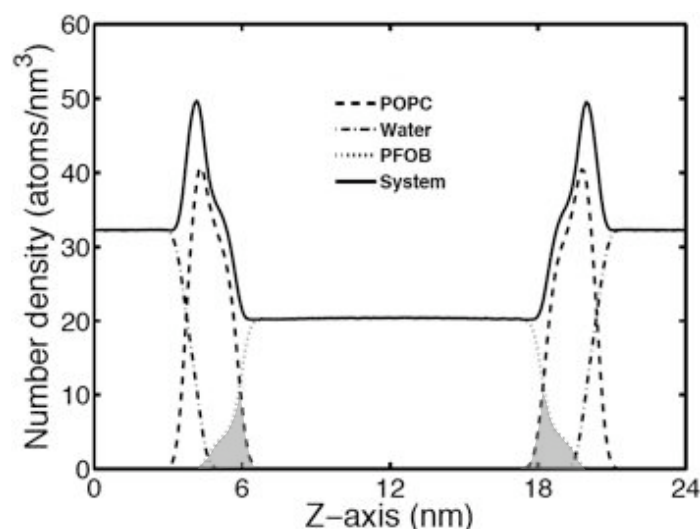
Figure 3.3: The number densities of each component of the system along the z-axis are shown for whole system (solid), POPC monolayer (dashed), water (dotted dash), and PFOB (dotted). The shaded regions in gray mark the density overlap between POPC lipids and PFOB.

observed for much larger block sizes. With a 14 ns block size, 20 statistically independent blocks were obtained from the control POPC bilayer simulation. The observables calculated in this report were averaged over the statistically independent blocks as determined in this section.

NEP-water interface geometry

Figure 3.4 shows that the width δ of PFOB and SPC water at the emulsion interface increases substantially as compared with the pure PFOB-water interface shown in p.137 Figure 7.3 of the Supplementary materials. Additionally, the PFOB and water density profiles overlap only slightly in the presence of the POPC monolayer demonstrating the effectiveness of the stabilizing monolayer at separating the hydrophobic PFOB molecules from the aqueous environment.

Monolayer density distribution   The number density profiles of the monolayer along the z-axis were determined to assess structural changes in the POPC monolayers. Two density profiles of the PFOB-NEP interface and the control POPC bilayer
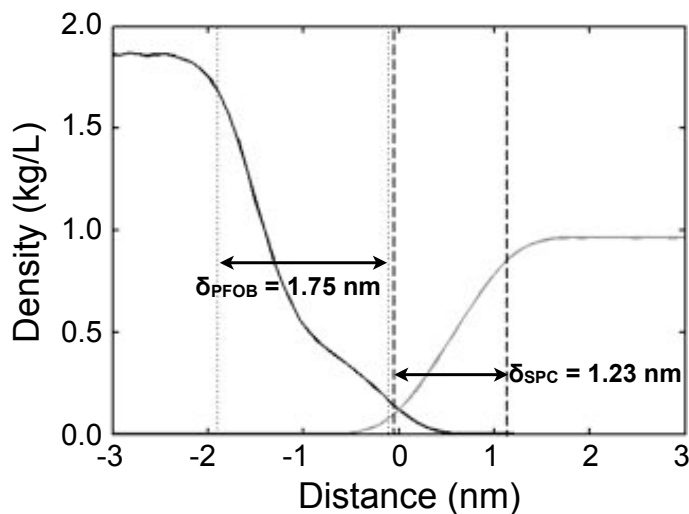
Figure 3.4: Phase separation of PFOB in water in the presence of an emulsifying POPC monolayer. The mass densities of PFOB (green) and water (red) near the interface are shown. The vertical dotted lines show the δ of PFOB interface (δ_{PFOB}), and the vertical dashed lines show that of water interface (δ_{SPC}). The thickness of the δ region was 1.75 nm for PFOB interface and 1.23 nm for water interface, and no overlap is observed.

were aligned such that the maximum density of each was placed at zero on the z-axis. Figure 3.5 shows that the thickness of the monolayer is greater in the PFOB-NEP interface than in individual control bilayer leaflets. The largest increase in thickness was observed in the tail region of the PFOB-NEP interface monolayer. The maxima of the density profiles of different parts of lipids shifted outwards as compared to those of the control POPC bilayer. The peak of choline group shifted toward the water side and terminal methyl group shifted toward the lipid tail side. These density shifts are consistent with the more parallel orientation of the P-N vector to the bilayer normal (see Figure 3.8) and more ordered lipid tails (see Figure 3.7).

Total area The cross-sectional area of a lipid molecule has been a commonly used metric to assess and compare membranes under different physical environments or with different force field parameters (201; 79; 202) However, as described previously (79), it is not a trivial problem to measure the cross-sectional area of individual lipids in inhomogeneous membranes. As described above, the POPC monolayers of PFOB-NEP interface were inhomogeneous due to the intercalation of PFOB. Therefore, the
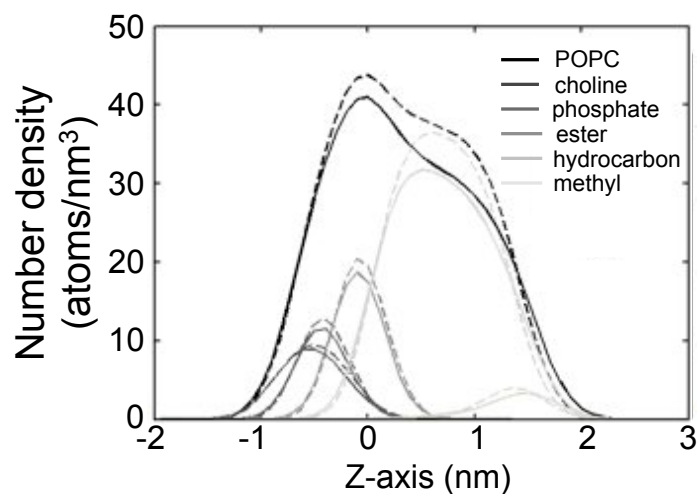
Figure 3.5: The monolayer thickness changes were examined by the number densities of moieties of POPC lipid. The number densities of control POPC bilayer are plotted with dashed lines, and those of PFOB-NEP interface with solid lines along the z-axis with the same color codes as shown in the figure. To ease the comparison, two profiles are aligned with their maximum densities to be at the zero point on the z-axis. The whole POPC monolayer is shown in black, and lipid moieties in gray colors as shown in the figure.

cross-sectional area of the total monolayer, which corresponds to the lateral area (XY-plane) of the simulation box, was measured and compared with that of the control POPC bilayer instead. The cross-sectional area of 128 POPC bilayer (41.0 ± 0.1 nm²) gives a per-lipid area of 0.641 ± 0.001 nm² which is in good agreement with both experiment (201) and with the results of other simulations (202). The expansion of the cross-sectional total membrane area of PFOB-NEP interface compared to the control POPC bilayer is shown in Figure 3.6A. The mean areas and standard errors obtained from the independent blocks were 44.42 ± 0.17 for the 64-lipid PFOB-NEP interface and the increase was significant (99.9% confidence level). The result agrees qualitatively with experimental Langmuir results that show total monolayer area expansion upon the application of gaseous PFOB to the hydrophobic tail side of the monolayer (203).

Probe-accessible surface area Probe-accessible surface area (ASA) was measured using a 1.4 Å probe to examine the contribution of each molecule to the area expansion. The contributions of hydrophilic and hydrophobic parts of the system

to the total ASA were calculated separately. The hydrophilic parts consisted of all POPC headgroup atoms, while the hydrophobic parts consisted of lipid tails and PFOB.

In agreement with the total membrane area results, the total ASA of the PFOB-NEP interface was greater than that of control POPC bilayer. The increase in the total ASA could be fully attributed to the increased hydrophilic ASA; hydrophobic ASA decreased in the PFOB-NEP interface. The lower inset of Figure 3.6B shows the contribution of POPC lipid tails and PFOB to the hydrophobic ASA. The surface exposure of lipid tails was substantially decreased while a small portion of the hydrophobic surface area was contributed by PFOB molecules at the PFOB-NEP interface. The reduction in hydrophobic ASA could be explained by the intercalation of PFOB in between the lipid tails. The void volume in between lipid tails in POPC bilayer provides continuous paths through which water probe could travel into the hydrophobic interior of POPC bilayer; however, those paths were blocked by intercalated PFOB molecules in the PFOB-NEP interface which resulted in a substantially decreased hydrophobic surface area.

Order parameters Lipid tail order parameters provide important details about membrane structure (79; 204). Figure 3.7 clearly shows that tail order parameters for POFB-NEP interface lipids increased, with respect to POPC bilayers, for both chains all along the tail length. This increase was most prominent near the ends of the lipid tails. In the control bilayer, the ends of lipid tails are more flexible and have smaller order parameters due to the void volume at the center of bilayers. In the PFOB-NEP interface, no void volume exists at the hydrophobic region and, hence, conformational flexibility decreases more substantially near the termini of lipid tails. Increased order parameters indicates that POPC molecules are in more extended conformations and occupy a smaller cross-sectional area per lipid. This result clearly supports our conclusion that the expanded total monolayer area is due to the intercalation of PFOB molecules into the POPC monolayers and not due to the disordering of POPC.

Head group orientation The P-N vector (see Figure 3.1B) connects the POPC phosphorus and nitrogen atoms and reorients in response to environmental changes. The orientation was computed to obtain $\cos\theta$ where θ is the angle between the mean

(A)

(B)
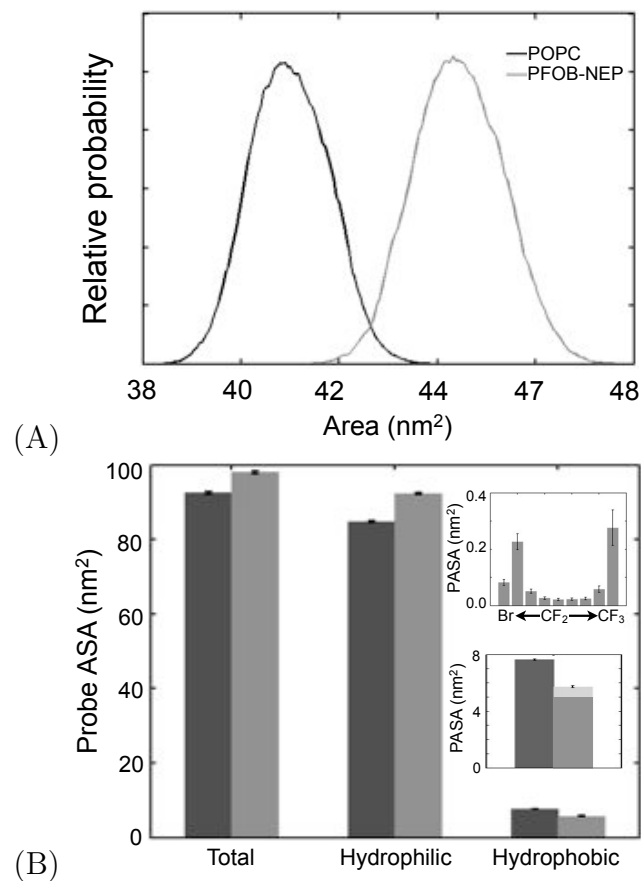
Figure 3.6: System area change. A) The distributions of the cross-sectional area of the total monolayer are plotted for control POPC bilayer (black) and PFOB-NEP interface (gray). B) The probe-accessible surface area (ASA) of control POPC bilayer (dark gray) and PFOB-NEP interface (light gray) are plotted. The contributions from hydrophilic and hydrophobic parts of each system are plotted separately. The top insert shows the contribution of each united atom of PFOB starting from Br terminus to CF_3 to the hydrophobic probe-ASA of PFOB-NEP interface. The bottom insert shows the contribution of each component to hydrophobic probe ASA. The left bar shows the sole contribution of POPC (dark gray) in control POPC, and the right bar shows that the contribution of both POPC (light gray) and PFOB (silver) in PFOB-NEP interface.
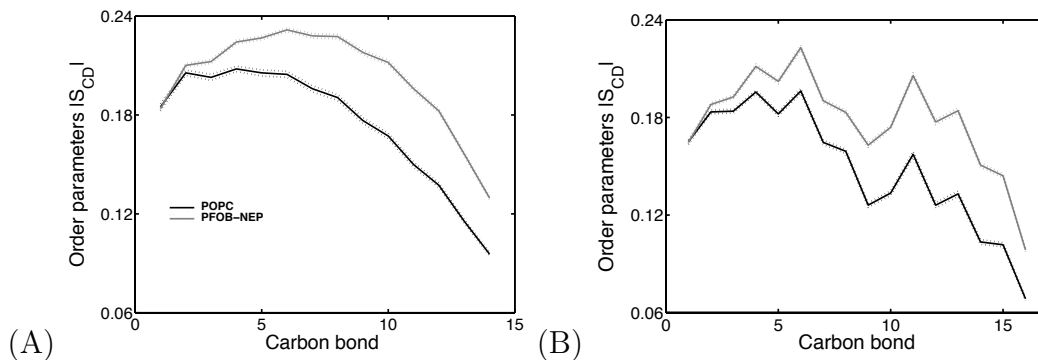
Figure 3.7: Lipid order parameters. A) Tail orders of the sn-1 saturated palmitoyl chains are plotted for control POPC bilayer (black) and PFOB-NEP interface (gray). The means are connected by solid lines with one standard error deviations by dotted lines. B) Tail orders of the sn-2 unsaturated oleoyl chains are plotted with the same line types and color codes.

P-N vector and the monolayer normal. Larger values of $\cos\theta$ indicate a P-N vector orientation that is more parallel with respect to the monolayer normal. Figure 3.8 shows significantly greater $\cos\theta$ value in the PFOB-NEP interface as compared to POPC bilayers. Decreased electrostatic repulsion among the head group dipoles due to expanded monolayer area likely caused this more parallel distribution of P-N vectors. While this change in orientation was significant, no increased net polarization density was measured (see p.140 figure 7.6 in the Supplementary materials), indicating compensatory polarization changes in the rest of the system.

Characterization of PFOB structure

Shape Conformational variation of PFOB along the z-axis was examined. The short chain length of PFOB resulted in no significant variation of the radius of gyration along the z-axis (data not shown). Therefore, the average conformation of PFOB along the z-axis was examined by assessing the mean end-to-end length from Br to CF_3 (see Figure 3.9B). The mean end-to-end length was 1.02 nm in a fully extended conformation and 0.992 ± 0.002 nm for bulk PFOB. To obtain a profile of PFOB in the emulsion environment, the simulation system was divided into slabs of 0.25 nm thickness along the z-axis, and then mean length was computed from the average over the molecules in an individual slab. Figure 3.9A shows that the PFOB conformation
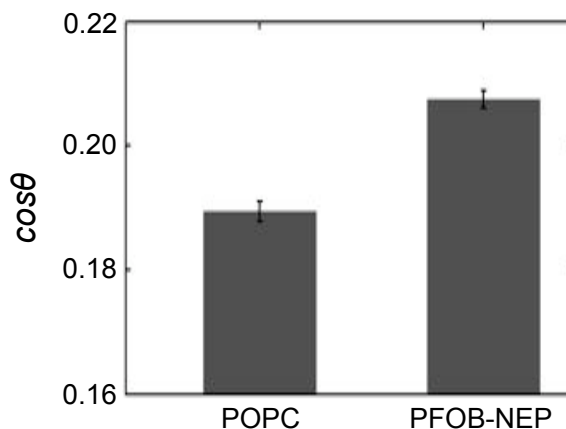
Figure 3.8: P-N vector orientation. The mean and one standard error deviation of the P-N vector orientation to the monolayer normal are shown for control POPC bilayer and PFOB-NEP interface.

has small but significant variations along the z-axis. The PFOB length was longer within the monolayers, indicating that more PFOBs were in extended conformations inside of the monolayers. On the other hand, the mean length was shortest near the lipid termini where the mixing of lipid tails and PFOB occurs. The mean end-to-end length at the middle of the PFOB-NEP interface was comparable to the mean length of bulk PFOB, indicating that the direct influence of the emulsifying monolayers vanished in the middle of the PFOB-NEP interface.

Orientation The mean orientation of PFOB along the z-axis was also examined. The molecular vector of PFOB is defined in Figure 3.1B starting from Br and pointing to the terminal CF_3 atom. The orientation was measured from the normalized inner product of the PFOB molecular vector with a unit vector along the z-axis. The orientation of every PFOB was averaged over slabs of 0.25 nm thickness along the z-axis and plotted in Figure 3.9B.

The plot shows that PFOB inside and adjacent to the monolayers was preferentially oriented. The maximum peaks with the $\cos \theta = 0.3$ appeared inside of the monolayers, showing that PFOB preferentially orients with its Br atom pointing to the hydrophilic surface of the monolayer. The preferential orientations vanished very quickly outside of the monolayers, and PFOB was randomly oriented with the $\cos \theta$ zero in the middle of the PFOB-NEP interface, which again supports the assertion that the PFOB-NEP

sandwich geometry can be appropriately used to model larger nanoemulsion droplet interfaces.

The preferentially oriented PFOB in the monolayers contributed additional non-zero charge density to the system as shown in Figure 3.9C. The charge attributed to the preferentially oriented PFOB generated additional positive electrostatic potential inside of the PFOB-NEP interface, which will be discussed in the section 3.3.1.

Electrostatic potential profile

The charge density profiles of the pure POPC bilayer (top) and the PFOB-NEP interface (middle and bottom) are shown in Figure 3.10A. The overall charge density profiles of the pure POPC bilayer and that of the PFOB-NEP monolayer are almost indistinguishable. The PFOB charge densities of the PFOB-NEP interface are plotted separately due to their much smaller scale compared to those of POPC and water. The sinusoidal fluctuation of PFOB charge in and near the POPC monolayer was observed and attributed to the polarized molecular orientation of PFOB molecules discussed earlier in the previous section (3.3.1).

The electrostatic potential was calculated by the double integration of the charge densities along the z-axis as shown in the following equation (205; 206).

$$\phi(z) - \phi(0) = -\frac{1}{\epsilon} \int_0^z \left(\int_0^{z'} \rho(z'')dz'' + D_0 \right) dz', \qquad (3.1)$$

where ϵ is a *homogeneous* dielectric constant which is ϵ_0 for analysis of the atomistic system, and $\rho(z)$ is the charge density. The displacement constant D_0 for net neutral systems to impose the conducting boundary condition is defined by (205; 206)

$$D_0 = -\frac{1}{L} \int_0^L \int_0^z \rho(z'')dz''dz, \qquad (3.2)$$

Results are shown in Figure 3.10B. The statistical errors in the electrostatic potential along the z-axis were small and are not shown for clarity. The black curves in the figure showed that electrostatic potentials of the PFOB-NEP interface and POPC bilayer systems were substantially different. The positive potential in the interior of
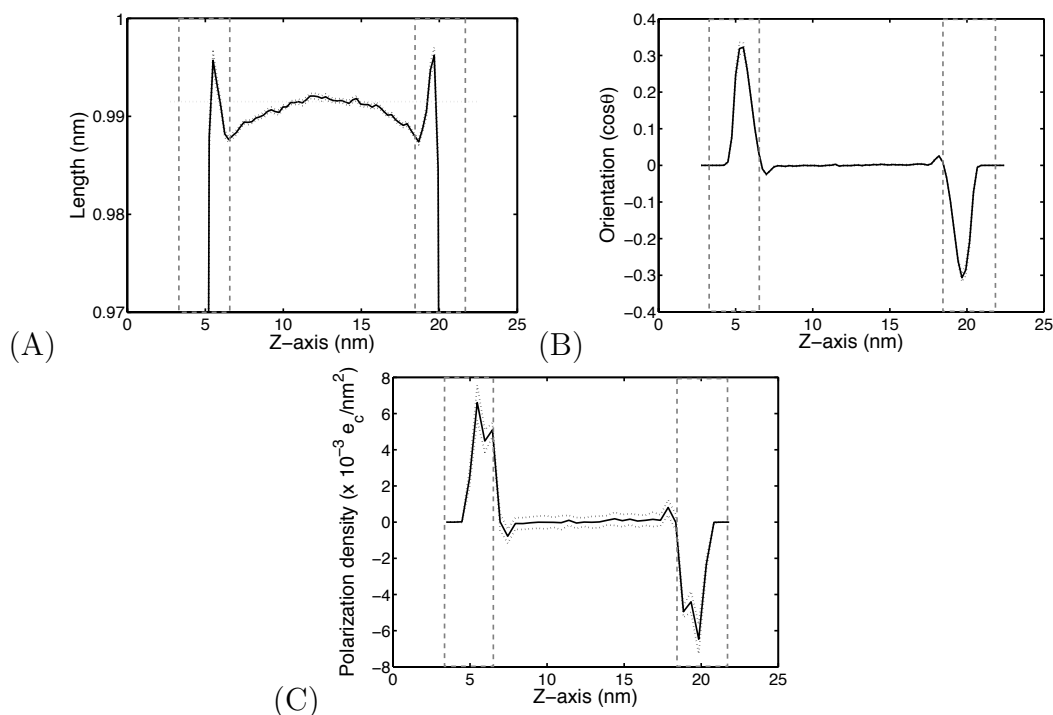
Figure 3.9: The structures of PFOB within PFOB-NEP interface. A) The mean molecular end-to-end length of PFOB in each slab of 0.2 nm thickness along the z-axis was calculated. A horizontal dotted line in gray shows the mean length of PFOB in bulk. B) The mean $\cos\theta$, where the θ is an angle between z-axis and the molecular axis of each PFOB molecule, was calculated along the z-axis. The molecular axis was a vector starting from the Br atom to the terminal CF_3. C) The polarization density of the PFOB weak dipole is plotted along the z-axis. Dashed-gray boxes mark the locations of the two POPC monolayers. The mean is plotted by a solid line and the one standard error deviations are by dashed lines.

PFOB-NEP was much greater than the potential at the hydrophobic interior of pure POPC bilayer. The potentials due to different molecules were estimated separately to identify the origin of this positive potential. It was observed that the potentials due to both POPC and water of the PFOB-NEP interface system were comparable to the potentials of pure POPC bilayer system. The additional positive potential was attributed solely to the dipolar charge distribution of PFOB due to their polarized orientation near the PFOB-NEP monolayer.

Another minor difference between the two systems is the slightly lower potential at the boundary peak. The decreased potential can be explained by the greater total membrane area and concomitantly decreased charge density in the PFOB-NEP interface system.

3.3.2 Testing the model with melittin tryptophan fluorescence quenching

Melittin was simulated to test if the modeled system agrees with experimental results in that Trp fluorescence was quenched upon melittin binding on the surface of PFOB-NEP (35) and to elucidate the molecular mechanism of the quenching phenomenon. The quenching of Trp fluorescence by bromine atom is known to occur within very short distances via dynamics quenching mechanism (176; 207). Therefore, in order for quenching to occur, bromine atoms must directly collide with Trp side chain.

A simulation with melittin at the NEP interface was performed for 190 ns as described in the Methods sections 3.2.2 and 3.2.2. The initial structure and position of melittin was based on x-ray diffraction results which show that, at low mole fractions, melittin positions itself parallel to the membrane surface at the depth of the glycerol groups and orients its hydrophobic residues towards the hydrophobic interior of the membrane (192). Figure 3.11A shows the structure of the system after 190 ns of simulation. Figure 3.11B shows that melittin maintains a helical conformation, in agreement with experiments, (192) and that the Trp side chain faces the interior of the PFOB-NEP interface.
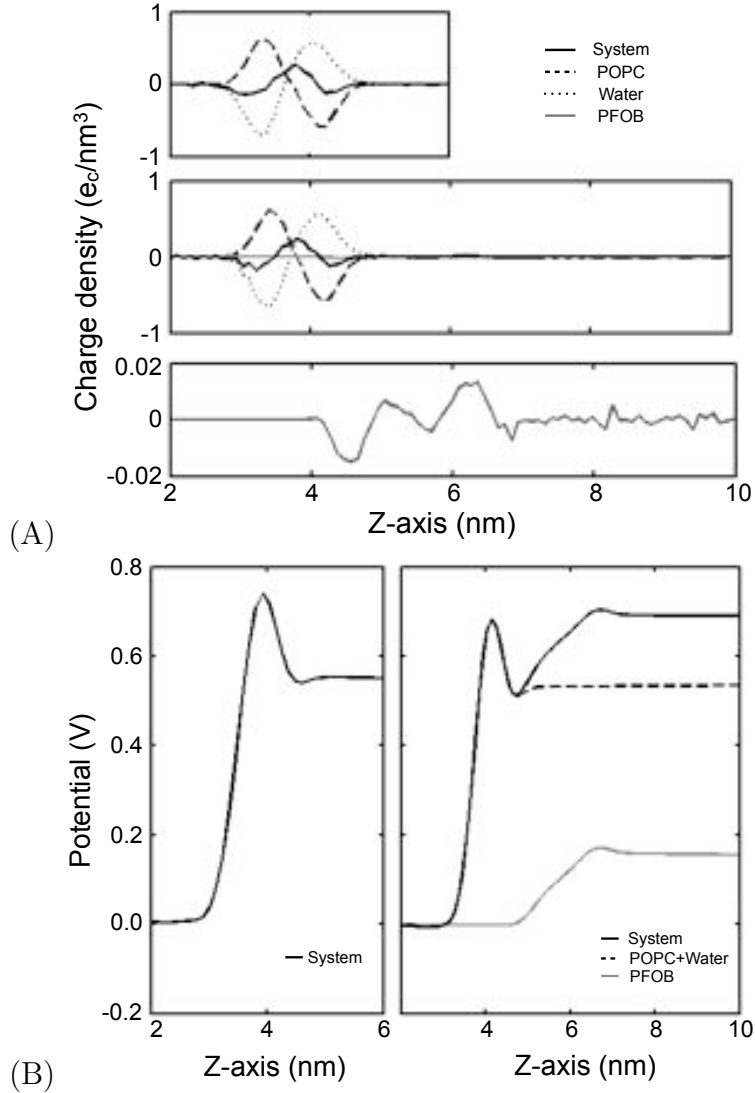
Figure 3.10: Charge densities and electrostatic potentials. To ease the comparison, a half of the system along the z-axis is plotted. A) The charge densities of whole system and individual components are plotted for control POPC (top) and for PFOB-NEP interface (middle). The charge density of PFOB of the PFOB-NEP interface is plotted separately (bottom) to be noticeable. The charge density of the whole system is shown in a solid black line, POPC lipids in a dashed black line, water in a dotted black line, and PFOB in a solid gray line. B) Electrostatic membrane potentials are plotted. The potential of the whole system of control POPC bilayer is plotted on the left panel. The potential of the whole system (black sold) of the PFOB-NEP interface is shown on the right panel. The potential due to PFOB was plotted separately in solid gray line, and the potential generated by POPC monolayer and water is shown in dashed black line.

60

The radial distribution of bromine atoms around each Trp side chain was computed to assess the likelihood of quenching, and the radial distribution profiles of both peptides are shown in Figure 3.11C. The density of bromine atoms appeared at distance shorter or near the direct contact between the Trp side chain and bromine atoms considering the radii of the two (approximately 0.35 nm and 0.33 nm respectively) (207). Such close apposition is made possible only through the intercalation of PFOB molecules into the monolayers and provides a molecular explanation of Trp quenching upon melittin binding to PFOB-NEP interfaces. This result, in turn, supports our modeled PFOB-NEP interface structure characterized by the PFOB intercalation.

3.4 Discussion

In this study, a new set of force field parameters for PFOB was developed to study the structural properties of a PFOB-NEP interface. The atomistic simulations show that PFOB intercalates into the emulsifying monolayers and causes unique structural changes at the NEP-water interfaces. Due to the intercalation, the structures and properties of the monolayer are altered, becoming distinct from those of similarly composed bilayers. Also, the orientation and conformation of PFOB was different within and near the monolayers as compared with bulk PFOB or the center of the PFOB-NEP interface. Such changes likely contribute to the functions of PFOB-NEP interface of cargo loading as well as cargo delivery.

3.4.1 United atom model for PFOB

The new set of force field parameters preserved important characteristics of PFOB both in bulk and at the phase-separated interface between water and PFOB both in the absence and presence of emulsifying phospholipid monolayer. The bulk density and heat of vaporization were reproduced in an acceptable accuracy. The strong hydrophobicity of the model PFOB generates a sharp interface in water and the computed surface tension from the interfaces was close to the experimentally measured value. While perfluorocarbon is regarded as lipophobic (177), the unfavorable solvation free energy of a perfluoromethane in liquid n-hexane (2.06 kJ/mol) (189) was less
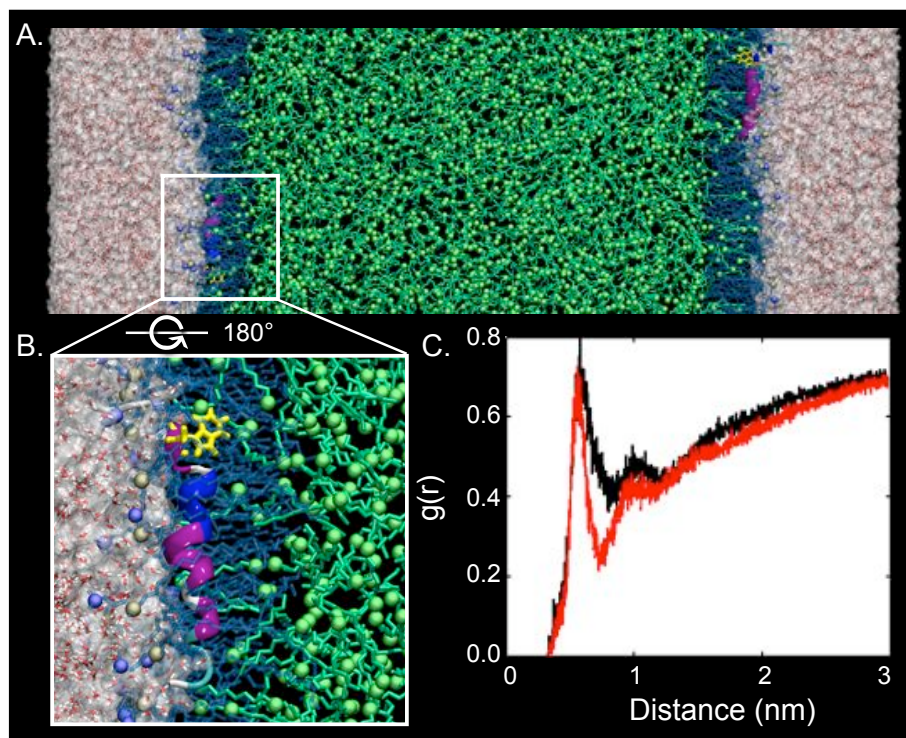
Figure 3.11: Structure of melittin bound to the POPC monolayers of the PFOB-NEP interface. A) Two melittin peptides, one in each POPC monolayer, are shown. B) A melittin peptide in the bottom POPC monolayer is shown in detail. Melittin peptides are drawn by a ribbon diagram; the parts in α-helix conformations are shown in magenta, 3-10 helix in blue, turn in green, coil in while. Trp residues are shown in yellow sticks. POPC lipids are drawn with blue lines for tails and with gray and blue balls for head group atoms. Br atom of PFOB is shown in a green ball with perfluorinated chain part in a green stick. Water is shown as white (hydrogen) and red (oxygen) sticks. C) The radial distributions of Br atoms about Trp side chain of melittin in the top (black) and bottom (red) leaflet are plotted as a function distance between the tryptophan side chain and Br atoms.

than thermal energy (2.48 kJ/mol) at room temperature. The strong hydrophobicity with relatively moderate lipophobicity of perfluorocarbon is important to form stable emulsions. Our parameters preserved the weakly unfavorable interaction between perfluorocarbon united atom and the united *n*-hexane and, as a result, substantial mixing between PFOB and lipid tails is observed in our simulation.

3.4.2 System configuration caveats

The interface between PFOB and water was planar and was not allowed to have any large scale curvature due to the periodic boundary conditions and small lateral dimensions in our simulations. However, this planar interface can be considered to be equivalent to small patches on the surface of larger PFOB-NEPs with radii of a few hundred nanometers. Furthermore, because we observe a return to bulk PFOB behavior in the center of our sandwich simulation geometries, they can therefore be considered to mimic the interface of more realistic PFOB-NEPs. A similar simplification scheme has been used to model triglyceride-based emulsions (190) and to mimic cells that have asymmetric ionic conditions inside and outside of the cell by putting two bilayers in a simulation box (78; 206; 179).

In the current study, structural differences in the emulsifying monolayer of the PFOB-NEP have been assessed through comparison with a lipid bilayer of the same lipid composition. As a control, a bilayer is less topologically relevant than the monolayer at the air/water interface, which has been modeled recently.(208; 209) However, a bilayer has been used as a control in our study to have a consistent comparison with future simulations designed to understand the functional mechanism of cargo delivery by using PFOB-NEPs as platforms. In particular, we wish to understand the differential binding of cargo, such as melittin peptides, to monolayers of PFOB-NEPs and the target bilayer membranes. Therefore, comparisons with a bilayer will provide us not only consistency with the future work but also more insight to understand the functional mechanisms of PFOB-NEPs.

3.4.3 PFOB intercalation into phospholipid monolayer

Substantial intercalation of PFOB into POPC monolayers was the most remarkable result of these simulations, and is somewhat contradictory to the expectation that PFOB and lipid tail would have a clear interface due to the lipophobicity of perfluorocarbons (177). However, models based on this expectation cannot explain the Trp fluorescence quenching that requires direct contact between the side chain and bromine atoms. Gerber et al examined the influence of gaseous perfluorocarbons (gFCs) on Langmuir DPPC monolayers and showed that gFCs had a strong fluidizing effect on the monolayer, expanded the total area, with more pronounced effects if the gFCs were linear (203). The results indicated that gFC interacts with the lipid tails. The fact that linear gFCs are more effective at causing such changes strongly suggests that the effect is mediated by the intercalation of gFCs with the lipid tails. Yokoyama et al tested the miscibility of perfluorocarbons of various lengths (FC_n) and showed that the length of FC_n with respect to the lipid tail length is important in determining their miscibility: FC_n shorter than the lipid tail is miscible with lipid tails, miscibility drops as the FC_n length becomes closer to the tail length, and FC_n becomes immiscible if the length is comparable or greater than the tail length (210). These observations support our modeled PFOB-NEP interface since the PFOB chain length (FC_8) is far shorter than either the palmitoyl (C16) or oleoyl (C18) lipid tails of POPC. Finally, our simulation of melittin peptide loaded onto PFOB-NEP interface corroborates the presence of this intercalation, in that PFOB intercalation is necessary for the tryptophan fluorescence quenching to occur by direct collision with bromine atoms (207).

3.5 Conclusions

Despite active research to develop PFOB-NEPs as platforms for carrying therapeutic agents, their atomistic structural details are yet to be determined, and limited knowledge hinders the rational design of the NEPs for optimal efficiency. This study is the first to report the structural details of the PFOB-NEP interface at an atomistic level. The reported interface structure is corroborated by providing a structural explanation for Trp quenching upon the melittin binding on the PFOB-NEP interface. More importantly this work opens new possibilities to study; in particular, the influence of different lipid compositions on the structure of the PFOB-NEP interface as well as cargo binding to the interface. Finally, the atomistic structural details of PFOB-NEP interface in the absence (pure PFOB-NEP interface) or presence of cargo (melittin peptides in this report) can be used as reference structures to develop coarse-grained models of the PFOB-NEP system. Simulation of the systems at a coarse-grained level will enable us to study behaviors on a much larger scale, such as the hypothesized lipid complex formation as well as cargo diffusion through the complex, which are under extensive study in our group.

Acknowledgments

Chapter 4

Interactions of antimicrobial peptides with perfluorocarbon nanoemulsion particles: a molecular dynamics study

4.1 Introduction

Nanoemulsion particles (NEPs) with perfluorocarbon (PFC) cores have shown great potential in delivering a wide range of therapeutic molecules to target cells.(163; 211; 212; 213) PFCs are strongly hydrophobic and form nanoscale emulsions when mixed with water under strong shear force.(214) Biomedical NEPs are often formed with phospholipid surfactants that form monolayers enclosing the PFC droplets to stabilize the particles. PFCs are well known for their biological compatibility and clinical safety (215), with years of demonstrated success as blood substitutes and in other applications.(15; 203)

Recent efforts have focused on the use of PFC NEPs as platforms to specifically deliver melittin, an antimicrobial peptide (AMP), to cancer cells.(35; 11) AMPs have shown promise as anticancer chemotherapeutics if tumor cell specific delivery is enabled.(35; 11; 216; 217) Soman et al. demonstrated that the melittin AMP could be stably bound to PFC NEPs without disruption of NEP morphology nor destabilization of the PFC emulsion. Furthermore, they showed that NEP-bound melittin

retains its biological activity: it can lyse liposomes and induce apoptosis *in vitro* and, more importantly, significantly reduce tumor size in *in vivo* mouse studies.(35; 11) Employing PFC NEPs has resolved many of the difficulties that previously prevented clinical applications of AMPs such as melittin. First, premature melittin degradation is prevented by limited protease access to peptides associated with the emulsifying phospholipid monolayer.(11) Second, the non-specific cytolytic activity can be directed to tumor cells by targeting the NEPs with tumor cell specific ligands on their surface.(11)

The current work is based on the interface structure of perfluorooctylbromide (PFOB) based NEP (PFOB-NEP) determined by previous simulations.(218) This work has focused on understanding differential interaction of melittin, a model cargo peptide delivered by PFC NEPs, with phospholipids on the surface of PFOB-NEPs versus a control bilayer. From the current simulations we aim to understand the structural bases for experimentally observed phenomena such as melittin tryptophan quenching upon its binding to PFOB-NEPs and the ability of PFOB-NEPs to remain intact even after binding of critical concentrations of membrane-disrupting melittin peptides.(35) Finally, structural comparison of melittin bound to the phospholipid monolayer of a PFOB-NEP versus a control bilayer will suggest important structural motifs that can affect the design of cargo for optimal binding to and delivery from PFOB-NEPs.
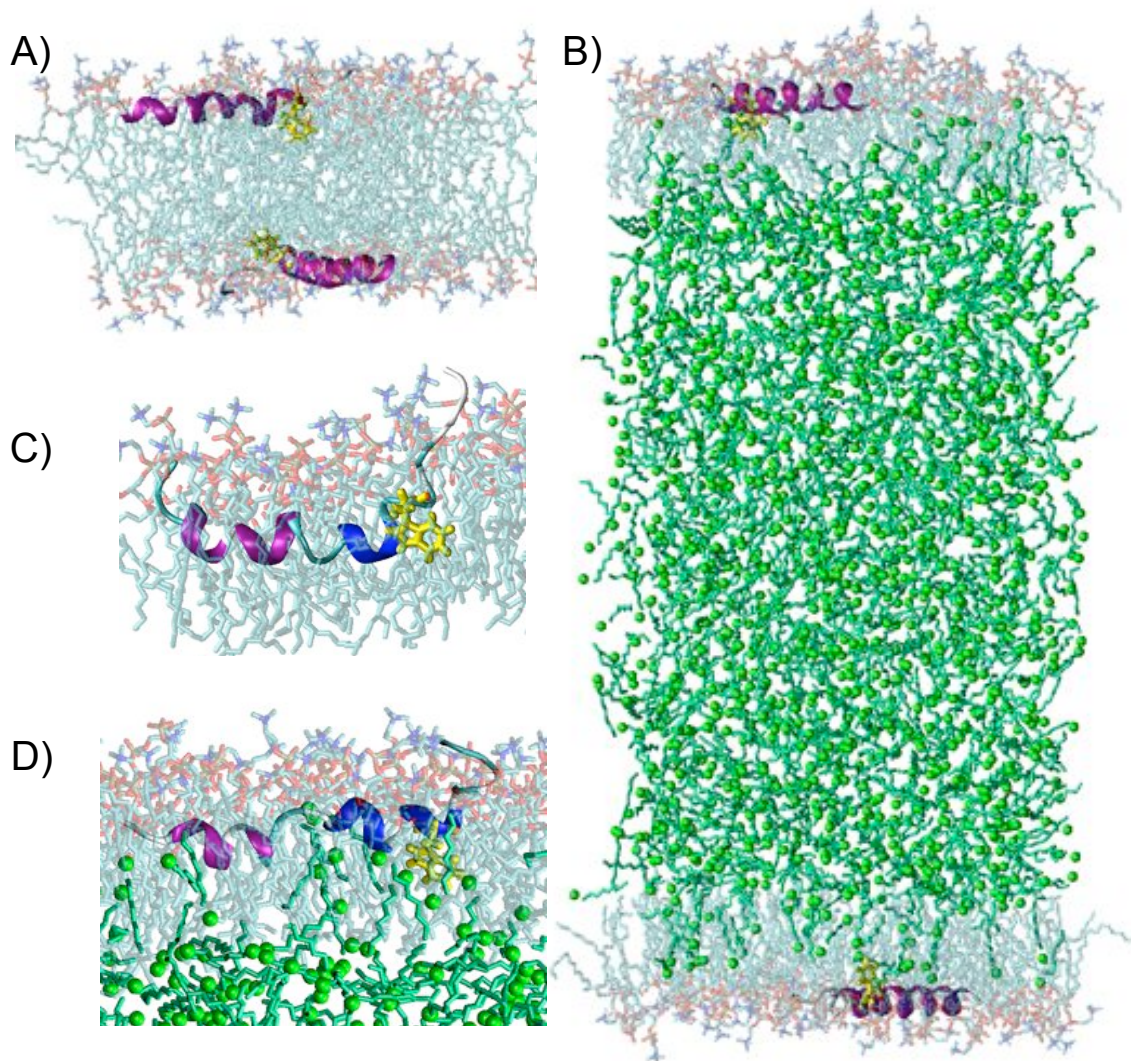
Figure 4.1: Structures of melittin bound to membranes. Initial structure of the Control (A) and the PFOB-NEP (B). Melittin in the top monolayer of the Control(C) and of the PFOB-NEP (D) at approximately 300 ns. Lipids are shown in cyan for carbon, blue for nitrogen, gold for phosphorus, red for oxygen atoms. PFOB is shown in green sticks with an explicit bromine atom depicted as a green ball. The peptides are shown in ribbon style with an explicit tryptophan side chain in yellow. Each residue is colored based on their secondary structure: α-helix in magenta, 3-10 helix in blue, random coil in white, and turns in cyan.

4.2 Methods

4.2.1 Simulations

Initial structures

Melittin was studied in two model systems (see Fig. 4.1): a planar model of a per-fluorooctylbromide (PFOB) NEP interface and a planar POPC bilayer. The initial planar PFOB-NEP interface model in the absence of melittin was prepared as described in previous work (218) with 1310 PFOB molecules sandwiched between two POPC monolayers comprising 64 lipids each. The entire system was surrounded by 11678 water molecules. The initial planar POPC bilayer comprised 128 POPC lipids and 7714 water molecules.

Melittin placement was assisted by a model of bilayer-bound melittin provided by the Hristova and White groups.(192) A single melittin peptide was inserted into each POPC monolayer to the mean depth of the glycerol groups (see Fig. 4.1) as suggested by experimental results.(219; 192) The peptide was inserted so that its non-polar residues faced the hydrophobic interior while its polar residues faced the NEP-water interface. POPC lipids that significantly overlapped with the inserted melittin peptides were deleted, leaving 55 POPC lipids remaining in each monolayer of PFOB-NEP. No PFOB molecules had direct contact with the inserted melittin peptides and hence none of them were deleted. 18,959 water molecules were added to solvate the NEP interface and 10 randomly chosen water molecules were replaced by chloride ions to neutralize 5+ formal charge of melittin. The hydration level of the system was over 90 water per lipid, ensuring complete solvation. The dimensions of the system were 6.0 nm x 6.9 nm x 24.8 nm along the x, y and z directions. Two replica simulations were run for 300 ns respectively. The simulated system was named "PFOB-NEP".

To prepare a control system (named "Control"), the inital planar POPC bilayer was duplicated along the x and y direction so that the new bilayer contained large number of POPC lipids per inserted peptide. The lipids that significantly overlapped with the inserted melittin peptides were deleted. Then the lipids at the boundary of the

bilayer were deleted so that the ratio of lipid:melittin ratio ∼ 100:1 was satisfied in each monolayer without excessive lipids to enhance computing efficiency. 9,984 water molecules were added to solvate POPC bilayer simulation and to neutralize the +5 formal charge of each melittin peptide, ten randomly chosen water molecules were replaced by chloride ions. The hydration level of 90 water per lipid was achieved. The dimensions of the system were 8.3 nm x 8.7 nm x 12.0 nm along the x, y and z directions. Three replica simulations were run for 300 ns respectively.

Force field parameters

PFOB was modeled with the force field parameters previously developed by Lee et al.(218) POPC was modeled with the united atom force field parameters optimized by Berger et al. (76) and Chiu et al. (193) Water was modeled with the simple point charge SPC model.(194) The melittin peptides used in these simulations were modeled with the OPLS-AA force field.(195) Mixing between Berger lipid model and OPLS-AA protein force field was performed using the half-epsilon pairlist approach discussed in previous reports.(218; 82)

Simulation parameters

Molecular dynamics simulations and analyses of the trajectory were performed with GROMACS version 4.0.(92) The starting structures were subjected to previously described equilibration procedures.(78) First, an energy minimization was performed using a steepest descent method and the system was then gradually heated from 50 K to 303 K through a series of short molecular dynamics (MD) simulations. After the system reached the production temperature of 303 K, the MD simulation was continued for at least 300 ns of production simulation. Cutoffs for LJ interaction and for direct space for electrostatic interactions were set at 1.0 nm. The particle-mesh Ewald method (196) with conducting boundary conditions was used for long-range electrostatic interactions. The simulation was performed in an isobaric-isothermal ensemble (NpT). A Parrinello-Rahman barostat (197) with 2 ps coupling time was used to maintain the system pressure at 1 bar. The pressure coupling type varied depending on the systems: isotropic pressure coupling was used for simulations of bulk

solutions, semiisotropic for simulations of PFOB-NEP interface and POPC bilayer systems, and anisotropic for the simulation of melittin bound membranes. A Nosé-Hoover thermostat (198) with 0.5 ps coupling frequency was applied to each molecule type separately. Hydrogen atoms bonded to heavy atoms were constrained with the LINCS algorithm (199), allowing a 2 fs time step to be used. Initial velocities were randomly assigned from different Maxwell distributions for each simulation.

4.2.2 Analysis

Block averaging

To perform statistical analysis, each trajectory was divided into small blocks with the block size chosen based on the standard error so that each block was independent of one another.(200) The standard error $\varepsilon(f, n)$ in observable f for a block of length n was calculated according to the formula $\varepsilon(f, n) = \sigma/\sqrt{M}$, where n is the block length, σ is mean standard deviation, and M is the number of blocks in the simulation. When the block size is large enough; i.e., much greater than the correlation time of an observable, the standard errors become independent of the block size and the true standard error is obtained. The block size for sub-sampling was determined by the value of n where $\varepsilon(f, n)$ for observable f reached a plateau. When an observable was calculated for each monolayer separately, then the results from each monolayer were combined and the number of independent blocks was doubled.

4.3   Results

4.3.1   Equilibration and sub-sampling

The total membrane area was used to determine the equilibration and the size of statistically independent sub-sample size. Substantial drift was only detected in one POPC "Control" bilayer simulation (figure 7.8). To remove the initial drift, the first 100 ns of trajectory was discarded from all other simulations. The evolution of total membrane area of the remaining 200 ns-long trajectories was used to determine the
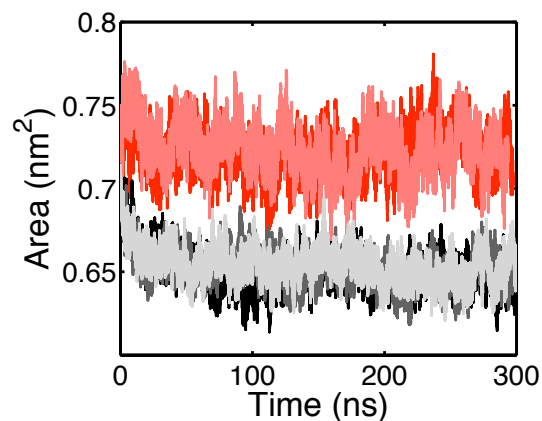
Figure 4.2: Evolution of total membrane area. The evolution of total membrane area of the Control (black, dark gray, and light gray) and the PFOB-NEP (red and light red) are plotted for the trajectories of 300 ns.

independent sub-sample size as introduced in 4.2.2. A block size of ≥ 40 ns resulted in a plateau of standard errors in all five simulations (see Supplementary material). Therefore, a block size of 40 ns was applied, which generated 5 independent sub-samples for each simulation. Sub-samples from each replica simulation was combined to lead in 10 independent sub-samples for PFOB-NEP and 15 for Control. When the observables were computed for each monolayer, then the sub-samples were duplicated to be 20 for PFOB-NEP and 30 for Control.

4.3.2 Melittin conformation

Secondary structures

Many AMPs undergo significant structural transitions when binding to membrane environments,(219; 220; 32) indicating the important role of the membrane environment in their structural properties. Therefore, it is useful to assess whether differences between the monolayer environment of the PFOB-NEP and the bilayer environment of POPC Control induce changes in the melittin conformation. Using the DSSP algorithm (221), melittin secondary structures were categorized into four different conformations: random-coil, bend, turn, and helix. The fractions of each conformation adopted were determined for each melittin residue (see Fig. 4.3).

Two residues at both N- and C-termini adopted mostly random-coil conformations in both the Control and PFOB-NEP. Two major helical segments (residue 6-LKVLTTGL-13 and residue 17-ISWIKRK-23) were detected in both systems. The former was named N-terminal and the latter C-terminal helical segment.
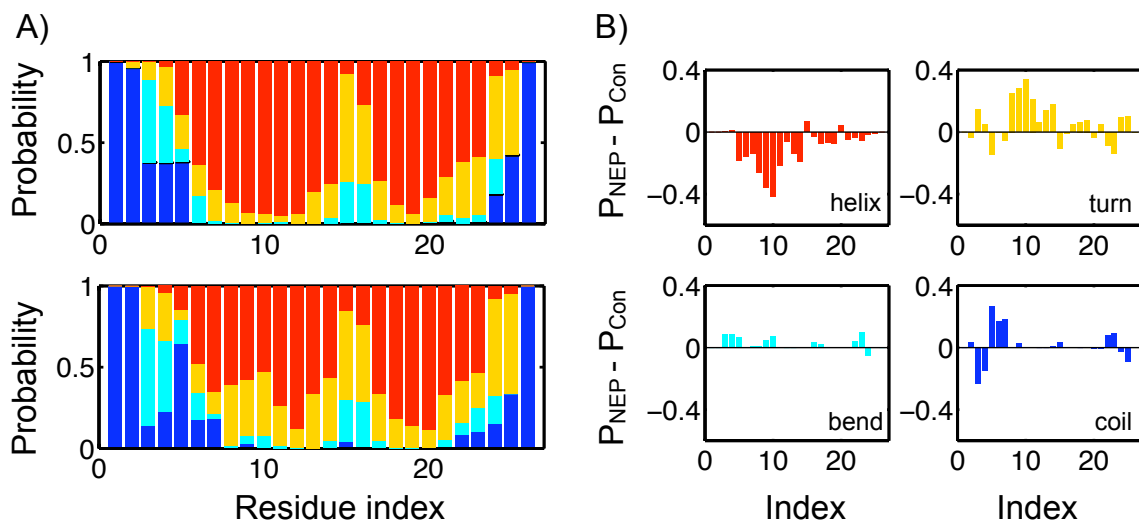
Figure 4.3: The secondary structure content of each residue. The secondary structures were categorized into four different conformations: random-coil (blue), bend (cyan), turn (yellow), and helix (red). A) The top panel shows the secondary structure contents of the Control, the bottom shows those of the PFOB-NEP. B) The difference in the content for each conformation between the Control and PFOB-NEP is plotted.

The melittin bound to the monolayer of PFOB-NEP exhibited differences in the structure from the melittin bound to the POPC bilayer. The overall peptide helical content was smaller in the PFOB-NEP, for which it was replaced by the less structured turn conformation. Reduction in helical content was more pronounced in the N-terminal helical segment. At the kink (14-PAL-16) between the two helical segments, the internal hydrogen bonds were lost and turn conformations were replaced by bend conformations.

4.3.3 Peptide-lipid interaction

Solvent accessible surface area

Solvent accessible surface area (SASA) was estimated for the peptide and lipids separately (see Fig. 4.4), and the SASA was divided into either hydrophobic ($|q| \leq 0.25$) or hydrophilic ($|q| > 0.25$) surface area, where q represents the charge of each atom.

Hydrophobic SASAs of the peptide in the PFOB-NEP were greater than those of the peptide in the Control POPC bilayer while hydrophilic surface area was slightly decreased. However, the differences were not statistically significant at a 95 % confidence level. Increased exposure of hydrophilic surface accompanied by decreased exposure of hydrophobic surface of lipids agreed with our previous report (218) while additional perturbation by the associated melittin was not detected.
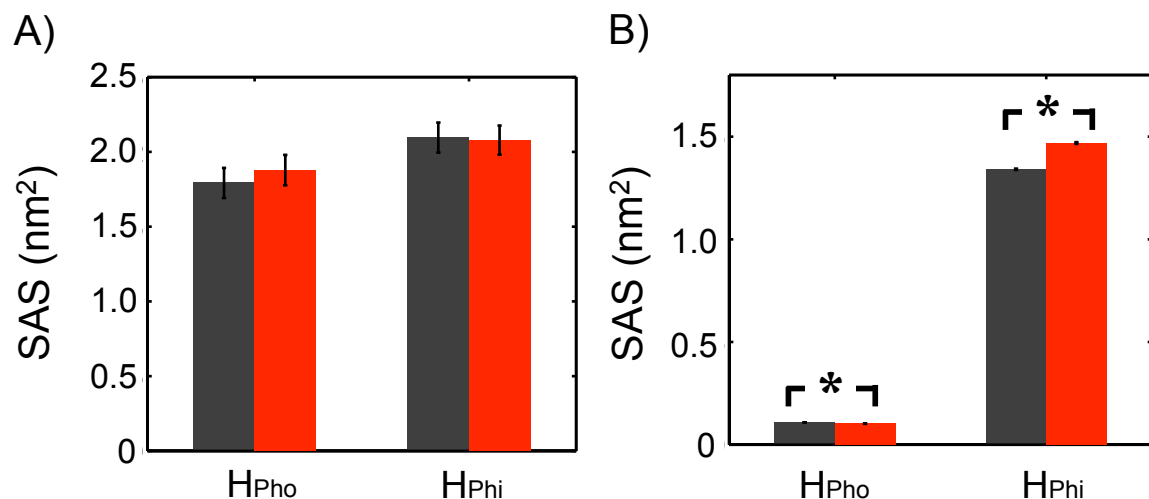
Figure 4.4: Solvent accessible surface area of the melittin peptide (A) and a lipid molecule (B). Dark gray bars are those of the Control and red bars of the PFOB-NEP. "Hphi" represents hydrophilic surface and "Hpho" hydrophobic surface. The ∗ symbol indicates the statistical significance with a p-value of 0.05.

Density overlap between melittin and the phospholipid monolayer

Number density profiles of melittin and lipid groups in a monolayer were determined over the replica simulations and are illustrated in Figure 4.5. The density profile

of the monolayer was centered at zero and the density profiles of other parts of lipids and peptide were placed with respect to that of the monolayer. As reported
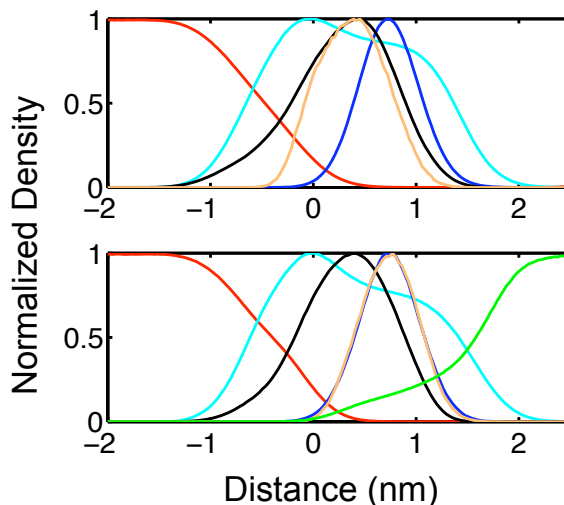
Figure 4.5: Number density profiles of the phospholipid monolayer and embedded melittin peptide for the Control (top) and PFOB-NEP (bottom) systems. The density of the monolayer is shown in cyan and the density of methylene group in blue. The density of the entire melittin peptide is shown in black and that of tryptophan side chain (W19) is shown in orange. The density of water is shown in red and PFOB (only in the bottom panel) in green.

previously (218), the monolayer on the surface of the PFOB-NEP was thicker due to more extended head group and tail conformations. The monolayer density profiles were almost identical between the Control and the PFOB-NEP, which was a striking difference from the melittin-free system where the monolayer density profile of PFOB-NEP was substantially wider, implying a thicker monolayer, than the Control (218). The density profile of melittin peptide was narrower in the PFOB-NEP, and the residual density of the peptide extended farther out of the hydrophilic surface of monolayer in the Control. The density of tryptophan was detected near the methylene group of oleoyl chain, which was deeper in the PFOB-NEP.

Peptide penetration

To further understand the differential melittin interaction with monolayers, we determined the relative positions of Cα carbons with respect to the mean depth of glycerol moiety of each monolayer (see Fig. 4.6).

Melittin was more deepley buried throughout the peptide in the Control than in the PFOB-NEP. However, the deeper penetration was more substantial for the residues in the N-terminal helical segment. A Student's t test revealed that most of the differences between the two systems are statistically significant.
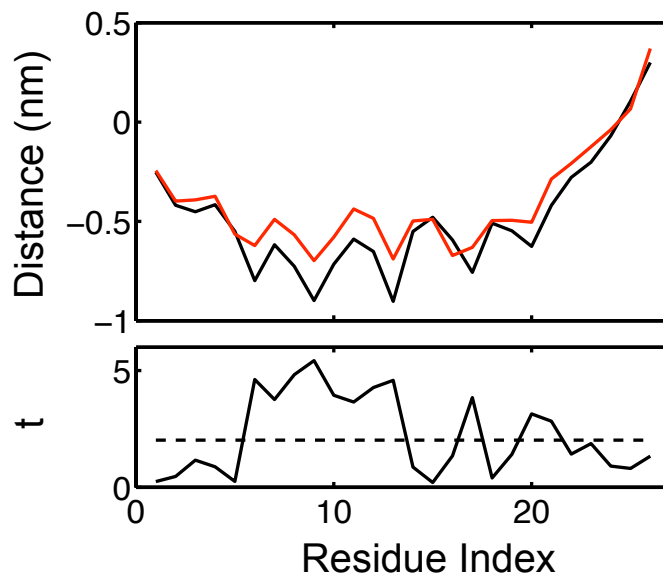
Figure 4.6: Penetration of melittin into the phospholipid monolayer. The top panel shows the relative mean positions of C$_\alpha$ carbons of the Control (black) and the PFOB-NEP (red) with respect to the position of glycerol groups of each monolayer. The bottom panel shows the Student t-values for differences in C$_\alpha$s between the Control and PFOB-NEP systems. The dashed black line indicates the t-value ($n = 48$) for a significant difference with a p-value of 0.05. The n number is doubled since two data sets (one for each monolayer) were obtained from each block.

Close apposition of the bromine atoms near the tryptophan side chain

The radial distribution of the bromine atom of PFOB molecules around the tryptophan (W19) side chain was determined for and averaged over each independent

sub-samples. The result is plotted in Figure 4.7. Finite bromine density appeared as close as 0.3 nm to the tryptophan sidechain, indicating direct contact between the two parties. This direct contact is important for explaining the experimental quenching observed experimentally (176; 222) and in our previous atomic-scale simulations (218).
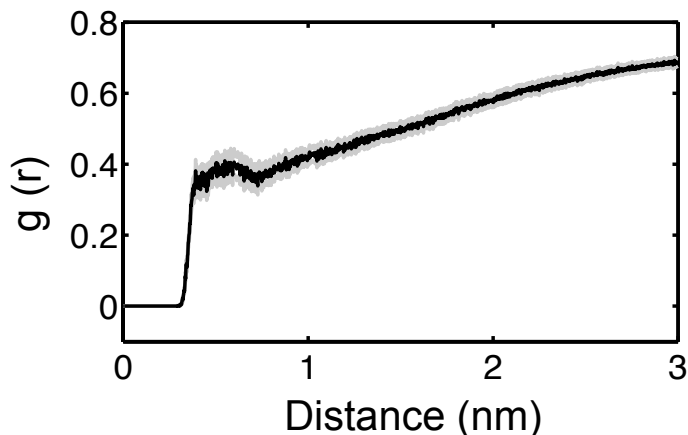
Figure 4.7: Close approach of bromine atoms to tryptophan side chain. The plot shows the radial distribution function of PFOB bromine atom around the tryptophan (W19) side chain. The black solid line shows the mean of the distribution and the gray solid lines show the one standard error deviation of the distribution.

Peptide-lipid contact map

To further clarify the contribution of lipid moieties in their interaction with the embedded melittin peptide, a contact map (223) was constructed to enumerate interactions between the lipid moieties and each residue of melittin (see Fig. 4.8). Interaction of a lipid moiety with a certain residue of melittin was defined by a distance cutoff of 0.6 nm. The distance measurement was made for all possible pairs of the atoms in a defined lipid moiety and a residue. If the distance of any pairs was shorter than the cutoff, the number of contact was incremented by one for that specific match. The contact numbers were averaged over two peptides in each monolayer and over the simulations. Different lipid moieties are defined in the Figure 4.8A.

Figure 4.8B and C shows melittin interactions with the nearby lipids. The patterns of peptide-lipid contact were very similar between the two systems. Charged residues (amino terminus, Lys7, Arg22, Lys23, Arg24) showed more frequent interactions with

polar lipid moieties including phosphate group and ester group of sn-2 chain (oleoyl acid). Among them, two arginine residues showed the most extensive interactions. As expected in their helical conformation, the residues on the hydrophilic side interacted with head group moieties and the residues on the hydrophobic side of the helix interacted with the moieties of lipid tails.

The melittin peptide embedded in the monolayer of the Control had more frequent contact with lipids moieties both hydrophobic and hydrophilic. The interactions of the peptide with the moieties of lipid tails near the N-terminus were declined in the PFOB-NEP. The interactions near the C-terminus were also observed in the PFOB-NEP, which was most substantial at the Arg22.
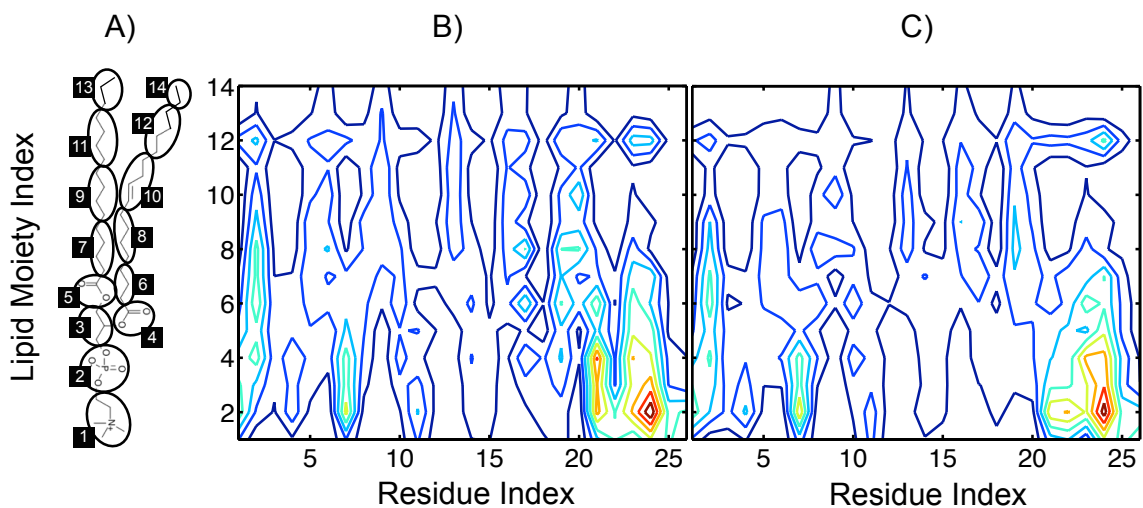
Figure 4.8: Contact map between the every residue of the peptide and the moieties of lipid. A) The division of a POPC lipid into small moieties is present. The contacts of melittin with the Control (B) and with the PFOB-NEP (C) are shown by contour maps. Smaller indices indicate lipid moieties closer to the hydrophilic surface while greater indices indicate moieties that are deeper in the hydrophobic core. The mean contact number ranges from 5 (dark blue) to 40 (dark red).

4.3.4 Membrane structure

Monolayer thickness

To assess the structural changes of the membranes, monolayer thickness was deter-
mined and compared between the PFOB-NEP and Control bilayer systems in the
presence and absence of melittin. Bilayer thickness is typically determined by the
distance between the phospha   1); however, this defi-
nition is not applicable to mo   risons among the sim-
ulated systems used a definiti   mined from the mean
distance between the phosphat   yl group of the palmi-
toyl chain. Figure 4.9 shows t   ificantly thicker in the
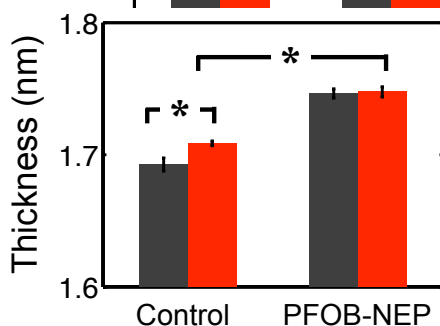
Figure 4.9: Comparison of monolayer thickness between the Control and the PFOB-
NEP. The ∗ symbol indicates the statistical significance with a *p*-value of 0.05.

Control when the membrane contained melittin while the thickness of the monolayer
of the PFOB-NEPs was not changed due to the presence of melittin. Despite its
increase in thickness, the melittin-bound monolayer of the Control was thinner than
that of PFOB-NEP. The increased thickness of the control monolayer in the presence
of melittin peptide was also observed in the density profile shown in Figure 4.5.

Lipid tail ordering

Lipid tail order parameters provide an indication of the mean conformation of lipids
in a membrane. On average, lipid order parameters increased upon the binding of
melittin to the membrane (see Fig. 4.10). To provide a more detailed view of the
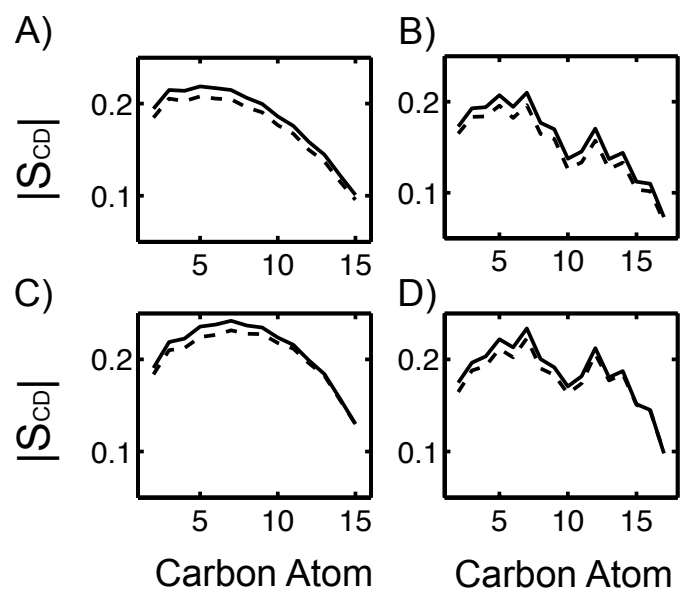
Figure 4.10: Global lipid order parameters. Lipid order parameters averaged over all lipids in each monolayer. The deuterium order parameters of the palmitoyl chain (A) and the oleoyl chain (B) of the Control and the PFOB-NEP (C, D in the same sequence) were averaged over all the lipids in each monolayer. Data from systems containing melittin peptides are shown in solid black lines; the dashed black lines are the order parameters of the same membranes but in the absence of melittin.

influence of melittin on the membrane structure, the order parameters were computed as a function of distance from the embedded melittin. The membrane was subdivided into 4 shells with the thickness of 0.9 nm around the peptide. Each lipid was assigned to one of the 4 shells depending on its distance from the melittin in the xy plane. Lipids in the innermost shell were assigned first. If the separation between the geometric center of a lipid and the geometric center of any melittin residue was closer than 0.9 nm, the lipid was assigned to the first shell. Next, the lipids for the second shell were selected if the distance from the geometric center of a lipid to the geometric center of any lipid in the first shell was shorter than the 0.9 nm cutoff. Lipids that belonged to the third and fourth shell were assigned in the same manner. This assignment and the calculation of order parameters were repeated for every snapshot and order parameters were averaged for each shell over the course of simulation.

Figure 4.11 shows the changes in the lipid order parameters due to the presence of melittin. Melittin decreased tail order for lipids closer than 0.9 nm near the tail ends but increased tail order for all bonds of all lipids beyond that distance. This ordering effect by melittin was weaker and decayed more quickly in the PFOB-NEP than in the Control bilayer. As shown in Fig. 4.11, the conformation of lipids in the fourth shell of the PFOB-NEP:melittin system are similar to lipids in the melittin-free monolayers of the PFOB-NEP system.
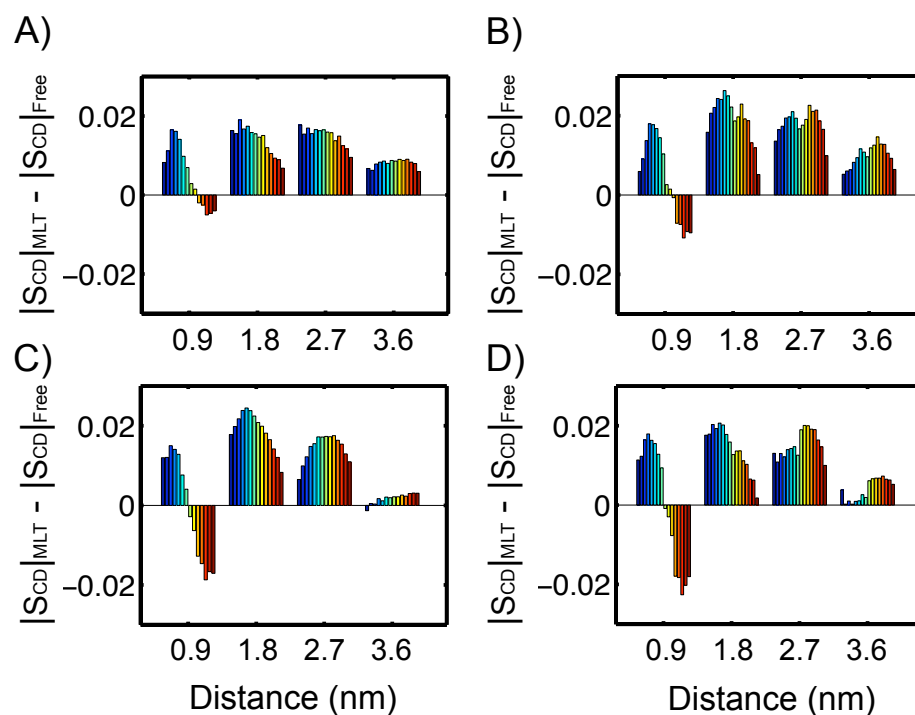
Figure 4.11: Local lipid order parameters. Differences in the order parameters in the presence and in the absence of melittin as a function of lipid separation from the melittin. The differences of the palmitoyl chain (A) and the oleoyl chain (B) of the Control and the PFOB-NEP (C and D in the same sequence) are plotted separately. The narrow bars show the difference in the order parameter of each carbon bond. The palmitoyl chain has 14 carbon bonds and the oleoyl chain has 16 bonds. The bonds near the polar head group are colored in blue and those near the hydrophobic tail end in dark red.

4.4 Discussion

4.4.1 Structural determinants of melittin binding to PFOB-NEPs

Secondary structure

As illustrated in Figure 4.3, the helical content for the peptide in the Control bilayer agreed well with the experimentally measured helical content of about 19 to 20 residues.(224; 225) Additionally, the smaller helical content in the PFOB-NEP agrees with the decreased ellipticity at 220 nm and 208 nm of melittin peptides when bound to PFOB-NEPs as compared to the melittin bound to liposomes.(35) The N-terminal segment showed more pronounced reduction in the helical content, which may have resulted from the attenuated penetration of the segment into the monolayer (see Fig. 4.6). Since melittin peptides are known to be unstructured in solution and form secondary structure only upon binding to membranes (225; 226), it is possible that the decreased helical content resulted from competition of internal hydrogen bonds with the surrounding water molecules.(227)

Peptide-lipid interactions

The contact maps of peptide residues and lipid moieties showed that the two arginine residues (R22 and R24) exhibited the strongest interaction with the phosphate and ester groups (Fig. 4.8). This result is in accordance with the experimental observation that these charged C-terminal residues are important for the binding to both neutral and negatively charged membranes,(228) presumably due to salt bridges between the arginine guanidinium and lipid phosphate groups.(229) These particular interactions were diminished in the PFOB-NEP system, indicating that this mode of interaction of melittin with the PFOB-NEP monolayer may be weaker than in the Control bilayer.

PFOB intercalation affects cargo loading

PFOB is the perfluorocarbon that forms the core of PFOB-NEPs. Our previous work (218) showed that PFOB could intercalate into the emulsifying lipid monolayers due to their linear shape and lengths that are relatively shorter than the monolayer lipid tails. PFOB intercalation reduces the free volume in the hydrophobic tail region of the monolayer and thus provides a driving force for preventing insertion of melittin into the PFOB monolayer to the same depth as it is found in bilayer environments. This attenuated penetration results in reduction in melittin secondary structure and subsequent changes in the interactions with nearby lipids. These observations suggest that the interaction of the core forming perfluorocarbon with the emulsifying monolayer affects the interaction of cargo on the surface of PFC-NEPs. Reduced free volume could be more detrimental for the loading of cargo molecules that require deeper penetration due to elevated hydrophobicity. For optimal cargo loading for such hydrophobic molecules, modulation of the mixing between the emulsifying monolayer and the core forming perfluorocarbon will be required.

4.4.2 Membrane structural changes

Our simulations showed that melittin thickened the monolayers of the Control system bilayer, This observation was determined by the mean distance between the phosphate and terminal methyl group (Fig. 4.9) and by the number density profiles (Fig. 4.5). Consistent with this thickening, we observed changes in lipid order parameters (Fig. 4.10. The disordering of lipids adjacent to the melittin was observed in accordance with previous experiments (Fig. 4.11).(230; 231; 232) However, lipids beyond the first shell, directly surrounding the peptide, were influenced to be more ordered. Higher order indicates more extended lipid tail conformations and, consequently, a thicker membrane.

While local lipid disordering agrees with experimental results, our observation of overall monolayer thickening is in contrast to the experimental observations made at melittin concentrations below the critical concentration at which melittin caused membrane thinning.(230; 231; 232) A possible reason for the deviation is the presence of overly favorable interactions between the peptide and lipids. Artificially strong

interactions may have caused tighter interactions, increased order, and membrane thickening. Such overly favorable protein and lipid interactions were detected with the combination of the united gromos protein model and the Berger lipid model.(195; 82) To reduce the impact of this potential artifact, we carefully chose the combination of the all-atom OPLS force field for melittin and the Berger lipid model, which did not inherit such problem based on a previous report by Tieleman et al.(77) Our data, however, indicated that we might still have some degree of this artificial effect in our simulations. Because of these limitations, we have confined our interpretation of the data to comparative studies of the differences between the Control and the PFOB-NEP environmental influence on melittin conformations and melittin interactions with lipid bilayers/monolayers.

4.4.3 Mechanism of quenching for melittin tryptophan upon binding to PFOB-NEPs

Experimental measurements place the depth of the melittin tryptophan residue (W19) 1.06 nm away from the center of a di-oleoyl-phosphatidylcholine (DOPC) bilayer.(233) As illustrated in Figure 4.5, our simulations also placed tryptophan density approximately 1 nm away from the center of the Control bilayer, thus showing good agreement with these experimental results. Previously, based on the observation that melittin tryptophan fluorescence could be quenched by water-soluble molecules, it had been argued that the melittin tryptophan should be located in the water-accessible region near the first carbon of the lipid tails.(225) This observation was in apparent contradiction with the placement of the melittin tryptophan 1.06 nm away from the center of a DOPC bilayer.(233) As shown in Figure 4.5, our data reconcile these two apparently opposing experimental results by showing that water molecules could penetrate to the depth of tryptophan and thus suggesting that water-soluble quenchers should also be able to access the deeply buried tryptophan side chain in this region of the bilayer.

The validity of our simulations is also further supported by the location of the melittin tryptophan residue in the PFOB-NEP interface system in that tryptophan side chain had direct contacts with the bromine atom of PFOBs. The direct contact between the tryptophan side chain and bromine atoms provides the molecular mechanism for

tryptophan fluorescence quenching upon the peptide binding to the surface of PFOB-NEPs (see Fig. 4.7).(218; 35)

4.4.4 Understanding PFOB-NEP stability in the presence of high melittin concentrations

Melittin does not disrupt lipid monolayer structure on the surface of PFOB-NEP, even at very high melittin concentrations (lipid:melittin ratios of up to 40:1) far above the critical concentration (lipid:melittin ratio of 62:1) for melittin transmembrane configuration and pore formation in POPC bilayers. (35; 234; 34) Our simulations provide some insight into potential reasons why this disruption does not occur. It has been shown experimentally that helical conformation and amphipathicity are important for the lytic activity of melittin toward neutral membranes, (235) such as the lipids obtained from the egg lecithin used to prepare PFOB-NEPs.(236) Our simulations revealed reduced helicity and suggested potentially lower pore-forming and lytic capabilities. Another important feature for pore formation and membrane disruption is the reorientation of melittin to a transmembrane configuration.(34) In the monolayer of the PFOB-NEP, this conversion to a transmembrane configuration is extremely unlikely due to necessary interaction of polar and charged melittin residues with the strongly hydrophobic perfluorocarbon core of the PFOB-NEP.

4.5 Conclusions

Our simulations revealed the molecular details of the melittin bound at high mole fractions either to a bilayer or a PFOB-NEP monolayer. A few structural details including helical contents and direct contact between tryptophan (W19) side chains and bromine atoms corresponded experimental observations (35) and hence supported our simulations.

Melittin exhibited differences in its conformation and mode of interactions with the surrounding lipids when bound to a PFOB-NEP monolayer. First, the helical content of melittin was reduced, 2) it adopted more linear overall conformation, and 3) it

exhibited less frequent direct contacts with the lipids especially by the charged C-terminal residues.

From these structural changes, functional consequences were inferred. First these changes suggested a weaker binding affinity of the melittin toward the PFOB-NEP monolayer. Reduced helicity destabilizes the amphipathic peptide at the membrane interface.(237) The salt bridge between the charged residues at the C-terminus with the lipid head groups are important for its binding to a membrane.(228) Second the changes suggested the attenuated lytic activity of melittin on the surface of PFOB-NEP because helical conformation(235) was found to be important for the hemolytic activity of the peptide.

Our simulations suggested the attenuated penetration of melittin into the hydrophobic interior of the monolayer of PFOB-NEP as a major molecular determinant for such alterations and also suggested that preoccupied free volume by the intercalated PFOB molecules, otherwise melittin could have been as deeply buried as in the control bilayer, be the cause of the shallower penetration. The results implied that the interaction of the core forming molecules could affect the binding of cargo molecules to this emulsifying monolayer.

Our simulations demonstrate that the interaction of core forming peruorocarbon molecules with the emulsifying phospholipids monolayer can directly affect the mode of cargo binding to the perfluorocarbon-based nanoemulsion particles. Hence, systematic analysis may help to elucidate the optimal combinations of PFC molecules and enclosing phospholipids for the most stable and efficient cargo loading to the peruorocarbon-based nanoemulsion particles.

Chapter 5

Membrane fusion between the monolayer of PFC-NEP and the outer monolayer of liposome

5.1 Introduction

Nanoscale particles, of $200 \sim 300$ nm in diameter, have been developed to sequester loaded cargo until a specific target, recognized by the targeting surface ligands, is reached. The delivery of therapeutic agents including drugs, imaging agents, and macromolecules such as nucleic acids and proteins using nanoscale particles has advantages over conventional small molecule treatment. Delivery using nanoscale particles prevents premature degradation of the therapeutic agents, concentrates the agents at a specific target tissue or cell type, and aids agents in crossing through biological barriers such as epithelium, endothelium, and plasma membrane.(36) Nanoparticle design must be precisely tailored to deliver each particular agent to its appropriate destination. To achieve efficient delivery to subcellular organelles, we must understand the molecular mechanisms of how nanoparticles interact with plasma membranes.

Phagocytosis and endocytosis are the most common internalization mechanisms for nanoparticles such as liposomes and polymer-based nanoparticles.(36) However, these internalization mechanisms involve lysosomal degradation that attenuates therapeutic efficiency and as such are not suited for the delivery of therapeutic biomolecules. Alternative strategies have been developed where cargo molecules are directly inserted into the cytoplasmic space through transient pores in the plasma membrane. Direct

insertion methods include the conjugation of therapeutic cargo to cell-penetrating peptides(37; 38), electroporation(39; 40), and therapeutic ultrasound with microbubbles.(41; 42; 43) However, all of these methods have the potential to cause cell damage by disrupting the plasma membrane.(38; 40; 44; 45; 46)

Perfluorocarbon-based nanoemulsion particles (PFC-NEP) that are stabilized by an emulsifying phospholipid monolayer provide another delivery mechanism. This so called "contact-facilitated" delivery mechanism involves neither lysosomal pathways nor substantial perturbations in membrane such as pore formation. The delivery mechanism is hypothesized to start with the formation of a hemifusion complex between the monolayer of PFC-NEP and the outer monolayer of target cell plasma membrane. Cargo molecules then diffuse to the plasma membrane through the hemifusion complex and are finally internalized by lipid raft mediated endocytosis.(238; 239; 47) This mechanism would particularly useful for the delivery of biomolecules that are highly susceptible to enzymatic reactions. However, the molecular details of this mechanism are as yet undetermined due to experimental difficulties of structure determination of small, fluid, and highly heterogeneous systems.

Molecular dynamics simulations have been widely used to determine membrane structures at both an atomistic(69; 78; 79; 80; 81; 82; 55) and coarse-grained level.(85; 86; 90; 87) Atomistic simulations are useful for collecting accurate structural details but often too costly for examining biologically important membrane behavior such as self-assembly of lipids into bilayers or vesicles, bilayer phase changes, domain formation, pore formation, and membrane fusion. Therefore, coarse-grained models have been extensively used to simulate these mesoscopic phenomena. Theoretically proposed membrane fusion mechanisms involving a hemifusion stalk(240; 241) were validated by the appearance of proposed intermediate structures in coarse-grained simulations.(71; 56) Furthermore, simulations have identified important structural motifs, such as splayed lipids in inducing membrane fusion, which could not be predicted from the theories based on continuum models.(242; 55)

In this research, we have focused on the initial step of the contact-facilitated delivery mechanism,(47) where two monolayers form a hemifusion complex, which resembles the hemifusion stalk.(50; 240) We have used coarse-grained molecular dynamics
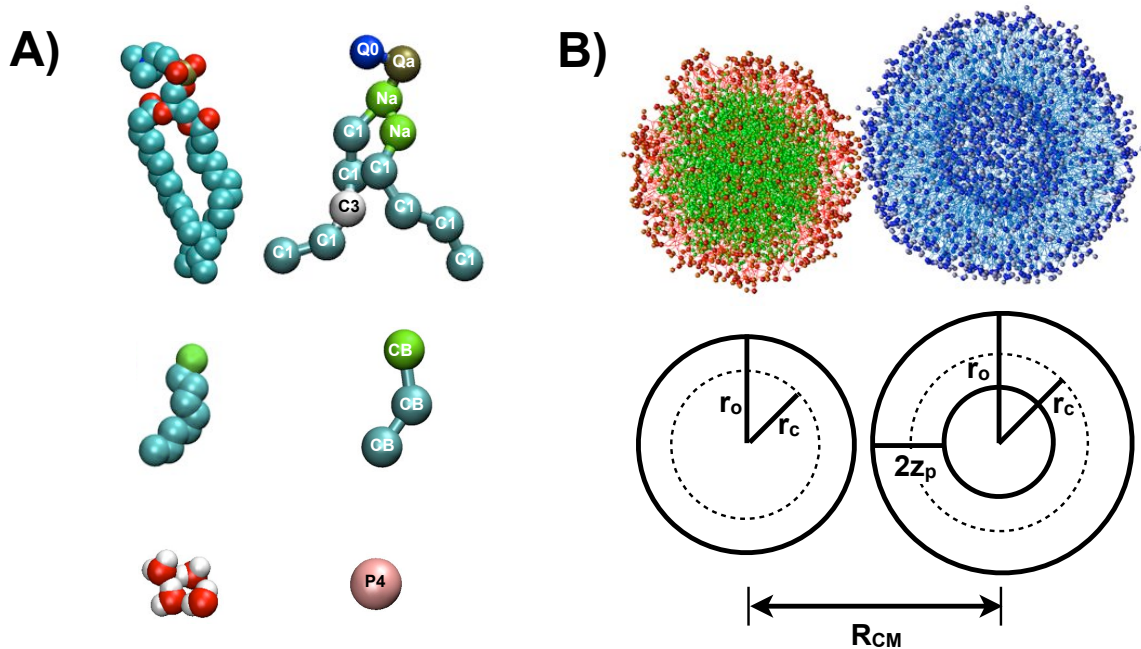
Figure 5.1: System configuration and constituting molecules. The structure of a linked NEP and liposome and the structures of molecules contained in the system. A) The structures of phospholipid (POPC), perfluoroocytlbromide (PFOB) and water molecules, from top to bottom, presented at an atomistic (left) and coarse-grained (right) level. The type is shown for each coarse-grained site. The CB type was specifically developed to model PFOB. B) The initial structure of a fusion simulation, with a PFOB-NEP and a liposome held in close contact through artificial links. PFOB is shown in green and enclosing phospholipids are shown in red. The lipids constituting the liposome are shown in blue. The geometry of the two particles is defined in the bottom panel. R_{CM} is the distance between the center of mass of each particle. r_o is the distance of phosphate group from the center of mass of each particle and r_c is the distance of lipid termini. $2z_p$ is the distance between phosphate group of the outer and inner monolayer.

simulations to directly test hemifusion complex formation between a PFC based nanoemulsion particle and a liposome that models a target cell. We also have tested the dependence of nanoparticle-liposome fusion on particle size and lipid composition in order to identify important structural (physico-chemical) features of the particles required for optimization of fusion.

5.2   Methods

5.2.1   Development of a coarse-grained PFOB model

To simplify a model system, the MARTINI force field usually maps four atoms into a coarse-grained bead, or interaction site. The MARTINI force field contains four main types of interaction site: polar (P), non-polar (N), apolar (C), and charged (Q). The main types are subdivided into 18 different subtypes based on their hydrogen bonding capability and level of polarity. Within the 18 different subtypes, 10 different levels of van der Waals interaction potentials are defined: super attractive, attractive, almost attractive, semi attractive, intermediate, almost intermediate, semi repulsive, almost repulsive, repulsive, and super repulsive.(88) These potentials were obtained by ranging the energy parameter ϵ from 5.6 $\sim$ 2.0 kJ/mol with a constant size parameter σ of 0.47 nm. The only exception was the super repulsive potential where the size parameter was increased ($\sigma = 0.62$ nm) to preserve the strongly unfavorable interaction between charged (Q) and apolar (C) interaction sites. Despite its simplicity, the MARTINI force field has been widely and successfully used to simulate mesoscopic phenomena including membrane fusion, pore formation, self-assembly, and domain formation. Further, the MARTINI force field is easy to implement and is transferable for other small molecules. For these reasons, we developed a coarse-grained model of a perfluorocarbon molecule, perfluorooctylbromide (PFOB), in accordance with the MARTINI force field (see Table 5.1).

Intra-molecular interaction parameters   PFOB was modeled by three interaction sites, named as follows: BRC (BrCF$_2$CF$_2$CF$_2$-), CBM (-CF$_2$-CF$_2$-CF$_2$-), and

CBE (-CF$_2$-CF$_2$-CF$_3$) such that the coarse-grained model was a linear 3-particle system, BRC-CBM-CBE. Bond length was determined based on the Lennard-Jones (LJ) size parameter and bending angle was determined following the manner that the CG lipid aliphatic chain was modeled in the MARTINI force field. To accelerate computation, the MARTINI force field normally uses the same mass for all interaction sites and ignores partial charges.(85) However, to preserve the asymmetric nature of PFOB, we used the true mass and partial charges for each site in our force field development and simulations, as discussed in section 5.4.1. These three sites were modeled by the same interaction site type, CB, which was newly developed in this work to preserve the stronger hydrophobic character of perfluorocarbons as compared with hydrocarbons. The initial guess of the LJ parameters ($\sigma = 0.47$ nm and $\epsilon = 3.5$ kJ mol^{-1}) was taken from the polar interaction site type C1 of the MARTINI force field.(88)

The size (σ) and energy (ϵ) parameters were systematically varied starting from the initial guess to reproduce the density and heat of vaporization of liquid PFOB. The final LJ parameters were $\sigma = 0.5$ nm and $\epsilon = 3.5$ kJ mol^{-1}.

Inter-molecular interaction parameters To describe the interaction of PFOB with other molecules such as lipids and water, the LJ parameters between CB and other interaction sites were prepared using the constant size parameter of $\sigma = 0.5$ nm and different energy parameters (ϵ) based on the level of attractiveness between the two sites. The slightly greater than standard σ value imposes less favorable interaction level for all pairs than the corresponding pairs with the apolar (C) site. The super repulsive potential between a charged (Q) and CB was treated as in the MARTINI force field, except using σ of 0.62 nm.

To accelerate computation, the MARTINI force field normally uses the same mass for all interaction sites and ignores partial charges.(85) However, to preserve the asymmetric nature of PFOB, we used the true mass and partial charges for each site in our force field development and simulations as discussed in section 5.4.1.

5.2.2   Simulations

Force field parameters

PFOB was modeled by the new coarse-grained model. Phospholipids: 1-palmitoyl-2-oleolyl-phosphatidylcholine (POPC), and 1-palmitoyl-2-oleoyl-phosphatidylethanol-amine (POPE) and water were modeled by the standard MARTINI force fields.(88) The newest MARTINI force field defines the interaction level between the charged sites (Q) and apolar sites (C) to be super-repulsive, which was repulsive in the previous version. The recent change was made to prevent the penetration of the ion sites (Q) through the bilayers.(88) The modification, however, strongly inhibits membrane fusion protrusion of lipid tails out of the membrane because the interaction between apolar lipid tails and the charged head group sites (the choline and the phosphate group) are super-repulsive.(242) This protrusion of hydrophobic tails out of the membrane surface is a prerequisite for membrane fusion. Hence, the interaction level for the pairs of the charged sites of lipid head group (the choline and phosphate group) and the tails were adjusted from super-repulsive to repulsive to enable the protrusion of hydrophobic tails in the fusion process we are modeling.

Initial structures

To generate a sphericial PFOB-NEP, a number of phospholipids, PFOB, and water molecules were randomly mixed. A water shell of 5 nm in thickness surrounded this mixture in all directions so that the hydrophobic molecules were isolated inside of the simulation box and would not form a lamellar phase with their periodic images. The system sizes and compositions that were successful in forming an intact PFOB-NEP are listed in Table 5.2.2. The mean dimensions of the starting structure were 25.3 nm x 25.3 nm x 25.3 nm along the x, y and z directions.

To generate a liposome, a small patch was taken from a large bilayer and put in a simulation box. Water molecules were then added into the box so that the small bilayer would be solvated in all directions. The lipid bilayer at this state is disk-shaped and called as a bicelle. The composition of each liposome is listed in Table

Table 5.1: Force field parameters for PFOB at a coarse grained level

Bond Stretching Parameters

bond	k_b(kJ mol^{-1} nm^{-2})	r_0(nm)
CB-CB	1250	0.5

Angle Bending Parameters

angle	k_0(kJ mol^{-1} rad^{-2})	θ_0(deg)
CB-CB-CB	25	180

Lennard-Jones Parameters for Non-Bonded Interactions

atom type	σ (nm)	ϵ (kJ mol^{-1})
CB	0.5	3.5

Partial Charges for Long-Range Coulomb Interactions and Mass

atom name	charge (q)	mass
BRC	-0.11	179.92
CBM	0.09	150.02
CBE	0.02	169.02

Table 5.2: Particles used for fusion simulations

		Liposomes				
Name			Lipids		Water		Geometry	
		POPC	POPE	PC : PE		r_o (nm)	r_c (nm)	$2p_z$(nm)
L1		709	710	5 : 5	94040	8.4	6.2	4.2
L2		504	506	5 : 5	94040	7.4	5.2	4
PFOB-NEP								
Name	PFOB		Lipids		Water		Geometry	
		POPC	POPE	PC : PE		r_o (nm)	r_c (nm)	
N1	1000	169	170	5 : 5	77043	6.4	4.4	
N2	1000	203	136	6 : 4	77043	6.4	4.4	
N3	1000	238	102	7 : 3	77043	6.4	4.4	
N4	1000	271	68	8 : 2	77043	6.4	4.4	

5.2.2. The mean dimensions of the starting structure were 26.5 nm x 26.5 nm x 26.5 nm along the x, y and z directions.

The geometry of each particle tested for fusion is defined in Table 5.2.2. An example initial structure for fusion simulations is shown in Figure 5.1B. To start the fusion simulation, two spherical particles were placed in proximity with surrounding water sites as shown in Figure 5.1B. Two lipids, one from each particle, were selected to be connected by an intermediate water site.(72; 71) Artificial chemical bonds (linkers) were created between the water and the phosphate sites of each lipid. The initial bond lengths were usually greater than the equilibrium length of 0.5 nm. A series of short simulations were performed to gradually reduce the bond length to the equilibrium length as described below. The list of fusion pair between a liposome and PFOB-NEP is introduced in Table 5.3.2. Five replica simulations were run for fusion pair to enhance sampling efficiency.

Simulation parameters

Simulation for particle formation   Molecular dynamics simulations and analyses of trajectories were performed with GROMACS version 4.0 (92) As the first step in the simulations, an energy minimization was performed using a steepest descent method and the system was then gradually heated from 50 K to 303 K through a series of short molecular dynamics (MD) simulations. After these temperature equilibration steps, production simulations were run until the spherical PFOB-NEP and liposomes were formed.

A distance cutoff of 1.2 nm was used for non-bonded interactions in combination with the standard shift function in which both the energy and force go to zero at the cutoff distance. The LJ potential is shifted from $r_{\text{shift}} = 0.9$ nm to r_{cut} and the electrostatic potential is shifted from $r_{\text{shift}} = 0.0$ nm to r_{cut}. The simulation was performed in an isobaric-isothermal ensemble (NpT) with the Berendsen pressure coupling scheme and with coupling time of 4 ps. The temperature was kept at 303 K with the Berendsen coupling scheme with the coupling time of 0.4 ps. Time stpe of 20 fs time step was used to run a production simulation.

Table 5.3: Bulk properties of liquid PFOB. The references for each experimental bulk properties are Riess et al.(21) and Andre et al. (19) for density (ρ), Riess et al. (21), Gregor et al. (187), Faithful et al. (188) for heat of vaporization ($\Delta_{vap}H$), Song et al. (189) for the solvation free energy of CF_4 in liquid n-hexane (ΔG).

Properties	Experiment	Simulations	
		atomistic	coarse-grained
ρ (kg L^{-1})	1.925 ($\pm$ 0.007)	1.891 ($\pm$ 0.001)	1.954 ($\pm$ 7.424e-5)
$\Delta_{vap}H$ (kJ mol^{-1})	42.67 ($\pm$ 1.276)	41.05 ($\pm$ 0.26)	44.66 ($\pm$ 6.89e-3)
ΔG (kJ mol^{-1})	2.056	2.00 ($\pm$ 0.02)	

Simulation for particle fusion   The same energy minimization and temperature equilibration steps were repeated by applying the same simulation parameters as described above. After the temperature equilibration, a series of short simulations of 1 ns length were performed with decreasing the linker length by 0.2 nm after each simulation until the equilibrium length of 0.5 nm was achieved. These short simulations were followed by production simulations, each of which was performed for at most $\sim 4\mu$s. However, if a fusion complex was formed between the two particles, we stopped the simulation to invest our limited computing resources into additional replica simulations.

5.3 Results

5.3.1 Testing the coarse-grained in-house PFOB model

PFOB bulk properties To determine the bulk thermodynamic parameters including density and heat of vaporization, a simulation of a box containing 559 PFOB molecules was carried out for 100 ns at 298 K. Another simulation of a single PFOB in the same box was carried about for 100 ns at 298 K to compute the heat of vaporization. The procedures to compute these thermodynamic quantities were described previously .(218) As summarized in the Table 5.3, the density was 1.954 kg L^{-1} and the heat of vaporization was 44.66 kJ mol^{-1} when a box of PFOB was simulated at 298 K with the developed parameters. The results showed reasonable agreement with the experimental results of 1.925 kg L^{-1} for density and 42.67 kJ mol^{-1} for heat of vaporization.

PFOB-water interfacial structure After preparing the LJ parameters, the phase separation of PFOB in water was tested in the absence and in the presence of emulsifying POPC monolayer. The results were compared to the structures from previous atomistic simulations.(218) The density profiles showed good agreement between coarse-grained and atomistic simulations, supporting our in-house coarse-grained model (Figure 5.2).

5.3.2 Spontaneous emulsion and liposome formation

PFOB-NEP emulsion particles To test if PFOB-NEP emulsions will form spontaneously, the components (phospholipids, PFOB and water sites) of the system were randomly mixed and simulated under equilibrium conditions. The emulsion formed rapidly: even after accounting for approximately 4-fold faster time scale of the CG model (88), formation occurs in less than a few hundred nanoseconds. As shown in Figure 5.3, PFOB molecules aggregate while amphipathic phospholipids were expelled to the surface of the growing PFOB particles. Finally, small PFOB particles merged and became a single continuous entity in a toroidal shape. The hole in the middle

97
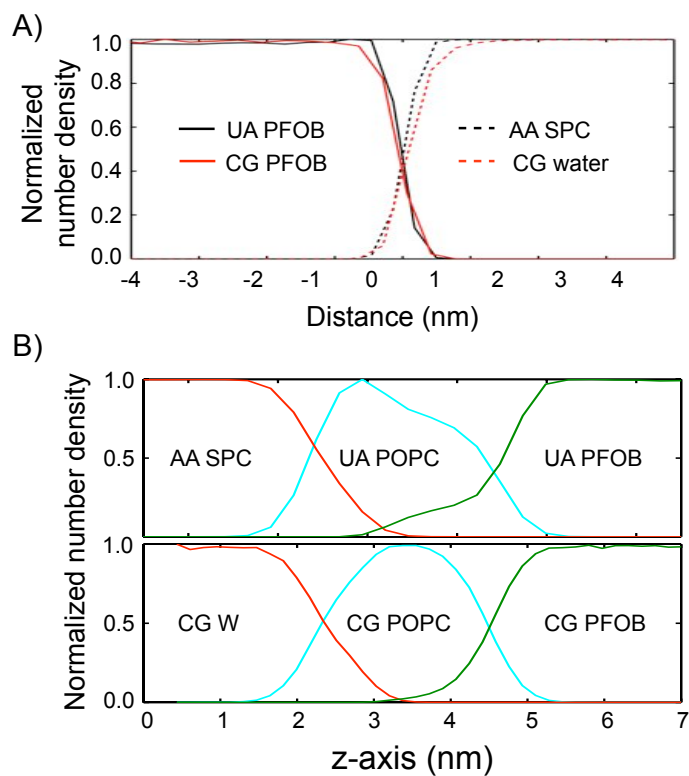
Figure 5.2: Interface structure comparison between atomistic and coarse-grained simulations A) in the absence and B) in the presence of an emulsifying phospholipid monolayer. A) The normalized number density profiles of water are shown in dotted red (coarse-grained) and black (atomistic) lines along the interface normal direction. Those of PFOB are shown in solid red (coarse-grained) and black (atomistic) lines. B) The top panel presents the normalized number density profiles of water (red), POPC monolayer (cyan), and PFOB (green) that were determined from an atomistic simulation. The bottom panel presents the same data that were determined from a coarse-grained simulation.
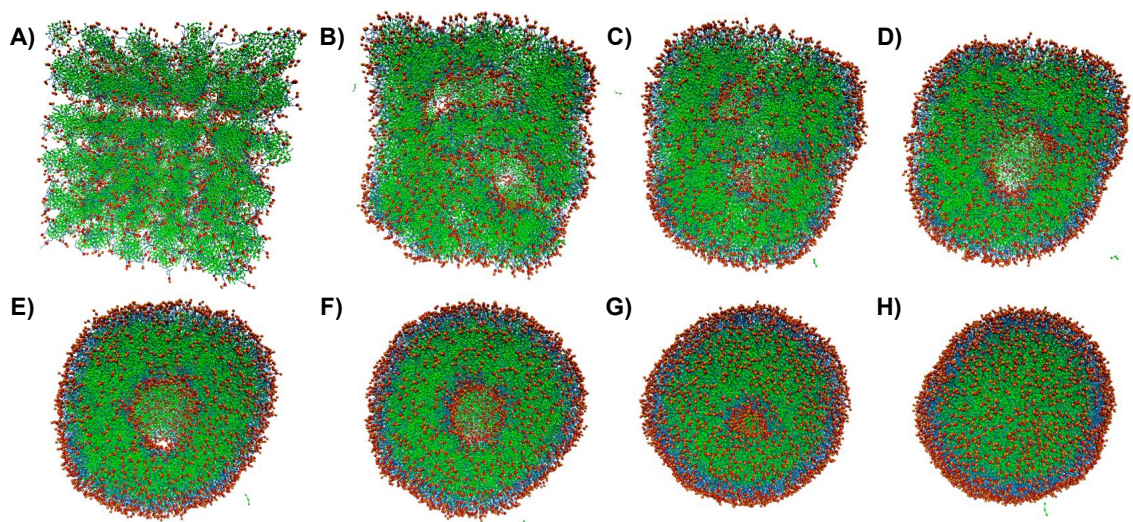
Figure 5.3: Spontaneous emulsion formation. Snapshots were taken at every 1.5 ns along the trajectory for the first 6 images (A-F). G was taken at 13.5 ns and H was taken at 22 ns, by which time the PFOB-NEP formation was complete. PFOB is shown in green, lipid tails in blue, and lipid polar head groups in red and orange. Water particles are omitted for clarity.

gradually decreased and PFOB molecules took a spherical shape with phospholipids covering the surface. The structure of a complete PFOB-NEP was defined by its outer radius (r_o), which is the distance between the center of mass and the peak of phosphate group density, and r_c, which is the distance between the center of mass and the peak of terminal methyl carbon sites (Figure 5.1B).

We occasionally observed incomplete PFOB-NEPs that contained a water droplet inside. The water droplet was also enclosed by a phospholipid monolayer, even after significant length of simulation (close to 1 μs), and it did not disappear. These structures would form when the system contained surplus lipids compared to the amount of PFOB. Therefore, when this was observed, we ran separate simulations after reducing the number of phospholipids to obtain complete PFOB-NEPs.

Table 5.4: Summary of simulations and result for fusion events. [a]The fusion mechanisms corresponding to each name are denoted by a letter and are described in Fig. 5.8. [b]The reaction coordinate of this fusion event couldn't be determined.

Name	System Size (sites)	Simulation Length (ns)	T_{S1} (ns)	T_{S4} - T_{S1} (ns)	Monolayer disruption [a]
		Liposome - Liposome			
L1-L1	225000	4000	-	-	
L2-L2	214353	3500	-	-	
		Liposome - PFOB-NEP			
L1-N1-1	219757	1080	366	57	C
L1-N1-2	"	3030	2533	95	B
L1-N1-3	"	1150	584	71	A
L1-N1-4	"	1449	1210	72	D
L1-N1-5	"	730	484	75	D
L2-N1-1	214441	770	217	45	D
L2-N1-2	"	1790	1427	47	D
L2-N1-3	"	1200	160	50	D
L2-N1-4	"	1183	994	48	D
L2-N1-5	"	410	183	41	D
L2-N2-1	212623	710	199	39	C
L2-N2-2	"	730	615	34	D
L2-N2-3	"	750	147	49	D
L2-N2-4	"	410	82	47	D
L2-N2-5	"	806	436	45	D
L2-N3-1	212623	1720	1138	45	C
L2-N3-2	"	1510	961	37	C
L2-N3-3	"	700	425	49	B
L2-N3-4	"	616	350	63	D
L2-N3-5	"	3270	3050	63	B
L2-N4-1	212623	2000	1576	33	B
L2-N4-2	"	4300	4000	-[b]	-
L2-N4-3	"	3500	2770	48	C
L2-N4-4	"	1974	1512	56	B
L2-N4-5	"	4300	-	-	-

Liposomes Liposomes were spontaneously generated starting from bicelles.(90) Transformation into a spherical liposome is the only way to stabilize the lipids in a bicelle structure by reducing energetically unfavorable interactions between solvent exposed lipid tails and water molecules. The L2 liposome (Table 5.2.2) used in our simulation was the smallest that could be formed spontaneously from a bicelle. A smaller bicell failed to form liposomes due to high curvature stress (data not shown). In addition to r_o and r_c, the structure of a liposome is defined by $2p_z$, which is the distance between two phosphate density peaks (Figure 5.1B).

5.3.3 Fusion simulations

To test the dependence of fusion between PFOB-NEPs and liposomes on lipid composition and particle size, respectively, a variety of PFOB-NEPs and liposomes were generated as described. The tested liposome sizes were 8.4 nm and 7.4 nm in radius (r_o). The lipid composition of PFOB-NEP varied from 20 mol% to 50 mol% of POPE with the remainder POPC. The details for the combinations of different PFOB-NEP and liposomes are summarized in Table 5.3.2.

Fusion between the two particles was observed in all simulations except one simulation (L2-N4-5) in the simulation time limit of ~ 4 μs. All the fusion events followed the process presented in the Figure 5.5. After the two monolayers were merged, PFOB molecules moved into the intermonolayer space of the fused liposome and became evenly distributed while the lipids from the PFOB-NEP were mixed into the outer monolayer of the liposome. As a result of the fusion, the $2p_z$ distance increased by 2 nm due to the absorption of PFOB (see p.143 figure 7.9).

Fusion process

To define different states along the fusion process, we used as a metric R_{CM}, the distance between the center of mass of PFOB molecules and the inner monolayer of liposome. Figure 5.4 shows an example of how R_{CM} changes over the course of fusion. Four different states were defined based on the R_{CM}. R_{CM} fluctuated around its mean value that was close to the sum of r_o for each of the two particles. After a lag time,
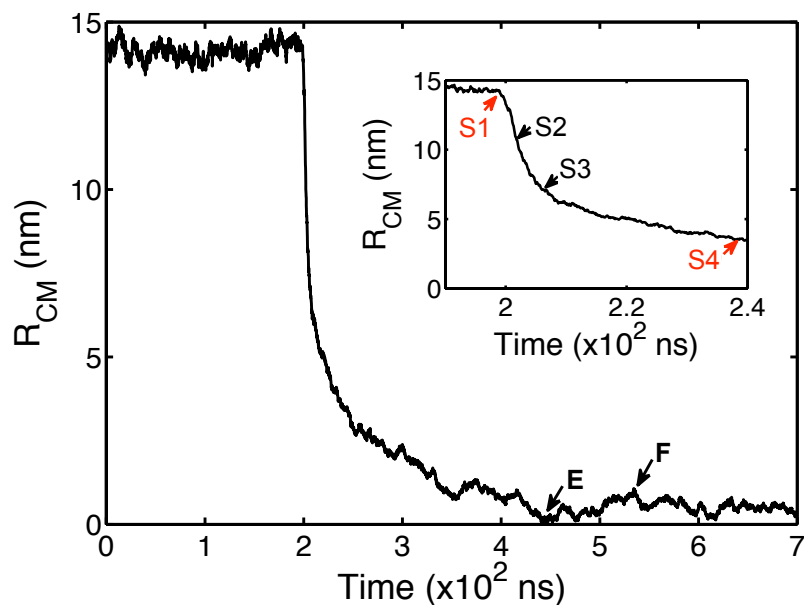
Figure 5.4: A reaction coordinate to define fusion process. The evolution of R_{CM}, the distance between the center of mass of each particle, is plotted as a function of time. Once the fusion is initiated, R_{CM} rapidly decreases to zeros. The time points designated by arrows are when R_{CM} starts to decrease (S1), when R_{CM} is decreased by 25 % (S2), when R_{CM} is decreased by 50 % (S3), and when R_{CM} is decreased by 75% (S4). R_{CM} does not stably converge to zero but fluctuating after fusion is complete. Time points E and F are somewhat arbitrarily chosen to show the structure of the PFOB-NEP and liposome complex after fusion. The corresponding structures of the two particles at each time point are shown in Figure 5.5. This exemplary R_{CM} profile was obtained from the fusion simulation L2-N2-1.

R_{CM} started to drastically decrease, indicating the initiation of fusion (S1). Three additional states were defined by the decrease of R_{CM} by 25 (S2), 50 (S3), and 75 % (S4). The structure of the particles at each state are shown in Figure 5.5. At 25 % decrease (S2), the two monolayers are fully merged and the two particles have a snowman shape with slight dent at the merged point (Fig. 5.5B). At 50 % decrease (S3), the dent at the merged point is almost disappeared and the fused particle has an elongated sphere shape (Fig. 5.5C). At 75 % decrease (S4), PFOB molecules are distributed, though uneven, all around the intermonolayer space, and the fused particle has a spherical shape with a slight bulge where the fusion event initiated (Fig. 5.5D).
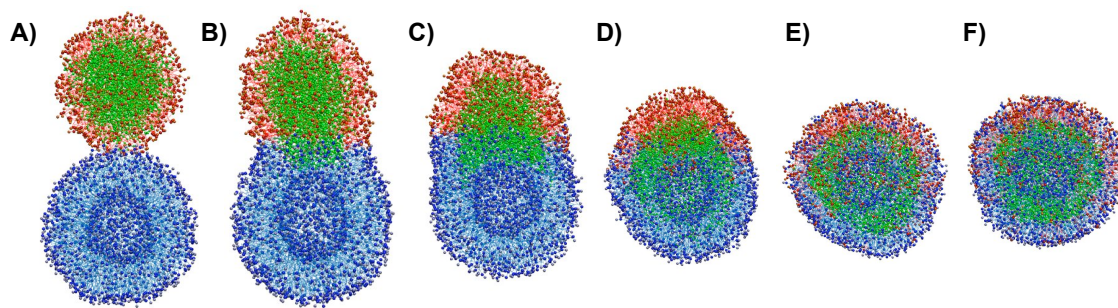
Figure 5.5: Fusion process. The structures of the two particles over the course of fusion are shown at the corresponding time points introduced in Figure 5.4. A) is at S1, B) S2, C) S3, D) S4, and E) and F) show the structures at the points designated as E and F in Figure 5.4. PFOB is shown in green, the lipids enclosing the PFOB core in red, and the lipids forming the liposome in blue.

Beyond the S4 state (75 % decrease), PFOB evenly distributes in the intermonolayer space and lipids of the absorbed PFOB-NEP mix with the outer monolayer of the fused liposome. R_{CM} is not sensitive to these changes and additional states were not defined by changes in R_{CM}. Instead, we employed the distance between the center of mass of PFOB molecules and the emulsifying lipids of PFOB-NEP. The exemplary profile is shown in Supplementary Materials (see p.144 Figure 7.10).

This profile showed that the homogeneous mixing took a long time and that a complete sampling for these processes was beyond the limit of our computing resources.

Initiation of fusion

Figure 5.6 illustrates the molecular details of the initiation steps that correspond to the events shortly before and after the first state (S1). Fusion started with a local perturbation in the monolayer PFOB-NEP and progressed with the exposure of hydrophobic compartment (either phospholipid tails or PFOB or both) to the contact interface. The local perturbation in both monolayers created a narrow and very short lived hemifusion complex. The expansion of this narrow pathway quickly followed due to flow of PFOB molecules from the NEP to the intermonolayer space of the fused liposome.

To understand the role of the liposome and emulsion components in initiating fusion, the composition of the interface region was assessed around the first state (S1). To assess the composition, first the whole system was transformed by a translation and rotation so that the molecular axis connecting the center of mass of each particle was on the z-axis. Then the system was divided into thin slabs of 0.1 nm in thickness along the z-axis. To locate the slab at the interface, the number of lipid sites (CG beads) was counted for each slab. The contact interface was identified from the minimum number of lipid sites.(55)

Thinning of the water layer at the contact interface   To examine if the initiation of fusion was accompanied by dehydration at the contact interface, the number of water sites at the interface was counted. But in this case, we additionally applied a distance cutoff of 3 nm from the z-axis so that the fluctuation in the bulk region would not screen the change that occurred within small area at the beginning of fusion.

Figure 5.7A shows the changes in the number of water at the interface. The number of water at the interface fluctuated in the range of $15 \sim 22.6$ at the interface. A drastic decrease in the number was observed upon the fusion event, which showed that the fusion was accompanied by dehydration at the interface.

Protrusion of hydrophobic moieties   Protrusion of hydrophobic moieties to the membrane surface is known to be a rate limiting step of membrane fusion.(242) To explore the participation of hydrophobic molecules in initiating fusion, the appearance of lipid tails and PFOB was assessed in the same manner by counting the CG beads of each molecule at the interface. The lipids of PFOB-NEP and liposome were treated separately.

As shown in Figure 5.7A, the appearance of lipid tails and PFOB followed the dehydration at the interface. The sequence of appearance of these hydrophobic moieties was various among different fusion events. Figure 5.7B shows the frequency to observe at the interface each hydrophobic moiety first, second, and third in sequence. Interestingly PFOB was most frequently observed as the first hydrophobic moiety at the interface and was followed by the lipid tails of PFOB-NEP.

104

The appearance of next hydrophobic moiety at the interface followed no later than 100 ps, which corresponded the sampling frequency limit. To classify the different modes of fusion initiation, if the appearance of additional hydrophobic moieties occurred within 0.3 ns, their appearances were considered to be simultaneous. With this additional condition, 23 fusion events were categorized into four different modes. The abnormal fusion event observed in the simulation L2-N4-2 was excluded in this analysis. The mode assigned to each fusion simulation is presented in Table 5.3.2, and exemple structures of each mode are shown in Figure 5.8.

In mode A, PFOBs first appeared at the interface and the appearance of lipid tails followed after 0.4 ns, which was observed only in one fusion event (L1-N1-3). In mode B, PFOB and PFOB-NEP lipid tails first appeared at the interface, which was followed by the appearance of liposome lipid tails after $0.3 \sim 0.5$ ns. This order was found in 5 fusion events (L1-N1-2, L1-N1-4, L2-N3-3, L2-N3-5, L2-N4-1, and L2-N4-4). In mode C, lipid tails from both PFOB-NEP and liposome were first observed at the interface and the appearance of PFOB was delayed by $0.5 \sim 0.9$ ns. Four fusion events belonged to this group (L1-N1-1, L2-N2-1, L2-N3-1, and L2-N3-2). In mode D, which included the remaining 13 fusion events, all three moieties appeared at the interface simultaneously.

5.3.4 Dependence of fusion on particle size and lipid composition

To determine the effect of particle size and lipid composition on this fusion process, each fusion simulation was analyzed based on the reaction coordinates introduced above. First the lag time dependence on the particle size was examined. The particles had the constant lipid composition of POPC:POPE=1:1 and the radius of liposomes varied from 8.4 (L1-N1) to 7.4 nm (L2-N1). Figure 5.9A shows an obvious trend that greater particle size increased the fusion lag time. However, the difference is not statistically significant at a 95 % confidence level.

Then the lag time dependency on lipid composition was examined while the particle size was kept constant. To test the influence of negative spontaneous curvature, the proportion of POPE decreased from 50 to 20 mol %. Figure 5.9B indicates that the

smaller fraction of POPE increased the lag time. The lag time differences of L2-N4 from L2-N1 and L2-N2 were statistically significant at a 95 % confidence level.

On the other hand, following fusion processes after fusion was initiated occurred almost indistinguishably and quickly (see see p.145 Figure 7.3 and p.146 Figure 7.12 in the Supplementary materials). The duration for the change from S1 to S4 was statistically different between L1-N1 and L2-N1, which is only due to the greater size of the L1 than L2.

5.3.5 Order parameter dependence on particle size and lipid composition

Order parameters of lipid tails were examined to determine if particle size and different lipid composition affected the flexibility of the tail conformation. The deuterium order parameters (S_{CD}) were computed with the following relation (243)

$$S_{CD} = \frac{2}{3}S_{xx} + \frac{1}{3}S_{yy},\tag{5.1}$$

where S_{ij} is an element of an order parameter tensor S and is defined by

$$S_{ij} = \frac{1}{2}\left\langle 3cos\theta_i cos\theta_j - \delta_{ij}\right\rangle, i, j = x, y, z.\tag{5.2}$$

In the equation, θ_i is the angle between the ith molecular axis and the sphere normal that is defined by a vector from a center of mass of the particle to the phosphate group of each lipid, and the bracket implies averaging over time and molecules. The molecular axes are defined per CG bead along the tail. For the nth bead (C_n), the z axis was defined by a vector from C_{n-1} to C_{n+1}, the y axis by a vector perpendicular to z and in the plane formed by C_{n-1}, C_n, and C_{n+1}, and the x axis by a vector perpendicular to y and z.

The deuterium order parameters computed for each CG beads along lipid tails of a liposome (L1, L2) and a PFOB-NEP (N1, N2, N3, N4) are shown in Figure 5.10. The order parameters of palmitoyl (left) and oleoyl chain (right) are plotted separately. It was observed that greater the particle size, was correlated with greater the order

parameters, which indicated that conformational freedom was reduced as the particle size increased. Even though decreasing the POPE fraction did not affect the tail order substantially, the order parameters of oleoyl chain (C_2 and C_3), were statistically greater in the particles containing reduced amount of POPE as shown in the Figure 5.11.
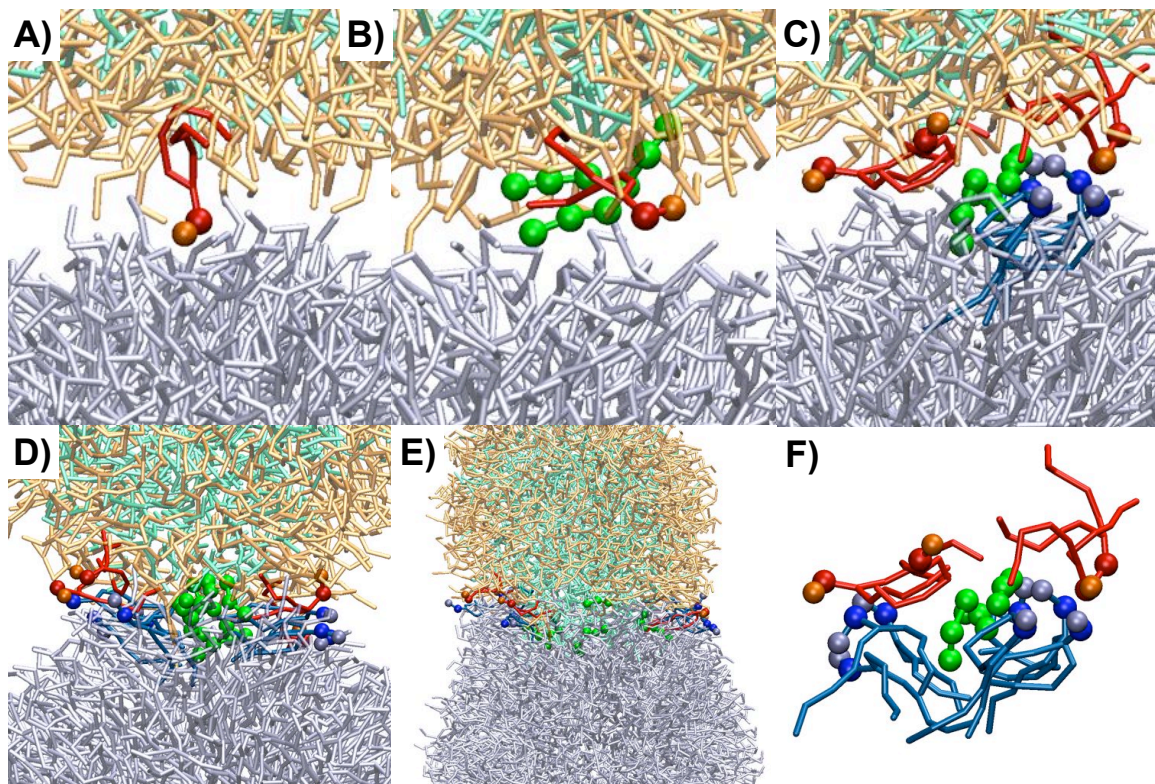
Figure 5.6: Molecular details at the initiation stages. The molecular details between the A and B stage shown in the Figure 5.5 are captured. A) Initial monolayer perturbation that led to the fusion. B) Disruption of the monolayer via the protrusion of a lipid in alliance with PFOB molecules. C) Disruption of outer monolayer of the liposome and creation of hydrophobic pathway connecting the two particles. D) Flux of PFOB through the pathway to the hydrophobic lumen of the liposome and parallel stacking of lipid along the circumference at the initiation site. E) Widening of the pathway and massive flux of PFOB-NEP. F) The initial hydrophobic pathway as shown in C with other molecules omitted for clarity. Lipids and PFOBs that directly involved in the initial monolayer disruption are depicted in darker colors and thicker sticks and additional balls while the rest of the molecules are shown in thinner sticks and faint colors. PFOBs are shown in green and light green colors with the enclosing phospholipids in red and orange colors. The phospholipids of the liposomes are shown in blue and light blue.
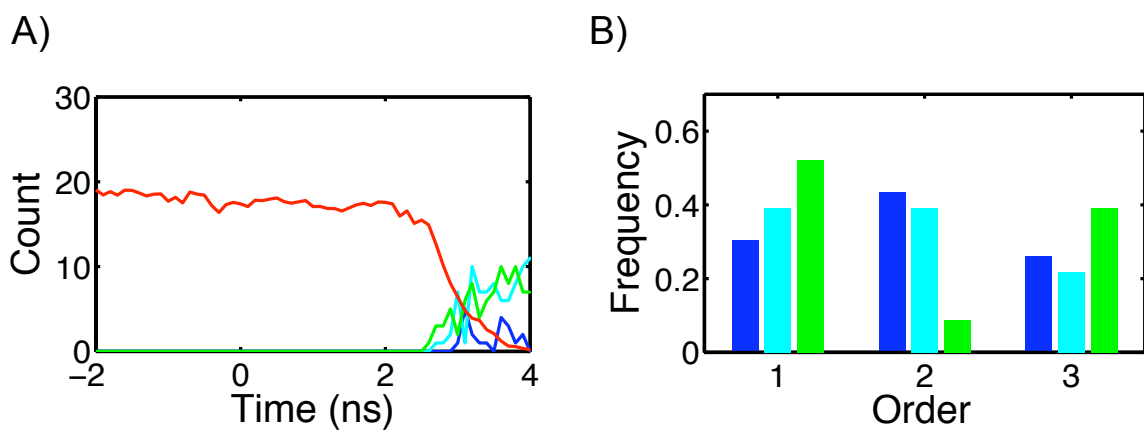
Figure 5.7: Changes in chemical composition at the interface. A) The evolution of the number of water (red) and each hydrophobic moiety (blue: lipid tails of liposome, cyan: lipid tails of PFOB-NEP, green:PFOB) at the interface is plotted with S1 state set at zero in time. This particular profile was obtained from the fusion simulation L2-N4-1. B) The frequencies to observe the hydrophobic moieties at the interface first, second, and third was plotted with the same color code used in A.
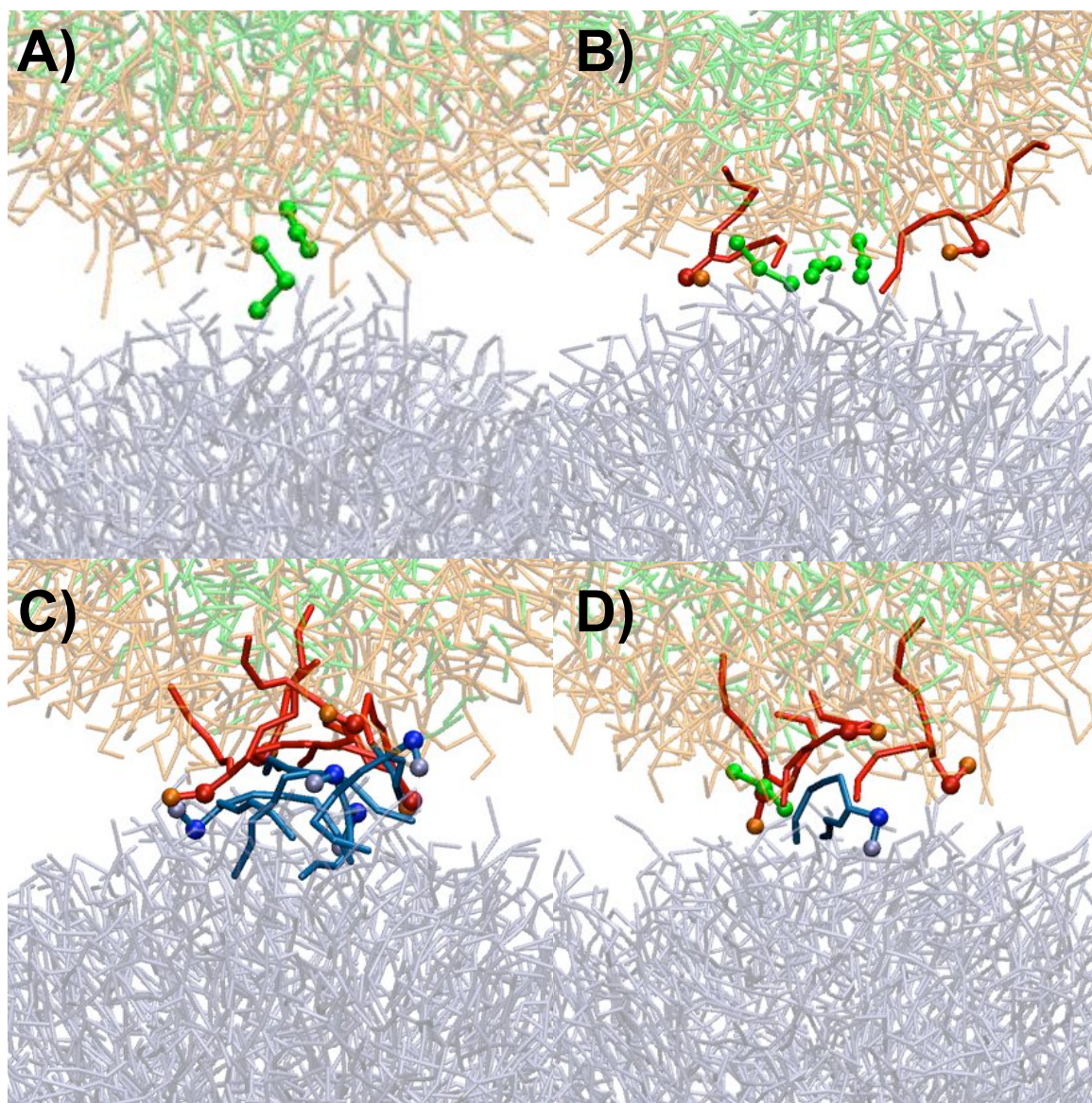
Figure 5.8: Different membrane disruption modes to initiate the fusion. A) Primary action of PFOB prior to the protrusion of lipids. B) Protrusion of PFOB-NEP lipid in alliance with FPOB molecules (solid red) C) Protrusion of lipids in the absence of PFOB molecules. D) Collaboration among three molecules. The same color codes and shapes are used as in Figure 5.6.
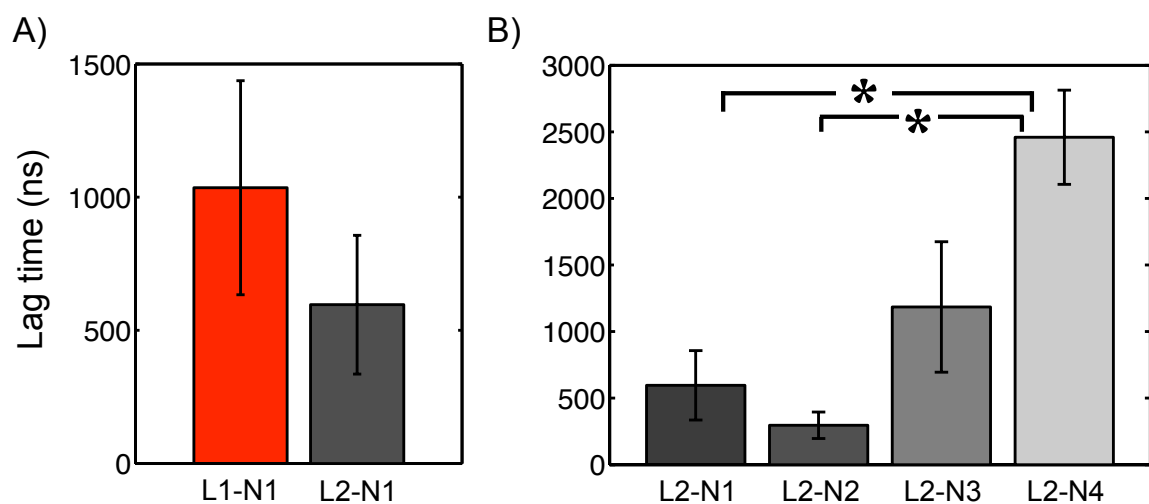
Figure 5.9: Fusion dependence on the particle size and lipid composition. A) The lag times for the fusion initiation are compared among fusion simulations that differ in comprising particle size as shown in the Table 5.3.2 at a constant lipid composition of POPC:POPE=5:5. B) The lag times are compared among the fusion events between a liposome and various PFOB-NEPs that contained different amount of POPE from 50 to 20 mol% while the particle sizes were the same. The differences of the designated pairs are statistically significant at a 95% confidence level.
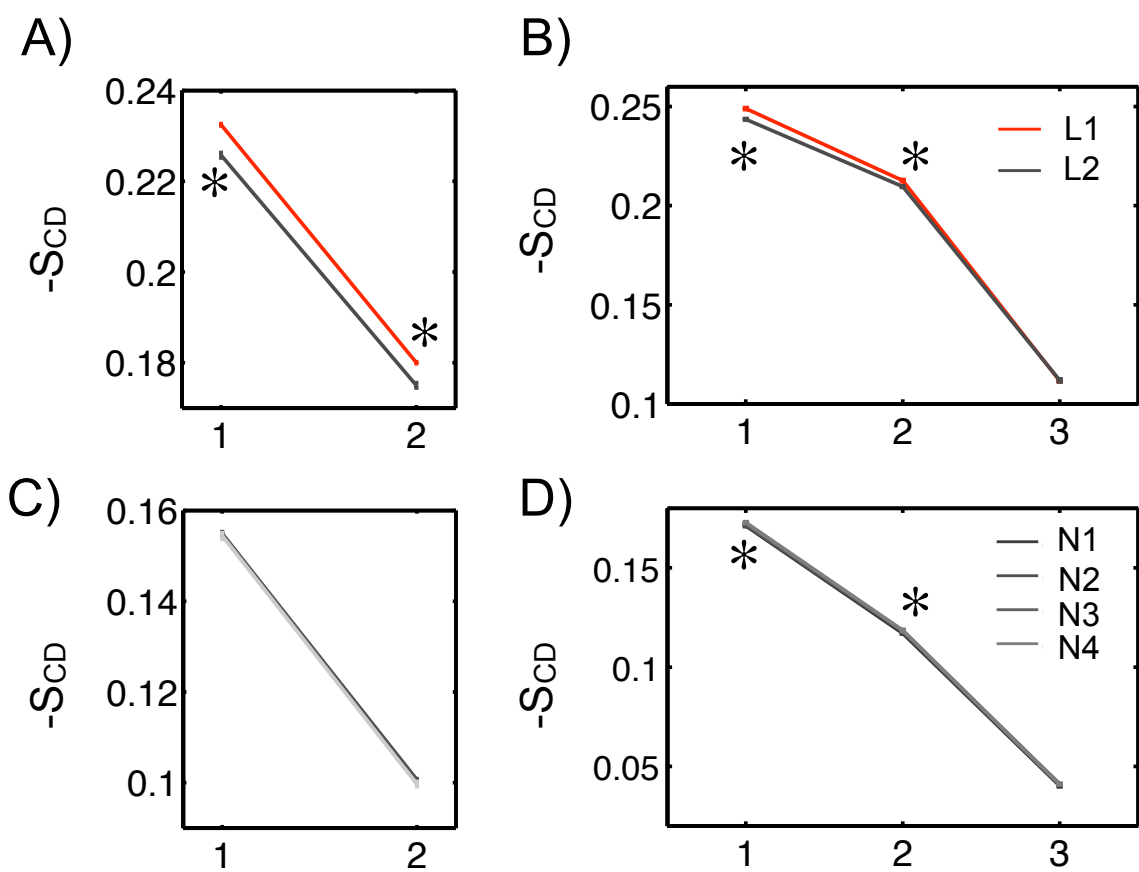
Figure 5.10: Lipid tail order parameters of Liposome and PFOB-NEP. The lipid tail oders of sn-1 palmitoyl chain (A) and sn-2 oleoyl chain (B) of liposomes are plotted. The lipid tail oders of sn-1 palmitoyl chain (C) and sn-2 oleoyl chain (D) of PFOB-NEPs are plotted. The differences of the designated pairs are statistically significant at a 95% confidence level.
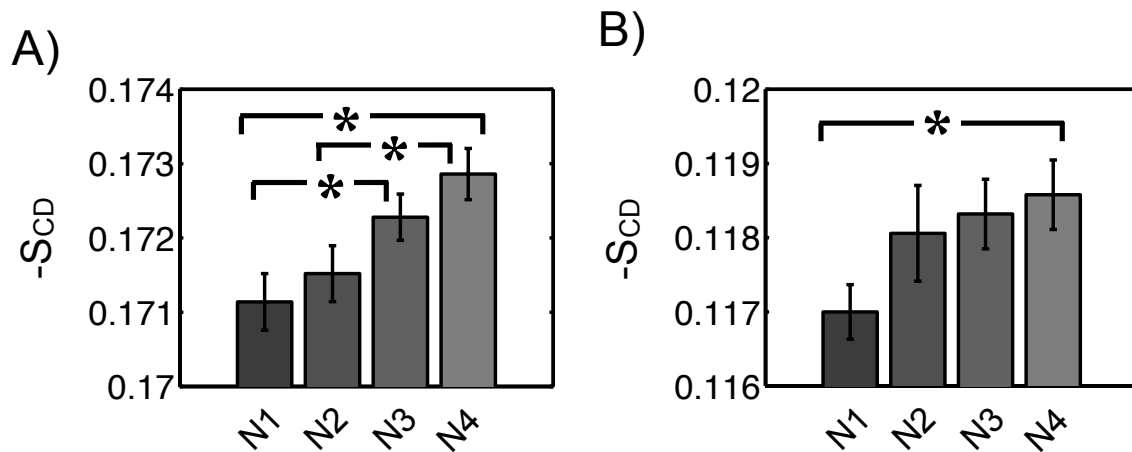
Figure 5.11: Statistically different tail orders among PFOB-NEPs. A) The tail orders at the C_2 position (A) and C_3 position of the oleoyl chain are plotted. The differences of the designated pairs are statistically significant at a 95% confidence level.

5.4 Discussion

To better understand the "contact-facilitated" delivery mechanism, we developed force field parameters at a coarse-grained level, generated particles using equilibrium simulations, and ran fusion simulations by placing a PFOB-NEP and a liposome after physically linking them. We have observed 24 fusion events for different combinations of PFOB-NEPs and liposomes, which strongly supports the contact-facilitated delivery mechanism. To authors' best knowledge, this is the first demonstration of fusion between liposomes and nanoemulsion particles enclosed by a phospholipid monolayer. This process shared some features with the well-established fusion process between two bilayers but also exhibited distinctive features as discussed below.

5.4.1 Force field parameters

The newly developed coarse-grained PFOB model was able to reproduce the bulk thermodynamic properties of PFOB in reasonable agreement with experimental observations. The interface structures determined at a coarse-grained model in combination of this new model and the MARTINI force field showed good agreement with the structure determined by atomistic simulations both in the absence and presence of an emulsifying phospholipid monolayer. Additionally, the spontaneous formation of PFOB emulsion droplets enclosed by a phospholipid monolayer starting from random mixtures of PFOB, phospholipids, and water further supported our model.

Even though non-zero partial charges were assigned to the three interaction sites to preserve the asymmetric nature of PFOB, PFOB behaved symmetrically without showing preferential orientation near the PFC-NPE surface. The small partial charges were not influential under these simplified simulation conditions. Hence, in the future, simulation performance could be enhanced by excluding these charges with no penalty to the simulation accuracy.

5.4.2 System configuration

To observe fusion events within the limit of our computing resources, a few constraints were imposed into the system configuration. First, very small sized particles were used, which has been common for vesicle fusion simulations.(90; 244; 72; 71; 55) Small size can both speed up the simulation and facilitate fusion between membranes due to pronounced curvature. The smallest liposome size of ∼15 nm in diameter corresponded to the minimum liposome size feasible in experiments.(245) The smallest PFOB-NEP size ∼ 13 nm in diameter was far below the experimentally-observed minimum PFC-NEP size of ∼ 50 nm in diameter.(27) By using these small sized particles, we demonstrated the effect of local curvature on the surface PFC NEPs and target cell membranes to initiate fusion. Indeed, recently it was reported that synaptotagmin (fusion protein) could induce high local positive curvature with a diameter of about $17.5 \pm 3nm$ and reduce the energy required to initiate membrane fusion.(246; 247)

Second, the two particles were placed very closely and connected by an artificial linker that would maintain the initial close proximity between the two particles. Spontaneous apposition between the two particles are energetically hindered due to electrostatic repulsion and dehydration penalty and will occur only with the help of molecular interactions such as ligand-receptor interactions. Including these additional macromolecules should make the system size and the simulation length far greater than the current simulations, which is simply unaccessible by MD simulations. Therefore, close apposition manifested by an artificial linker has been used in many recent fusion simulations.(71; 72; 55)

It is known that the interaction of PFOB-NEPs with the target cells became much more efficient in the presence of target cell specific ligands on their surface.(47; 248) It is obvious that such ligand-receptor interactions would lead to close apposition of the two particles as modeled in our simulations. Therefore, even though these artificial linker constraints were employed to overcome the limited computing power, they also described the geometry expected for receptor-mediated nanoemulsion interactions with biological membranes.

5.4.3 Different mechanisms for hemifusion complex formation

The 23 successful fusion events, excluding an abnormal fusion event (L2-N4-2), revealed four different modes for the disruption of the monolayers (Figure 5.8) as listed in Table 5.3.2. Three of the modes (A, B, and D) showed that PFOB played primary roles in initiating membrane disruption and lipid complex formation. In mode A, PFOB leaked, prior to the reorientation of lipids, into the interface and subsequently triggered membrane disruption. In modes B and D, PFOB also facilitated the reorientation and protrusion of lipid tails by solvating the hydrophobic tails exposed to surface. However, the boundaries between these modes were somewhat indistinct, and in any mode the interplay between phospholipids and PFOBs was prevalent. This aspect again emphasizes the critical role of PFOB for the initiation of fusion.

5.4.4 Transient hemifusion complex and complete absorption of PFOB-NEP

"Contact-facilitated" delivery mechanisms originally hypothesized that the two particles would stay intact with a hemifusion complex spanning the gap and providing continuous hydrophobic surface between the two particles.(47) The hypothesis was based on experimental observations as shown in Figure 5.12A as well as on the lipophobic property of PFOB that would maintain emulsion core even after a hemifusion stalk formed.

In contrast to the hypothesis, our simulations showed that hemifusion complexes are very short-lived, quickly expanding radially to allow the massive flow of PFOB into the intermonolayer space, finally leading to the complete absorption of PFOB-NEP into the apposed liposome. The fusion process that ended with a complete absorption of PFOB-NEP into the liposome disagreed with the original hypothesis.

A few distinctive conditions between the real and our *in silico* systems suggest the determinants behind this molecular event. First of all, the small particle size generates high curvature strain and surface tension that drive the system to minimize the surface area for a given volume. In our simulations, the complete absorption was the only way
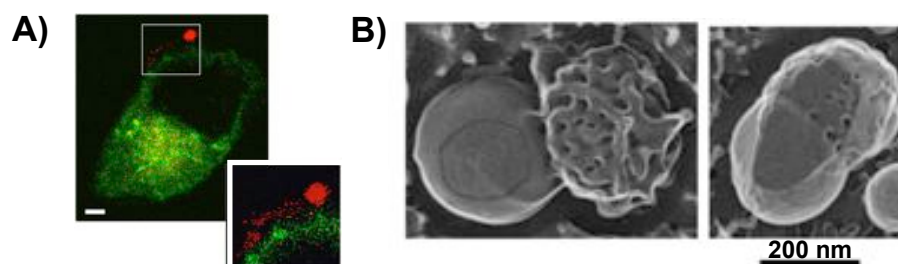
Figure 5.12: Experimental observations supporting the contact-facilitated delivery mechanism. A) Lipid streaming into the plasma membrane. Rhodamine-labeled lipids (red) on the surface of nanoparticle diffused onto the adjacent cell expressing a green cytoplasmic marker. Dark circular region is nucleus. Reprinted with permission from Crowder et al. (248) B) The freeze-fracture transmission electron micrographs of a PFOB-NEP and liposome in direct contact. Reprinted with permission from Soman et al. (11)

to maximize such reduction in the total surface area. In reality, such a high curvature strain can arise only locally at the expense of significant energy.(244; 56; 242; 71) Second, our systems are extremely pure without including any proteins in both particles. The flow of PFOB into the apposed liposome separates the two monolayers and thickens the membrane. In plasma membranes containing high fraction of transmembrane protein, thickening of membrane would not be as energetically favorable by inducing hydrophobic thickness mismatch.(249) Additionally our simulations used a single flexible linker to keep the two particles in close proximity while the close apposition of PFC-NEPs to their target cells are mediated by multivalent ligand-receptor interactions. It is geometrically unlikely to happen to have a ligand and receptor pair in the same monolayer. Hence, the multivalent ligand-receptor interactions should keep PFC-NEPs from being absorbed into the target cells.

The last two arguments gain support from the other experimental observation shown in Figure 5.12B. In this experiment, the contact between the two particles was driven by dehydration while they were concentrated upon centrifugation.(35) The figure shows a PFOB-NEP and a model liposome in contact due to dehydartion. The morphology of the contacted particles corresponds well to the intermediate fusion state shown in Figure 5.5C. In the absence of ligand-receptor interactions, the highly curved hemifusion complex was difficult to be maintained.

5.4.5 Fusion dependence on particle sizes and lipid compositions

It is well known that smaller liposomes are more fusogenic than larger ones due to more flexible lipid tails and higher exposure of hydrophobic tails.(56; 250; 251) The fusion between the monolayer of PFC-NEP and the outer monolayer of liposome exhibited the dependency on the particle size in the same manner as in the fusion between two bilayers. However, the dependency is yet to be confirmed by additional replica simulations.

Lipids of negative spontaneous curvature are known to facilitate membrane fusion between the two outer monolayers because they can accommodate the highly negative curvature (dent) that occurs during hemifusion stalk formation.(252) We observed this dependency in our fusion simulations. Lower fractions of POPE ($\sim$ 20 mol%) prolonged the lag time for the initiation of fusion compared to the PFOB-NEP contained higher POPE fractions (50 and 40 mol%). The prolonged lag time was statistically significant. In particular we did not observe fusion between L2 and N4 in one simulation (L2-N4-5) with a low fraction of POPE molecules, until the simulation reached the time limit of computing resources. Correlated increases in order parameters with increasing liposome size and decreasing POPE proportion help to explain the cause of the prolonged lag time, which is further discussed below.

5.4.6 Correlation of lipid tail order with fusion

In the previous study using atomistic models, significantly more ordered lipid tail conformations were detected in the monolayer of PFOB-NEP than in the control bilayer.(218) Unlike this previous observation, in this study we found that the tails were significantly disordered in the PFOB-NEPs than in the liposomes. We believe that different particle size attributes to this difference. Smaller PFOB-NEP with much higher curvature contained less number of lipids in the same surface area. Indeed, the area per lipid of PFOB-NEP (1.52 nm^2) was substantially wider than those of liposomes (1.25 nm^2 for L1 and 1.36 nm^2 for L2). Therefore, direct comparison to the atomistic simulations in a planar geometry may not be proper.

As expected, the lipids were more ordered in the larger liposome (L1) than in the smaller one (L2). On the other hand, even though the area per head group was the same among PFOB-NEPs (N1 through N4), the higher fraction of POPE caused the lipid tails to become more disordered. The lag time enlongation was more sensitive to the increased tail order of PFOB-NEPs (4.1-fold longer) rather than to that of liposome (1.7-fold longer). It may suggest that membrane disruption be more frequently initiated in the PFOB-NEP monolayer, acting as a rate limiting step, and in turn the disruption of liposome outer monolayer be triggered. This is supported by the fact that the hydrophobic moieties of PFOB-NEP including lipid tails and PFOB were more frequently found as the first molecule at the interface than the lipid tails of liposome.

5.5   Conclusions

We have developed a coarse-grained PFOB model that preserved the thermodynamic properties of pure PFOBs as well as the phase separation in water due to its strong hydrophobicity. The validity of the model was confirmed by the spontaneous emulsion formations starting from randomly mixed initial structures.

Our simulations using this in-house CG model directly showed that fusion could occur between the monolayer of PFOB-NEP and the outer monolayer of liposome. This observation strongly supports the "contact-facilitated" delivery mechanism, which was hypothesized to proceed by forming an intermediate structure similar to the hemifusion stalk. Indeed, this fusion event between a PFOB-NEP and a liposome shared many aspects in common with the well-resolved fusion mechanisms between two bilayers. The fusion showed a similar dependence on the particle size and lipid composition. The smaller the size and the higher the lipid content of negative curvature, the faster the fusion. The fusion was initiated by forming a hemifusion complex made of hydrophobic moieties protruded to the surface. Initial membrane disruption and hemifusion complex formation were the rate-limiting steps while subsequent steps occurred very quickly and barely differed among the observed fusion events.

We also observed distinctive features that were unique to this fusion process between a PFOB-NEP and a liposome. It appeared that freely mobile PFOB molecules played critical roles to progress the fusion process. PFOB expedited the protrusion of hydrophobic moieties from the PFOB-NEP to the interface region and therefore facilitated fusion. PFOB molecules solvated lipid tails and helped the protrusion of the tail to the polar interface. It was also often observed that PFOB molecules by themselves flew into the polar interface and generated a hemifusion complex that consisted of PFOB only. Finally it was clearly seen that the massive flow of PFOB into the intermonolayer space of the apposed liposome led to the complete absorption of the PFOB-NEP into the liposome.

Even though it was closely related to the fusion mechanisms between two bilayers, the current work has laid a foundation for new studies to understand the delivery mechanism of cargo molecules to target cell through membrane fusion. Systematic analysis

to test the fusion dependency on particle size and lipid dependency as well as core-forming perfluorocarbon molecules would help to better characterize the mechanisms and to aid in the rational design of particles for optimal delivery.

Chapter 6

Conclusions

6.1 Overview of the research

This thesis work was laid out to gain insight into the functional mechanisms of perfluorocarbon-based nanoemulsion particles (PFC-NEPs) at a molecular level. Multi-scale molecular dynamics simulations have been employed to elucidate the structural details. Atomistic molecular dynamics simulations revealed the interface structure of PFC-NEP, which was characterized by extensive intercalation of core-forming perfluorocarbon molecules into the emulsifying phospholipids monolayer. Another set of atomistic simulations indicated that the intercalated perfluorocarbon molecules could affect the cargo binding to the interface region. Coarse-grained (CG) simulations of closely apposed PFC-NEP and liposome showed that they fused in a manner similar to that of the fusion pathway between two bilayers. These CG simulations directly supported the hypothesized "contact-facilitated" mechanism.

We have undergone a few problem-solving steps to progress the research. The first problem was involved with determining the system configurations. Due to limitations in computing resources, simplifications are inevitable. We have used small sized PFC-NEPs and liposomes of less than 20 nm in diameter in order to test if fusion could occur between the two particles. The sizes are much smaller than the minimum sizes for both particles. This small size rather demonstrates how strong curvature strain is required so that fusion can occur. Another important issue was the accuracy of force field parameters. It was crucial to be aware of inaccurate force field parameters to avoid this potential problem. We have used the OPLS-AA force field for protein in combination with the Berger united lipid model, which was guided by the report

that showed GROMOS united protein model exhibited overly favorable interactions with the Berger lipid model.(77) We have modified the interaction potential between CG lipid head groups and CG lipid tails. The newer MARTINI force field set their interaction potential to be super-repulsive so that penetration of ions through a bilayer would be prevented.(88) The modification, however, placed a much higher energy barrier that prevented the protrusion of lipid tails to the surface and made the lipid much less fusogenic. Hence we reversed the change so that protrusion of lipid tails would be more probable.

6.1.1 Atomistic structure determination of PFC-NEP interface

To model the PFC-NEP interface at an atomistic level, a perfluorocarbon molecule, perfluorooctylbromide (PFOB), was modeled at a united atom level to be in accordance with the Berger united lipid model. By using the in-house PFOB model, the PFOB-NEP interface was constructed in a slab-geometry and two replica simulations were performed. The system contained ∼53,000 atoms and was run for 150 ns. After we obtained equilibrated PFOB-NEP interface structures, we ran other simulations to examine cargo (melittin peptide) binding to this interface. Two replica simulations were performed for PFOB-NEP interface with an embedded melittin peptide in each monolayer. This system contained ∼40,000 atoms and was run for 300 ns. A pure POPC bilayer and a POPC bilayer with an embedded melittin peptide in each monolayer were simulated as control systems.

From the above-mentioned simulations, we have found that the core-forming PFOB intercalated in between lipids forming the emulsifying monolayer on the PFOB-NEP surface and that the monolayer became distinctive from the bilayer made of the same lipid composition. The interface structure featured by the intercalations of PFOB gained support from an experimental observation of tryptophan (Trp) fluorescence quenching upon melittin adsorption onto PFOB-NEP surface.(35) It is because the direct collision of bromine atoms with the Trp side chain is only realized when PFOB is deeply inserted into the monolayer. The simulations with embedded melittin peptides showed that the intercalated PFOB inhibited deeper penetration of melittin into the

123

monolayer on the PFOB-NEP surface and caused significant changes in melittin structure. Reduced helical content was in accordance with experimental observation.(35) The direct influence of PFOB on the melittin interaction with the monolayer indicated that the interaction of core-forming perfluorocarbon molecules with the emulsifying monolayer could affect cargo binding to this interface.

6.1.2   Coarse-grained (CG) fusion process

Testing "contact-facilitated" delivery mechanism involved much bigger systems and required coarsening of molecules in the system. Therefore, three CG beads represented a PFOB and the force field parameters were developed to be in accordance with the widely used MARTINI CG force field. A system for a fusion simulation consisted of a spherical PFOB-NEP and liposome connected by a linker and surrounding water beads. Seventeen fusion simulations were performed. The number of CG beads in a system varied from 225,000 to 212,623 and the simulation length varied from 700 to 4,300 ns.

Twenty three successful fusion events were observed out of 25 simulations. The successful fusion events proceeded along the following pathway: 1) disruption of the apposed monolayers, 2) transient hemifusion complex formation, 3) merge of two monolayers, and 4) complete absorption of the PFOB-NEP into the liposome. These simulations revealed the critical roles of the core-forming perfluorocarbon molecules over the course of the fusion event. First, PFOB accelerated the monolayer perturbation and initiated the hemifusion complex formation. Second, the massive flow of PFOB molecules via the initial hemifusion complex expedited widening of the hemifusion complex and subsequent merge of the two monolayers. Finally, the redistribution of PFOB molecules at the inter-monolayer space of the fused liposome triggered the complete absorption of the emulsifying monolayer of PFOB-NEP into the outer monolayer of the liposome.

It is well known that small vesicle size, encompassing lipids of negative curvature (phosphatidylethanolamine:PE) in the outer monolayer, and encompassing lipids of positive curvature (lysophosphatidylcholine:LPC) in the inner monolayer accelerate the complete fusion between two bilayers.(253) The fusion process observed in our

simulations also appeared to be dependent on the particle size and the lipid compositions. The smaller the size and the higher the fraction of a lipid with negative curvature, the shorter the lag time. The dependency corresponds to that of the fusion between two bilayers and the correspondence implies that two fusion events proceed in the same manner at least for the initial steps. But obviously the two fusion events should diverge beyond the stage of hemifusion stalk formation because PFOB-NEP does not have the inner monolayer to form a hemifusion diaphragm structure where two inner monolayers form a disc-shaped bilayer.(253) Indeed, we instead observed the expansion of the hemifusion complex and subsequent absorption of PFOB-NEP into the liposome. The later processes that lead to a complete absorption may arise due to extremely small particle size. We believe this high curvature would arise only locally in the real physiological systems and would be alleviated upon the hemifusion complex formation.

In conclusion, these simulations showed that two monolayers of the two particles could form a hemifusion complex as proposed in the contact-facilitated delivery mechanism. In addition to that, the simulations showed the critical roles of perfluorocarbon molecules in initiating fusion.

6.1.3   Impact

The importance of different perfluorocarbon molecules was manifested in determining emulsion particle sizes,(27; 254; 255) stability,(256) and oxygen solubility when the particles were used as blood substitutes.(257) Recently, an extensive investigation has been carried out to develop multi-modal PFC-NEP so that different epitopes can be visualized simultaneously,(14; 10; 258) which requires different PFC-NEPs made of unique perfluorocarbons. Furthermore, customized PFC-NEPs are under development for the delivery of a specific drug molecule; the mixture of perfluoropentane and coconut oil was used to form NEPs for the delivery of apomorphine for treating Parkinson's disease.(259) Based on the need to develop diverse PFC-NEPs, various perfluorocarbons have been utilized: perfluorodecalin,(260; 261; 262) perfluoropentane,(259) perfluorohexane,(263) perfluorodecylbromide,(255) perfluoro-15-crown-5 ether,(10; 14; 258) perfluorotributylamine,(261) and fluorinert.(261)
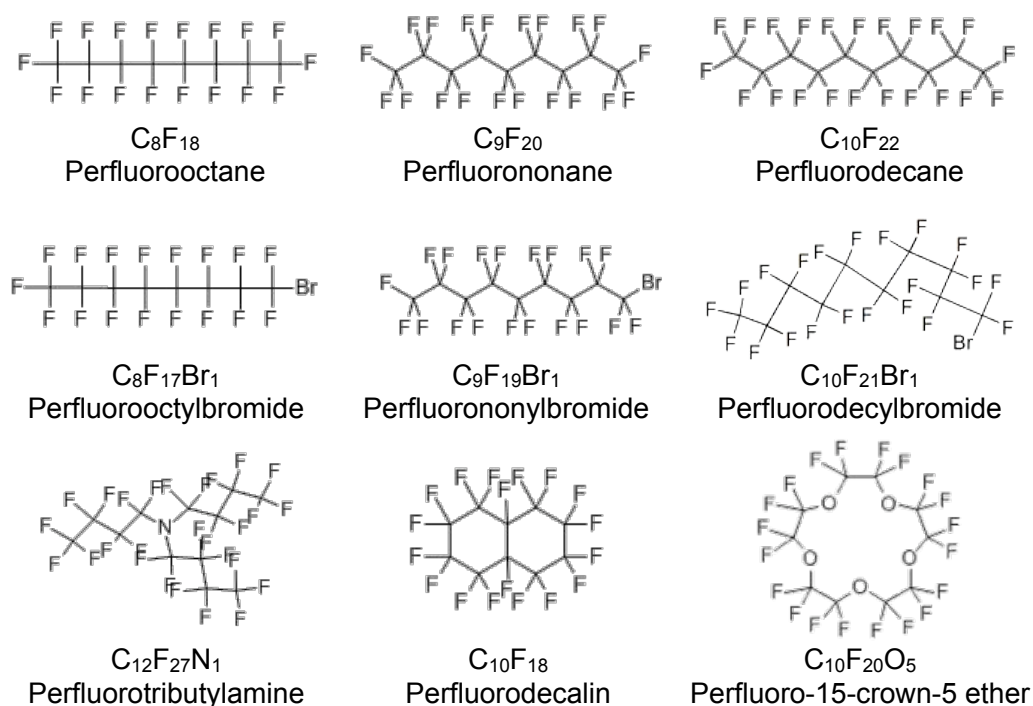
Figure 6.1: The chemical structures of various perfluorocarbons.

Our simulations have shown that the core-forming perfluorocarbon molecules play critical roles in cargo binding to the PFC-NEP interface as well as cargo delivery by promoting monolayer disruption. The former role will depend on level of interaction of PFC molecules with the emulsifying monolayer(203; 264; 210) and the latter will depend on the physical property of the PFC molecules such as vapor pressure.(265) Knowledge of these properties would suggest suited combinations of perfluorocarbons and emulsifying molecules to achieve the best outcome either for imaging, delivery or both.

6.2 Future work

Future studies would involve simulations at both atomistic and coarse-grained levels to test proposed hypotheses from the current thesis work.

6.2.1 Assess the influence of PFC intercalation on cargo binding

First, we have suggested that the mixing of perfluorocarbon is important for cargo binding. This hypothesis can be tested by the combination of atomistic simulations and experiments. The modulation of mixing would be achieved by varying the perfluorocarbon molecules in their length or shape. Experimentally it was shown that relatively shorter length was required for perfluorocarbon molecules to mix with the phospholipids monolayer.(210) Obviously the different shapes such as a linear or circular shape will differentially affect the interactions.(203)

Table 6.1: The physical characteristics of various perfluorocarbons. [a] All the physical properties were taken from the website www.chemicalbook.com except [a]. The value of [a] was from the reference (266).

Name	Molecular weight (g/mol)	Density (g/mL)	Melting Point (°C)	Boiling Point (°C)
Perfluorohexane	338.04	1.669	-4	58 ∼ 60
Perfluorooctane	438.06	1.766	-25	103 ∼ 106
Perfluorononane	488.06	1.799	-16	125 ∼ 126
Perfluorodecane	538.07	1.770	36	144
Perfluorododecane	638.09	> 1.5	75	178
Perfluorohexylbromide	398.95	1.871	-49	97
Perfluorooctylbromide	498.96	1.930	6	142
Perfluorononylbromide	548.97	1.900	27	159
Perfluorodecylbromide	598.97	1.862	65	185
Perfluorododecylbromide	698.99	11.856	87 ∼ 88	222
Perfluorobutylamine	671.09	1.883	-52	178
Perfluorodecalin	462.08	1.941	-10	142
Perfluoro-15-crown-5 ether	580.07	> 1.3	-44 ∼ -46 [a]	145

Figure 6.1 shows the chemical structures of various perfluorocarbons that can be tested in this future study. Table 6.1 shows the physical properties of the perfluorocarbons in the Figure 6.1 and additional ones. The physical properties such as melting and boiling points are important to form a stable liquid emulsion core. However, the properties drastically change depending on the chain length in the case of linear PFCs. Therefore, the length cannot be varied over broad ranges. For practical applications, it should be more meaningful to compare between linear and non-linear perfluorocarbons. First, force field parameters are to be prepared and, the PFC-interface will be generated in slab geometry. We expect that the shorter and linear PFC molecules will intercalate into the monolayer more extensively.

Melittin peptide will be used as a model cargo. The structural changes of the peptide on the surface of each PFC-NEP will be assessed and the results can be compared to the experimental observations such as helical contents and tryptophan quenching and blue shifted emission spectrum of tryptophan fluorescence. We expect that highly intercalated PFC molecules will cause more significant alterations in melittin conformation than the melittin bound to a control bilayer.

6.2.2 Prediction of ^{19}F magnetic resonance imaging intensification

Essentially no detectable background makes ^{19}F magnetic resonance imaging (MRI) advantageous over conventional MRI that detects the different nuclear spin relaxation of ^{1}H of water. However, ^{19}F MRI suffered from long image acquisition times due to relatively long T_1 relaxation time and MR signal attenuation due to short T_2 relaxation time, which mainly originated from low concentration of ^{19}F.[267]

The higher local ^{19}F concentration at the targeted sites could be achieved by applying perfluorocarbon (PFC) based nanoemulsion particles (PFC-based NEPs) with target specific ligands on their surface.[267] Interestingly besides higher local ^{19}F concentration, significantly enhanced ^{19}F magnetic resonance signal was obtained, provided that gadolinium-based contrast agents were present on the surface of PFC-based NEPs. [267; 268]

The faster T_1 relaxation of ^{19}F nuclear spins is induced by the local magnetic field fluctuations, which in turn was caused by the electron dipoles of Gd^{3+} ion. The relaxivity of Gd^{3+} ion depends on the distance between the contrast agents and resonance nuclei as well as the diffusion rate of the nuclei.[269]

Experimentally it is difficult to elucidate the distance between the Gd^{3+} ion and ^{19}F nuclei due to the lack of atomistic structure of PFC-NEP interface. Also the diffusion coefficients of ^{19}F nuclei, which should be different depending on their relative location to the PFC-NEP surface, are hard to obtain experimentally. Our atomistic simulations of PFOB-NEP interface in a slab-geometry could provide these missing pieces in experiments. Figure 6.2A shows the structure of the modeled PFOB-NEP interface and Figure 6.2B shows that the presumed mean position of Gd^{3+} ions, which is based on their chemical structure, corresponds to the height of phosphate groups. Based on this assumption, the distribution of fluorine atoms as a function of separation distance from the Gd^{3+} ion was computed and turned out to be continuously increasing starting from ~ 0.5 nm distance (see Fig. 6.3A). In addition to this distribution data, our simulations provided the diffusion coefficients of ^{19}F nuclei as a function of their distance from the NEP surface, and the diffusion coefficients were neither constant nor linear along the z-axis (see Fig. 6.3B). If these distance dependent parameters could be implemented into the theoretical calculations, which have been developed by Lingzhi in the Wickline group, the relaxivity would be more accurately predicted. The implementation and following experimental verifications will be carried out.

6.2.3   Elucidate fusion dependence on lipid compositions at a CG level

To date, we briefly tested the fusion dependence on the lipid composition. Our simulations indicated promoted fusion rates when the PFOB-NEP contained higher content of POPE of negative curvature. However, it needs additional replica simulations to obtain statistical significance. Obviously systematic analyses can follow to further elucidate the influence of different lipids on this process. The MARTINI force field contains the models of several different lipids; phosphocholines and phosphatidylethanolamine with different tails, sphingolipids, charged lipids, and cholesterol.[270] Therefore, we can test the roles of lipids of different spontaneous curvature, charge, and tail length.
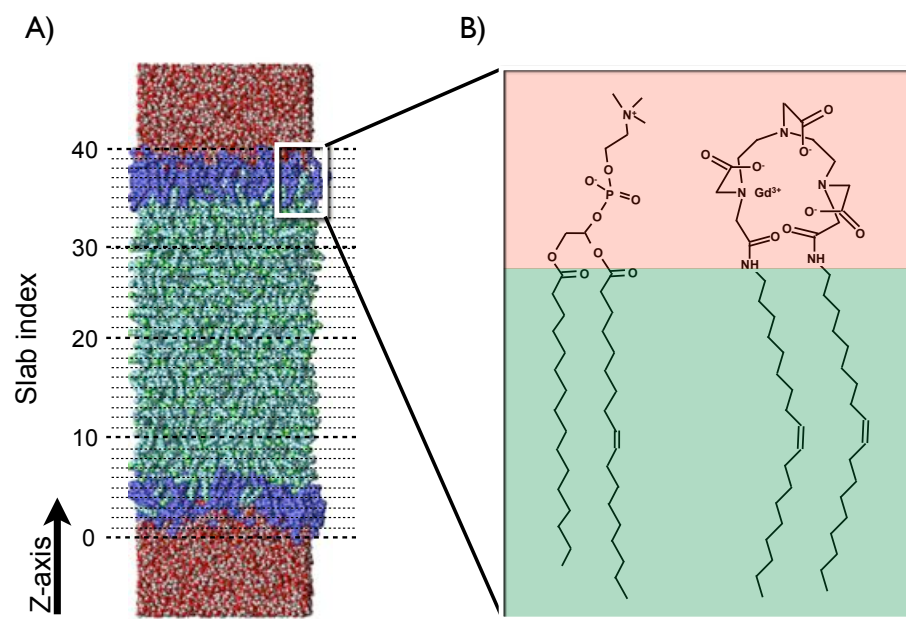
Figure 6.2: Potential position of Gd^{3+} ions on the PFC-NEP surface. A) A modeled PFOB-NEP in a slab-geometry. The POPC monolayers with the head groups oriented toward water regions and with lipid tails oriented toward PFOB region are shown in blue. Water is shown in red and white and PFOB is shown in green. The lower and upper boundaries for the area where PFOB molecules could visit were determined by the mean choline group position of each monolayer. The area was divided into the thin slabs (40) of 0.2 nm in thickness along the z-axis. B) The position of gadolinium diethylene-triamine-pentaacetic acid-bis-oleate (Gd-DTPA-BOA: right) is approximated based on its chemical structure. The position of a palmitoyloleoylphosphatidylcholine (POPC:left) lipid is shown for comparison. Gd^{3+} ions may locate at the depth close to that of phosphate group. The water and PFOB regions are colored in red and green respectively.
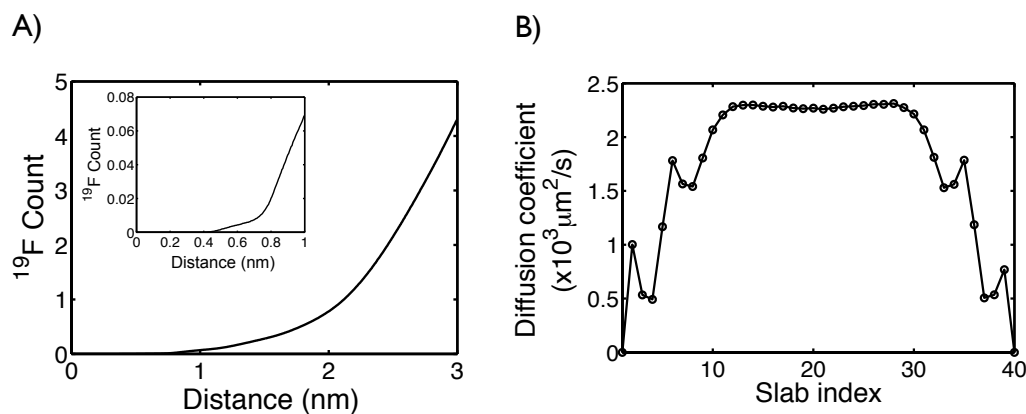
Figure 6.3: Microscopic observation at the PFOB-NEP interface based on atomistic simulations. A) The mean distribution of ^{19}F atoms of PFOB around a phosphate group that models the position of a Gd^{3+} ion. The ^{19}F counts at close distances are enlarged in the inset, which shows that ^{19}F can approach as close as 0.5 nm. B) The one-dimensional diffusion coefficients of PFOB molecules at each slab are plotted along the z-axis.

Based on the lipid dependency of the fusion between two bilayers, we expect that lipids of negative curvature (PE, cholesterol) will facilitate fusion while the lipids of positive curvature (LPC) will hinder the process.(253) Future simulations will be more useful to provide quantitative results, from which more precise formalism can be derived for the lipid compositions.

Chapter 7

Appendix

7.1 Supplementary Materials, Chapter 3

7.1.1 United atom PFOB model develoopment

Figure 7.1: Fitting of RB function to the torsional energy profiles. A single point energy was calculated at every 15 degree after optimization in vacuum. A) $BrCF_2$-CF_2CF_3 B) CF_3CF_2-CF_2CF_3
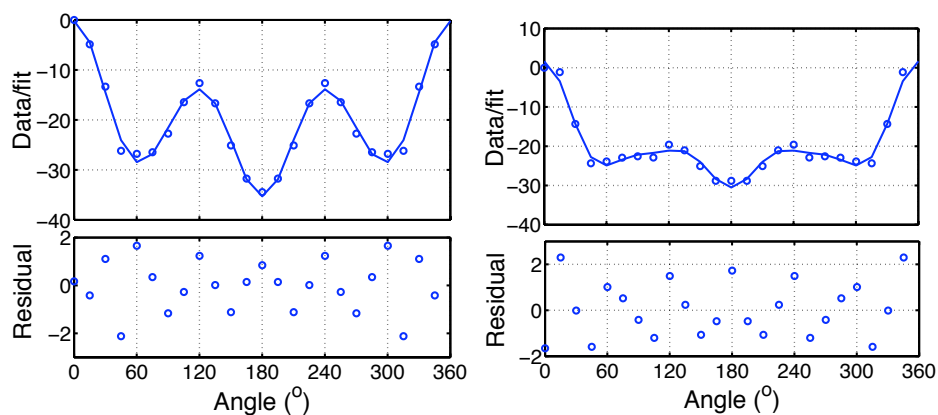
7.1.2   United atom PFOB model testing

Density

The density of liquid PFOB at standard temperature was calculated from an 83 ns NpT simulation of a box containing 216 PFOB molecules. The system reached equilibrium quickly and the mean density and standard error were calculated by the block averaging method described above. The density obtained with our PFOB parameters was 1.891 ± 0.001 kg/L. This result deviated from the experimental measurements of 1.925 ± 0.007 kg/L by less than 2% (21; 19). Our new parameters are an improvement over previous PFOB parameters (181; 182) which gave density errors as large as 7% for relevant perfluorocarbon species.

Heat of vaporization

The heat of vaporization was calculated according to equation 7.1 based on the relation of enthalpy changes (ΔH) to internal energy changes (ΔU) and pressure-volume work ($p\Delta V$) (271):

$$\Delta_{vap}H = E_{\text{intra, gas}} - E_{\text{tot, liq}} + RT. \tag{7.1}$$

The change in internal energy was obtained from the difference of the intramolecular energy of PFOB at the gas phase ($E_{\text{intra, gas}}$) and the total internal energy of PFOB in the liquid phase ($E_{\text{tot, liq}}$). $E_{\text{tot, liq}}$ was obtained from the bulk PFOB simulation described above while $E_{\text{intra, gas}}$ was calculated from a separate simulation of a single PFOB molecule in a box with the same dimensions as used for the density calculation. The last term (RT) was estimated assuming an ideal PFOB gas (with thermal energy RT) and zero pressure-volume work when extracting PFOB from the liquid phase. The experimental heat of vaporization was 42.67 ± 1.276 (kJ/mol) while the result from our simulation was 41.05 ± 0.26 (kJ/mol), for an error of less than 4% (21; 187; 188).

Solvation free energy

PFOB molecules make extensive interactions with lipid tails at the PFOB-water interface. To ensure accurate modeling of this interfacial region, it was important to reproduce the interaction energy of PFOB with lipid tails accurately. Therefore, the desolvation energy of a united perfluoromethane (CF_4) in a box of 421 liquid n-hexanes was estimated using the parameters employed in our PFOB-NEP interface simulations. The calculation was limited to CF_4 due to the lack of experimental data for hexane solvation of other longer-chain perfluorocarbons. The solvation energy was calculated by thermodynamic integration (272)

$$\Delta G_{TI}^0 = \int_0^1 \left\langle \frac{\partial V(\lambda)}{\partial \lambda} \right\rangle_\lambda d\lambda, \tag{7.2}$$

The integration is performed numerically along λ, a generalized coordinate which defines the path from a reference state ($\lambda = 0$) to a state of interest ($\lambda = 1$). In this case, we transition from a reference state, where CF_4 experiences full non-bonded interactions with its surroundings, to the state of interest, where those interactions are turned off. The angular brackets in Eq. 7.2 indicate an ensemble average at a particular λ value with potential value $V(\lambda)$. This potential function was calculated by a linear mixing of the two end-point potential functions. Soft-core potentials were used to remove the singularity for vdW and electrostatic interactions when the non-bonded interactions of the united perfluoromethane were set to zero (272; 92).

Thermodynamic integration was performed with 45 different λ windows (from zero to one in 0.02 or 0.03 increments). Each λ window was equilibrated with energy minimization followed by a 10 ps constant volume and a 10 ps constant pressure simulation. A production simulation at each λ value was carried out for 5 ns in the NpT ensemble, and the last 3 ns of each production run was used to calculate the integrand of Eq. 7.2. The calculated desolvation energy via thermodynamic integration was -2.15 ± 0.03 kJ/mol, which deviates by less than 5% from the experimentally measured solvation free energy of perfluoromethane in liquid n-hexane (2.056 kJ/mol) (189). Simulations using previous parameter sets gave a solvation energy of -0.13 kJ/mol; an error of 93% when compared to the experimental values. Additionally the solvation free energy of all-atom perfluoromethane was also computed in the same way, and

the result was -8.2513 ± 0.0501 kJ/mol. These results support our use of the new united atom perfluorocarbon parameters in simulations of the PFOB-NEP interface in conjunction with the current lipid model.

Phase separation of PFOB in water

The hydrophobicity of PFOB is an important characteristic to be preserved in our force field parameters when simulating PFOB emulsions. To test the hydrophobicity of PFOB, a system of randomly mixed PFOB and water molecules was prepared and simulated in the NpT ensemble under the isotropic pressure coupling. PFOB and water spontaneously separated and generated a sandwich configuration with a slab of PFOB in the middle of the box (see Figure 7.2).

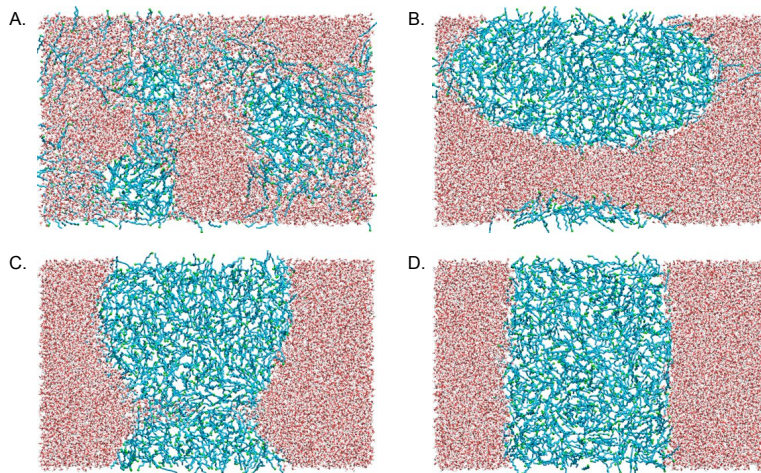Figure 7.2: Spontaneous phase separation of PFOB in water. The snapshots were collected at time 0 ns (A), 1 ns (B), 1.7 ns (C), and 2 ns (D).

The width δ was defined as the distance over which the density of one molecule type changes from 90 % to 10 % of its bulk density at the phase separated interface; this width gets smaller as the de-mixing between the two molecule types is stronger

(273). As shown by the sharp interface in Figure 7.3, the widths δ were 0.36 nm for PFOB and 0.45 nm for water at the pure PFOB/water interface. These widths are comparable to the octane-water interface (approximately 0.3 nm) (273), indicating that our parameters give a strongly hydrophobic PFOB species.

However, the width δ of the PFOB-water interface has not been measured experimentally. Therefore, to make a direct comparison with experimental results, the surface tension at the pure PFOB-water interface was calculated. The local pressure tensor $\mathsf{p}(z)$ was calculated from the difference between kinetic energy and the virial (or configurational stress) tensor in every slab along the surface normal, as described by Lindahl et al. (178) and used by several other authors(274; 275).

$$\mathsf{p}(z) = \sum_{i \in \text{slice}} m_i \mathbf{v}_i \otimes \mathbf{v}_i - \frac{1}{\Delta V} \sum_{j \in \text{system}} \sum_{k < j} \mathbf{F}_{jk} \otimes \mathbf{r}_{jk} f(z, z_j, z_k). \tag{7.3}$$

The first sum is taken over all particles in the slab while all the particle-pairs in the system contribute to the second sum. The function f is used to determine the virial contribution to the slab depending on the positions of two atoms with respect to the current slab: if both atoms are within the slab then $f = 1$, if both are outside on opposite sides then $f = \Delta z/|z_j - z_k|$, and if exactly one of them is inside then $f = \Delta z/2|z_j - z_k|$.

To obtain local pressure tensors, the PFOB-water system was simulated in the NVT ensemble starting from the fully equilibrated phase-separated structure. The simulation parameters were same as those described above except for the use of the NVT ensemble. Structures were sampled at every 2.5 ps and it was rerun by the specialized GROMACS version generously provided by Lindahl and Edholm (178). The SHAKE algorithm was used instead of LINCS to facilitate the extraction of pairwise interactions (178). To obtain the pairwise interactions for vdW and electrostatic interactions, a cutoff scheme was employed with 1.8 nm distance (275; 276). The simulation was performed for 50 ns and the local pressure tensors were calculated along the interface normal at 0.1 nm increments (274).

After the diagonal elements of the local pressure tensor were obtained, local pressure was calculated from the difference between the lateral (p_L) and normal (p_N) pressure
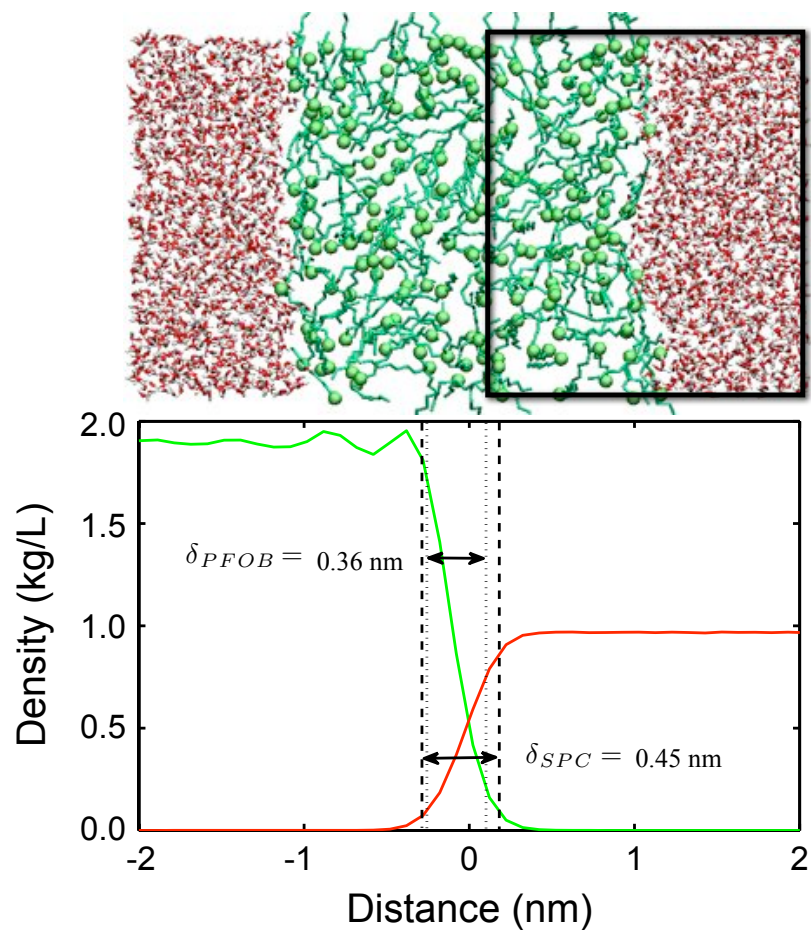
Figure 7.3: Structure at the PFOB-water interface. A snapshot of the phase-separated PFOB in water is shown at the top. Water is drawn by white (oxygen) and red (hydrogen) sticks, and PFOB is drawn by a green ball a nd sticks. The mass density of PFOB is shown in green, and water in red at the bottom. The vertical dotted lines show the width δ of the PFOB interface (δ_{PFOB}), and the vertical dashed lines show the width δ of the water interface (δ_{SPC}). The width δ is 0.36 nm for PFOB interface and that is 0.45 nm for water interface

tensor components:

$$p_{\mathrm{local}}(z) = p_L(z) - p_N(z) = \frac{1}{2}\left(p_{xx}(z) + p_{yy}(z)\right) - p_z(z) \tag{7.4}$$

Figure 7.4: Local pressure profile. The local pressures ($\boldsymbol{P}_{local} = \boldsymbol{P}_L$ - $\boldsymbol{P}_N$) at each slab along the normal of PFOB-water interface as 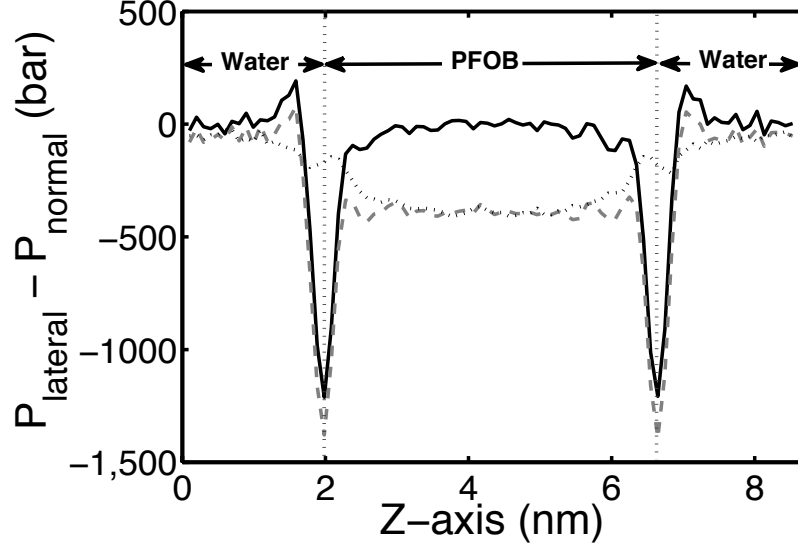are shown in the Figure 7.3. Mean local pressures are shown with a solid black line and standard errors are in solid blue lines. The regions of PFOB and water are designated with the vertical dotted lines to mark the positions of interface.

The negative pressure was the maximum at the interfaces, implying the existence of positive surface tension that the system has a tendency to minimize the interfacial area.

Surface tension, the energy per unit area of the interface, was computed by integrating the negative local pressure profile along the normal axis:

$$\gamma = -\int p_{\mathrm{local}}(z)dz. \tag{7.5}$$

The computed surface tension at the PFOB-water interface was $41.23 \pm 0.91\ mN/m$, which was 80 % of the experimental result of $51.3\ mN/m$ (21). In our study, the NVT simulations were performed with the SETTLE algorithm that fixes the distances between the oxygen and the hydrogen atom and between two hydrogen atoms of water.

It was reported that the orientation of rigid bond along the interface normal increased the deviation of pressure normal at the interface from the bulk value (277), and we could observe bumps at the interfaces between PFOB and water. Therefore, the 20 % discrepancy might have arisen from the limitations of the method as reported in the reference (277) in addition to the imperfect force field.

These tests of our PFOB model show that it reliably reproduces bulk as well as interfacial PFOB properties and can be used to realistically model the PFOB-NEP interface.

7.1.3 PFOB-NEP analysis
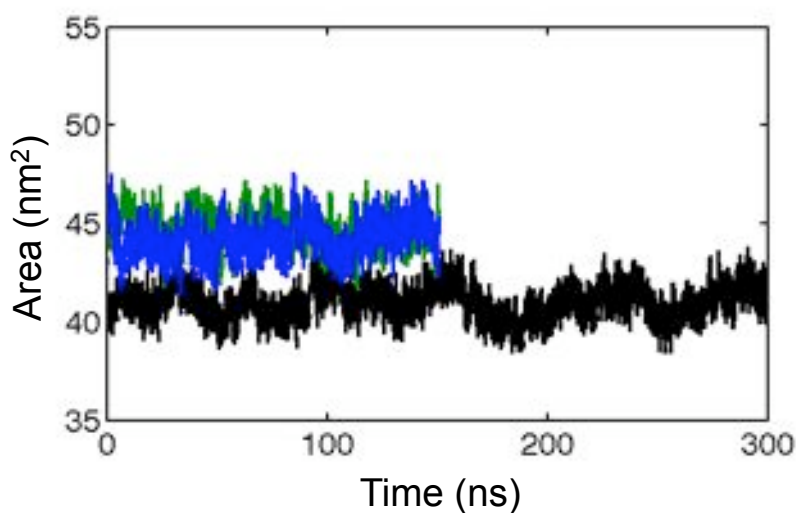
Figure 7.5: Evolution of total cross-sectional area of membranes. The area of PFOB-NEP batch 1 was shown in blue, batch 2 in green and that of the control POPC bilayer in black.
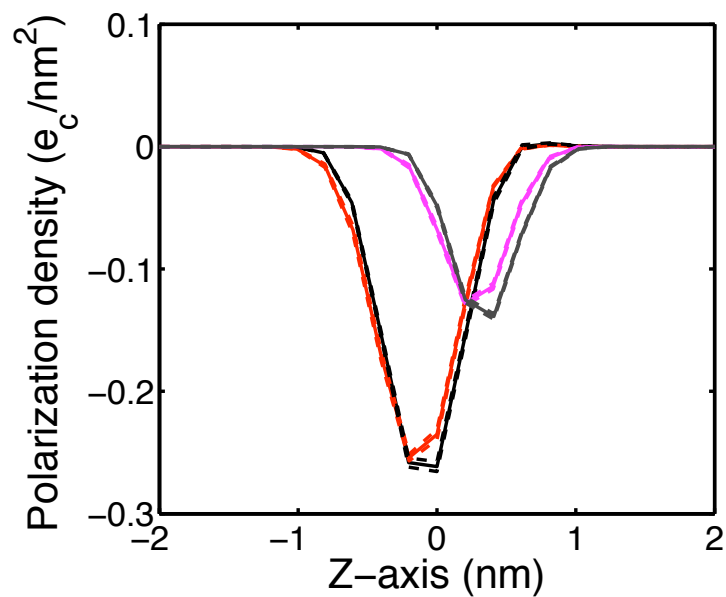
Figure 7.6: Polarization density of the head group. The polarization density of phosphatidyl and choline groups is shown in black for the control POPC bilayer and in red for PFOB-NEP. The polarization density of glycerol group in gray for the control POPC bilayer and in magenta for PFOB-NEP. One standard errors are shown in dashed lines with the same color codes.
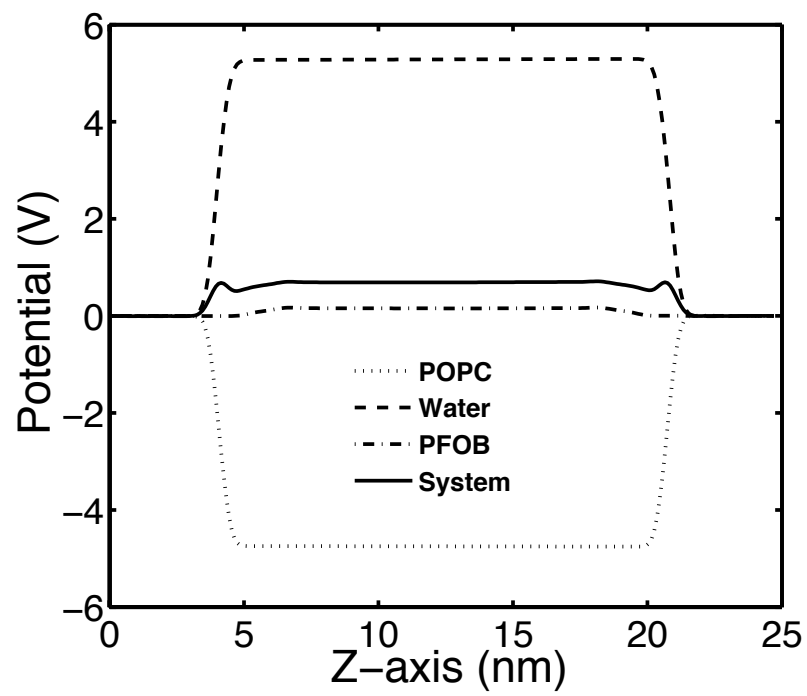
Figure 7.7: Electrostatic potentials by individual components

7.2 Supplementary Materials, Chapter 4
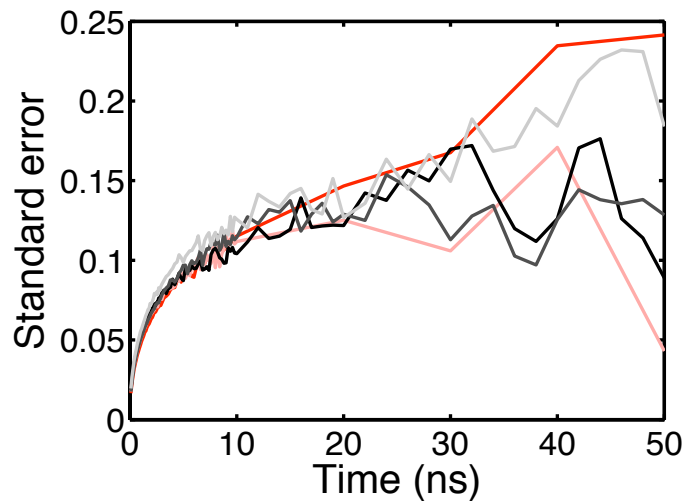
Figure 7.8: Evolution of total membrane area. The standard error for each trajectory for different block sizes (x-axis). The Control (black, dark gray, and light gray) and the PFOB-NEP (red and light red) are plotted for block sizes upto 50 ns.

7.3   Supplementary Materials, Chapter 5
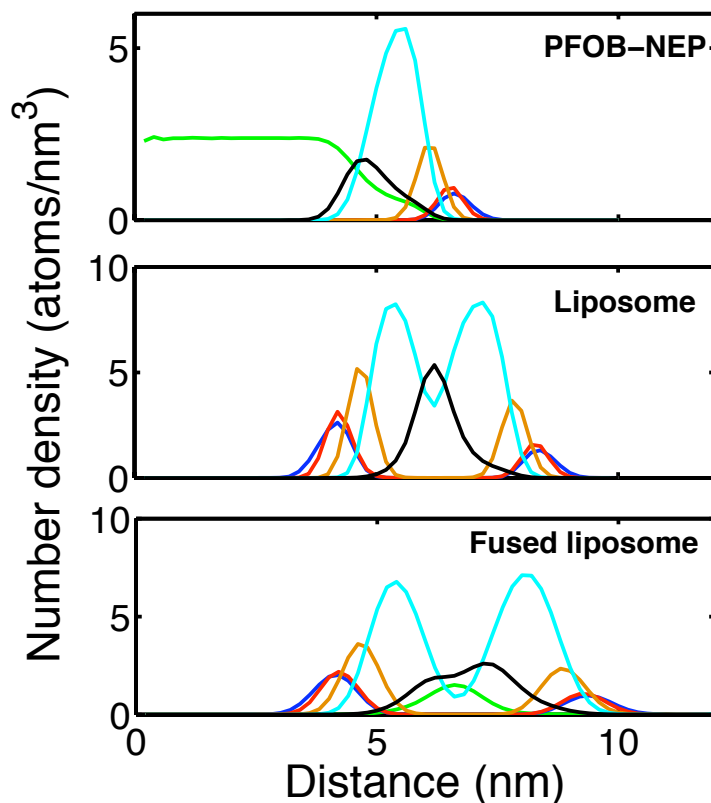
Figure 7.9: Changes in liposome geometry after fusion. The top panel shows the number density of PFOB-NEP, the middle panel the number density of liposome, and the bottom panel the density of fused liposome. The density of PFOB is shown in green, choline group in blue, phosphate group in red, glycerol group in orange, lipid tails in cyan, terminal methyl group in black. The increase is observed in the bilayer thickness of the liposome after the fusion as a result of the absorption of PFOB into the intermonolayer space of the bilayer.
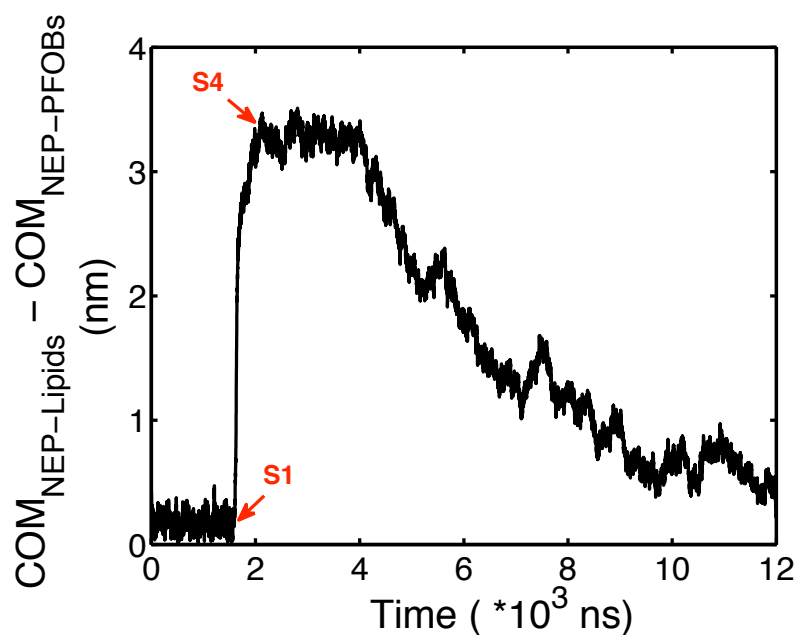
Figure 7.10: Second reaction coordinate. The second reaction coordinate is determined by the distance between the center of mass of PFOBs and the lipids forming the emulsifying layer on the PFOB-NEP surface. The distance increases rapidly when the fusion begins but then decays slowly and does not go back to zero for a long time. This reaction coordinate is useful to measure the mixing of the lipids from PFOB-NEP with the lipids of the outer monolayer of the fused liposome. Our fusion simulations showed that it took substantial time to observe complete mixing of the two lipids groups. This particular case (L2-N2-3) shows that 1 μs was not enough for complete mixing. The two arrows designate the initiation state (S1) and the state of 75% decrease (S4) respectively.
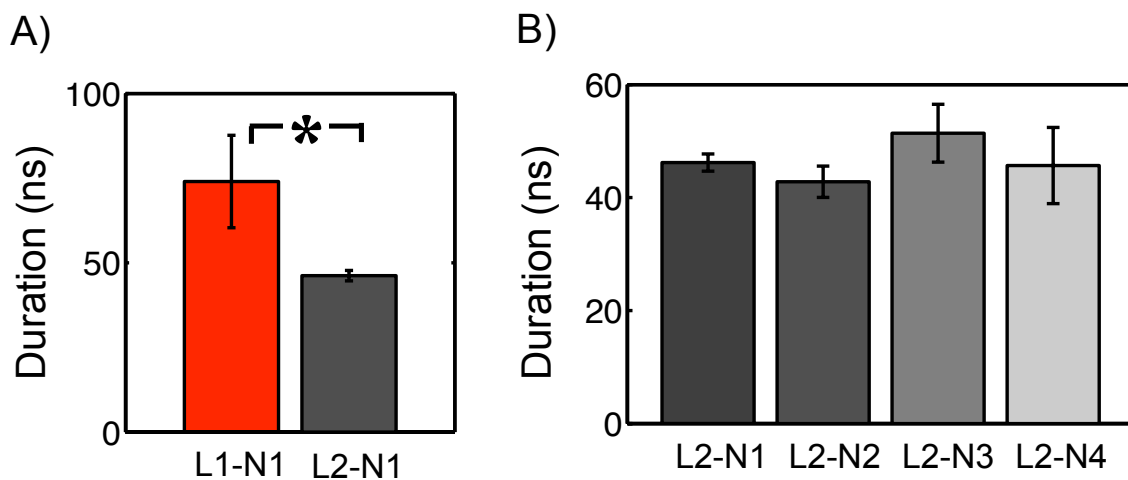
Figure 7.11: Time required to reach 75 % reduction (S4 state) from the beginnig (S1 state) in the R_{CM}. A) The time required to reach S4 was significantly different between L1-N1 and L2-N1 pairs at a 95% confidence level.B) The time required to reach S4 was indistinguishable among fusion pairs varying POPE proportions.
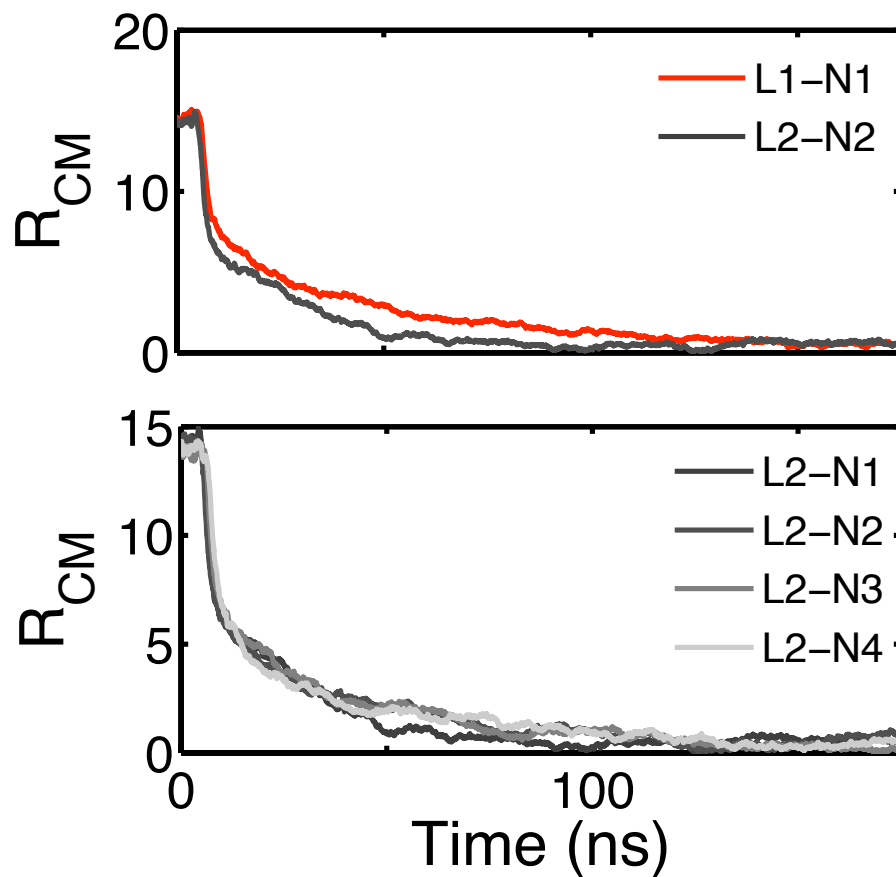
Figure 7.12: Superimposed reaction coordinates. Top panel: the reaction coordinates of L1-N1 (red), L2-N1 (dark gray). Bottom panel: the reaction coordinates of L2-N1-1, L2-N2-1, L2-N3-1, L2-N4-1 with the color codes shown in the panel. All reaction coordinates are plotted beginning at 50 ns prior to the S1 state. Only marginal differences are detected among them after superimposition, implying that the next steps after initial membrane disruption occurred at indistinguishable rates.

References

[1] Anne H. Schmieder, Patrick M. Winter, Shelton D. Caruthers, Thomas D. Harris, Todd A. Williams, John S. Allen, Elizabeth K. Lacy, Huiying Zhang, Michael J. Scott, Grace Hu, J. David Robertson, Samuel A. Wickline, and Gregory M. Lanza. *Magn. Reson. Med.*, **53**(3), 621–627, 2005.

[2] Patrick M. Winter, Anne H. Schmieder, Shelton D. Caruthers, Jeffery L. Keene, Huiying Zhang, Samuel A. Wickline, and Gregory M. Lanza. *The FASEB Journal*, **22**(8), 2758–2767, 2008.

[3] Walter J. Akers, Zongren Zhang, Mikhail Berezin, Yunpeng Ye, Anthony Agee, Kevin Guo, Ralph W. Fuhrhop, Samuel A. Wickline, Gregory M. Lanza, and Samuel Achilefu. *Nanomedicine*, **5**(5), 715–726, 2010.

[4] Patrick M. Winter, Shelton D. Caruthers, Andrea Kassner, Thomas D. Harris, Lori K. Chinen, John S. Allen, Elizabeth K. Lacy, Huiying Zhang, J. David Robertson, Samuel A. Wickline, and Gregory M. Lanza. *Cancer Res.*, **63**(18), 5838–5843, 2003.

[5] Patrick M. Winter, Anne M. Neubauer, Shelton D. Caruthers, Thomas D. Harris, J. David Robertson, Todd A. Williams, Anne H. Schmieder, Grace Hu, John S. Allen, Elizabeth K. Lacy, Huiying Zhang, Samuel A. Wickline, and Gregory M. Lanza. *Arterioscler. Thromb. Vasc. Biol.*, **26**(9), 2103–2109, 2006.

[6] Patrick M. Winter, Shelton D. Caruthers, Huiying Zhang, Todd A. Williams, Samuel A. Wickline, and Gregory M. Lanza. *JACC. Cardiovascular imaging*, **1**(5), 624–634, 2008.

[7] P. M. Winter, S. D. Caruthers, J. S. Allen, K. Cai, T. A. Williams, G. M. Lanza, and S. A. Wickline. *Magn. Reson. Med.*, **64**(2), 369–376, 2010.

[8] Gregory Lanza, Shelton Caruthers, Patrick Winter, Michael Hughes, Anne Schmieder, Grace Hu, and Samuel Wickline. *European Journal of Nuclear Medicine and Molecular Imaging*, **37**(0), 114–126–126, 2010.

[9] Eric T. Ahrens, Rafael Flores, Hongyan Xu, and Penelope A. Morel. *Nature Biotechnology*, **23**(8), 983–987, 2005.

[10] Kathryn C. Partlow, Junjie Chen, Jason A. Brant, Anne M. Neubauer, Todd E. Meyerrose, Michael H. Creer, Jan A. Nolta, Shelton D. Caruthers, Gregory M. Lanza, and Samuel A. Wickline. *FASEB J.*, **21**(8), 1647–1654, 2007.

[11] Neelesh R. Soman, Steven L. Baldwin, Grace Hu, Jon N. Marsh, Gregory M. Lanza, John E. Heuser, Jeffrey M. Arbeit, Samuel A. Wickline, and Paul H. Schlesinger. *J. Clin. Invest.*, **119**(9), 2830–2842, 2009.

[12] Jon N. Marsh, Angana Senpan, Grace Hu, Mike J. Scott, Patrick J. Gaffney, Samuel A. Wickline, and Gregory M. Lanza. *Nanomedicine-UK*, **2**(4), 533–543, 2007.

[13] Megan Kaneda, Shelton Caruthers, Gregory Lanza, and Samuel Wickline. *Ann. Biomed. Eng.*, **37**(10), 1922–1933, 2009.

[14] Anne M. Morawski, Patrick M. Winter, Xin Yu, Ralph W. Fuhrhop, Michael J. Scott, Franklin Hockett, David D. Robertson, Patrick J. Gaffney, Gregory M. Lanza, and Samuel A. Wickline. *Magnet. Reson. Med.*, **52**(6), 1255–1262, 2004.

[15] Thomas Chang. in *Artificial Oxygen Carrier: Its Front Line*, K. Kobayashi, E. Tsuchida, and H. Horinouchi, editors, (Springer, Tokyo, Japan). volume 12. chapter 2, pages 22–33. 2005.

[16] Robert F. Mattrey, F. William Scheible, Barbara B. Gosink, George R. Leopold, David M. Long, and Charles B. Higgins. *Radiology*, **145**(3), 759–762, 1982.

[17] Robert F. Mattrey. *Am. J. Roentgenol.*, **152**(2), 247–252, 1989.

[18] Robert F. Mattrey and David M. Long. *Invest. Radiol.*, **23 (Suppl. 1)**, S298–S301, 1988.

[19] Michael André, Thomas Nelson, and Robert Mattrey. *Invest. Radiol.*, **25**(9), 983–987, 1990.

[20] I. Kuznetsova and V. Yurchenko. *Pharmaceutical Chemistry Journal*, **40**(12), 673–677, 2006.

[21] Jean G. Riess. *Chem. Rev.*, **101**(9), 2797–2920, 2001.

[22] P. E. Keipert. in *Blood substitutes: principles, methods, products and clinical trials*, T. M. S. Chang, editor, (S. Karger AG, Basel, Switzerland). pages 127–156. 1998.

[23] Evan C. Unger, Thomas Porterc, William Culpd, Rachel Labella, Terry Matsunagaa, and Reena Zutshi. *Advanced Drug Delivery Reviews*, **56**(9), 1291–1314, 2004.

[24] G. V. Jeffreys and G. A. Davies. *RECENT ADVANCES IN LIQUID–LIQUID EXTRACTION.* Pergamon, 1971.

[25] C. Washington. *Advanced Drug Delivery Reviews*, **20**(2-3), 131–145, 1996.

[26] Si-shen Feng and Guofeng Huang. *Journal of Controlled Release*, **71**(1), 53–69, 2001.

[27] P. E. Keipert, S. Otto, S. F. Flaim, J. G. Weers, E. A. Schutt, T. J. Pelura, D. H. Klein, and T. L. Yaksh. *Artificial Cells, Blood Substitutes, and Biotechnology*, **22**(4), 1169–1174, 1994.

[28] Luz Palacios and Tong Wang. *Journal of the American Oil Chemists' Society*, **82**(8), 565–569, 2005.

[29] Gregory M. Lanza and Samuel A. Wickline. *Progress in Cardiovascular Diseases*, **44**(1), 13–31, 2001.

[30] A. Morawski, G. Lanza, and S. Wickline. *Current Opinion in Biotechnology*, **16**(1), 89–92, 2005.

[31] R. Jahn. *Current Opinion in Cell Biology*, **14**(4), 488–495, 2002.

[32] Yechiel Shai. *Biochimca et Biophysica Acta*, **1462**, 55–70, 1999.

[33] Kim A. Brogden. *Nature Reviews Microbiology*, **3**(3), 238–250, 2005.

[34] H. Huang. *Biochimica et Biophysica Acta (BBA) - Biomembranes*, **1758**(9), 1292–1302, 2006.

[35] Neelesh R. Soman, Gregory M. Lanza, John M. Heuser, Paul H. Schlesinger, and Samuel A. Wickline. *Nano Lett.*, **8**(4), 1131–1136, 2008.

[36] Hervé Hillaireau and Patrick Couvreur. *Cellular and Molecular Life Sciences*, **66**(17), 2873–2896, 2009.

[37] Johanna Rinne, Brian Albarran, Juulia Jylhava, Teemu Ihalainen, Pasi Kankaanpaa, Vesa Hytonen, Patrick Stayton, Markku Kulomaa, and Maija V. Ranta. *BMC Biotechnology*, **7**(1), 1+, 2007.

[38] A. Kerkis, M. A. F. Hayashi, T. Yamane, and I. Kerkis. *IUBMB Life*, **58**(1), 7–13, 2006.

[39] Zhengzheng Fei, Shengnian Wang, Yubing Xie, Brian E. Henslee, Chee G. Koh, and L. James Lee. *Analytical Chemistry*, **79**(15), 5719–5722, 2007.

[40] Cristian Ionescu-Zanetti, Andrew Blatz, and Michelle Khine. *Biomedical Microdevices*, **10**(1), 113–116–116, 2008.

[41] Héctor R. Guzmán, Daniel X. Nguyen, Sohail Khan, and Mark R. Prausnitz. *The Journal of the Acoustical Society of America*, **110**(1), 588–596, 2001.

[42] Yoshiaki Taniyama, Katsuro Tachibana, Kazuya Hiraoka, Tsunetatsu Namba, Keita Yamasaki, Naotaka Hashiya, Motokuni Aoki, Toshio Ogihara, Kaneda Yasufumi, and Ryuichi Morishita. *Circulation*, **10**, 1233–1239, 2002.

[43] Steven B. Feinstein. *Am J Physiol Heart Circ Physiol*, **287**(2), H450–457, 2004.

[44] N. R. Soman, J. N. Marsh, M. S. Hughes, G. M. Lanza, and S. A. Wickline. *IEEE Transactions on Nanobioscience*, **5**(2), 69–75, 2006.

[45] D. L. Miller and J. Quddus. *Proceedings of the National Academy of Sciences of the United States of America*, **97**(18), 10179–10184, 2000.

[46] J. Wible. *Ultrasound in Medicine & Biology*, **28**(11-12), 1535–1546, 2002.

[47] Kathryn C. Partlow, Gregory M. Lanza, and Samuel A. Wickline. *Biomaterials*, **29**(23), 3367–3375, August 2008.

[48] Gregory M. Lanza, Xin Yu, Patrick M. Winter, Dana R. Abendschein, Kerry K. Karukstis, Michael J. Scott, Lori K. Chinen, Ralph W. Fuhrhop, David E. Scherrer, and Samuel A. Wickline. *Circulation*, **106**(22), 2842–2847, 2002.

[49] D. Siegel. *Biophysical Journal*, **65**(5), 2124–2140, 1993.

[50] L. Chernomordik, A. Chanturiya, J. Green, and J. Zimmerberg. *Biophysical Journal*, **69**(3), 922–929, 1995.

[51] M. Müller, K. Katsov, and M. Schick. *Biophysical Journal*, **85**(3), 1611–1623, 2003.

[52] Alexandr Chanturiya, Leonid V. Chernomordik, and Joshua Zimmerberg. *Proceedings of the National Academy of Sciences of the United States of America*, **94**(26), 14423–14428, 1997.

[53] L. Yang and H. Huang. *Biophysical Journal*, **84**(3), 1808–1817, 2003.

[54] Siewert J. Marrink and Alan E. Mark. *Journal of the American Chemical Society*, **125**(37), 11144–11145, 2003.

[55] Peter M. Kasson, Erik Lindahl, and Vijay S. Pande. *PLoS computational biology*, **6**(6), e1000829+, 2010.

[56] A. F. Smeijers, A. J. Markvoort, K. Pieterse, and P. A. J. Hilbers. *The Journal of Physical Chemistry B*, **110**(26), 13212–13219, 2006.

[57] J. A. McCammon, B. R. Gelin, and M. Karplus. *Nature*, **267**(5612), 585–590, 1977.

[58] Andrew Leach. *Molecular Modelling: Principles and Applications (2nd Edition)*. Prentice Hall, 2 edition, 2001.

[59] Martin Karplus and J. Andrew McCammon. *Nature structural biology*, **9**(9), 646–652, 2002.

[60] B. R. Brooks, R. E. Bruccoleri, B. D. Olafson, D. J. States, S. Swaminathan, and M. Karplus. *J. Comput. Chem.*, **4**(2), 187–217, 1983.

[61] P. K. Weiner and P. A. Kollman. *J. Comput. Chem.*, **2**(3), 287–303, 1981.

[62] Walter R. P. Scott, Philippe H. Hunenberger, Ilario G. Tironi, Alan E. Mark, Salomon R. Billeter, Jens Fennen, Andrew E. Torda, Thomas Huber, Peter Kruger, and Wilfred F. van Gunsteren. *The Journal of Physical Chemistry A*, **103**(19), 3596–3607, 1999.

[63] Pengyu Ren and Jay W. Ponder. *Journal Physical Chemistry B*, **107**, 5933–5947, 2003.

[64] Jeffery B. Klauda, Norbert Kučerka, Brooks Brooks, Richard W. Pastor, and John F. Nagle. *Biophys. J.*, **90**(8), 2796–2807, 2006.

[65] Siewert J. Marrink, Alex H. de Vries, and Peter P. Tieleman. *Biochimica et Biophysica Acta*, **1788**(1), 149–168, 2009.

[66] D. Peter Tieleman, Hari Leontiadou, Alan E. Mark, and Siewert-Jan Marrink. *Journal of the American Chemical Society*, **125**(21), 6382–6383, 2003.

[67] Hari Leontiadou, Alan E. Mark, and Siewert J. Marrink. *Journal of the American Chemical Society*, **128**(37), 12156–12161, 2006.

[68] Henry D. Herce and Angel E. Garcia. *Proceedings of the National Academy of Sciences*, **104**(52), 20805–20810, 2007.

[69] Siewert J. Marrink, Erik Lindahl, Olle Edholm, and Alan E. Mark. *Journal of the American Chemical Society*, **123**(35), 8638–8639, 2001.

[70] Alex H. de Vries, Alan E. Mark, and Siewert J. Marrink. *The Journal of Physical Chemistry B*, **108**(7), 2454–2463, 2004.

[71] Peter M. Kasson, Nicholas W. Kelley, Nina Singhal, Marija Vrljic, Axel T. Brunger, and Vijay S. Pande. *P. Natl. Acad. Sci. USA.*, **103**(32), 11916–11921, 2006.

[72] Peter M. Kasson and Vijay S. Pande. *PLoS Comput. Biol.*, **3**(11), 2228–2238, 2007.

[73] Klaus Gawrisch. in *The Structure of biological membranes*, Philip L. Yeagle, editor, (CRC Press, Boca Raton, Florida). chapter 4, pages 149+. 2005.

[74] J. Klauda, R. Venable, A. MacKerelljr, and R. Pastor. (Elsevier,). volume 60 of *Current Topics in Membranes*. pages 1–48. 2008.

[75] Marcus G. Martin and J. Ilja Siepmann. *The Journal of Physical Chemistry B*, **102**(14), 2569–2577, 1998.

[76] Oliver Berger, Olle Edholm, and Fritz Jähnig. *Biophys. J.*, **72**(5), 2002–2013, 1997.

[77] D. Peter Tieleman, Justin L. MacCallum, Walter L. Ash, Christian Kandt, Zhitao Xu, and Luca Monticelli. *J. Phys.:Condens. Matter*, **18**(28), S1221–S1234, 2006.

[78] Sun-Joo Lee, Yuhua Song, and Nathan A. Baker. *Biophysical journal*, **94**(9), 3565–3576, 2008.

[79] Brett N. Olsen, Paul H. Schlesinger, and Nathan A. Baker. *J. Am. Chem. Soc.*, **131**(13), 4854–4865, 2009.

[80] Jonathan N. Sachs, Hirsh Nanda, Horia I. Petrache, and Thomas B. Woolf. *Biophys. J.*, **86**(6), 3772–3782, June 2004.

[81] Yuhua Song, Victor Guallar, and Nathan A. Baker. *Biochemistry*, **44**(41), 13425–13438, October 2005.

[82] Nilmadhab Chakrabarti, Chris Neale, Jian Payandeh, Emil F. Pai, and Régis Pomès. *Biophys. J.*, **98**(5), 784–792, 2010.

[83] Rüdiger Goetz and Reinhard Lipowsky. *Journal of Chemical Physics*, **108**, 7397+, 1998.

[84] Mark J. Stevens. *The Journal of Chemical Physics*, **121**(23), 11942–11948, 2004.

[85] Siewert J. Marrink, Alex H. de Vries, and Alan E. Mark. *J. Phys. Chem. B*, **108**(2), 750–760, 2004.

[86] John C. Shelley, Mee Y. Shelley, Robert C. Reeder, Sanjoy Bandyopadhyay, and Michael L. Klein. *The Journal of Physical Chemistry B*, **105**(19), 4464–4470, 2001.

[87] Sergei Izvekov and Gregory A. Voth. *The Journal of Physical Chemistry B*, **109**(7), 2469–2473, 2005.

[88] Siewert J. Marrink, Jelger J. Risselada, Serge Yefimov, Peter P. Tieleman, and Alex H. de Vries. *J. Phys. Chem. B*, **111**(27), 7812–7824, 2007.

[89] Luca Monticelli, Senthil K. Kandasamy, Xavier Periole, Ronald G. Larson, D. Peter Tieleman, and Siewert-Jan Marrink. *Journal of Chemical Theory and Computation*, **4**(5), 819–834, 2008.

[90] Siewert J. Marrink and Alan E. Mark. *Journal of the American Chemical Society*, **125**(49), 15233–15242, 2003.

[91] C. Oostenbrink, A. Villa, A. E. Mark, and W. F. Van Gunsteren. *Journal of computational chemistry*, **25**(13), 1656–1676, 2004.

[92] Berk Hess, Carsten Kutzner, David van der Spoel, and Erik Lindahl. *J. Chem. Theory Comput.*, **4**(3), 435–447, 2008.

[93] Siewert-Jan Marrink and Alan E. Mark. *Biophysical Journal*, **87**(6), 3894–3900, 2004.

[94] H. Jelger Risselada and Siewert J. Marrink. *Proceedings of the National Academy of Sciences*, **105**(45), 17367–17372, 2008.

[95] S. A. Shkulipa, W. K. den Otter, and W. J. Briels. *Physical Review Letters*, **96**(17), 178302+, 2006.

[96] H. Binder and Zschörnig. *Chemistry and Physics of Lipids*, **115**(1-2), 39–61, 2002.

[97] R. A. Böckmann, A. Hac, T. Heimburg, and H. Grubmüller. *Biophysical Journal*, **85**(3), 1647–55, 2003.

[98] P. Garidel and A. Blume. *Langmuir*, **15**(17), 5526–34, 1999.

[99] Georg Pabst, Aden Hodzic, Janez Strancar, Sabine Danner, Michael Rappolt, and Peter Laggner. *Biophysical Journal*, **93**(8), 2688–2696, 2007.

[100] S. Ohki and K. Arnold. *Journal of Membrane Biology*, **114**(3), 195–203, 1990.

[101] J. C. Franklin and D. S. Cafiso. *Biophysical Journal*, **65**(1), 289–99, 1993.

[102] V. C. K. Chiu, D. Mouring, B. D. Watson, and D. H. Haynes. *Journal of Membrane Biology*, **56**(2), 121–32, 1980.

[103] S. Garcia-Manyes, G. Oncins, and F. Sanz. *Biophysical Journal*, **89**(3), 1812–26, 2005.

[104] T. Fukuma, M. J. Higgins, and S. P. Jarvis. *Physical Review Letters*, **98**, 106101, 2007.

[105] H. Binder, K. Arnold, A. S. Ulrich, and O. Zschörnig. *Biophysical Chemistry*, **90**(1), 57–74, 2001.

[106] Y. A. Ermakov. *Biochimica et Biophysica Acta*, **1023**(1), 91–7, 1990.

[107] M. J. Bedzyk, G. M. Bommarito, M. Caffrey, and T. L. Penner. *Science*, **248**(4951), 52–6, 1990.

[108] P. L. Yeagle. *Accounts of Chemical Research*, **11**(9), 321–7, 1978.

[109] I. Gambu and B. Roux. *Journal of Physical Chemistry B*, **101**(31), 6066–72, 1997.

[110] A. A. Gurtovenko. *Journal of Chemical Physics*, **122**(24), 244902, 2005.

[111] J. N. Sachs, P. S. Crozier, and T. B. Woolf. *Journal of Chemical Physics*, **121**(22), 10847–51, 2004.

[112] P. T. Vernier, M. J. Ziegler, Y. Sun, M. A. Gundersen, and D. P. Tieleman. *Physical Biology*, **3**(4), 233–47, 2006.

[113] J. N. Sachs, H. Nanda, H. I. Petrache, and T. B. Woolf. *Biophysical Journal*, **86**(6), 3772–82, 2004.

[114] A. A. Gurtovenko and I. Vattulainen. *Biophysical Journal*, **92**(6), 1878–90, 2007.

[115] Y. Song, V. Guallar, and N. A. Baker. *Biochemistry*, **44**(41), 13425–38, 2005.

[116] D. Van der Spoel, E. Lindahl, B. Hess, G. Groenhof, A. E. Mark, and H. J. C. Berendsen. *Journal of Computational Chemistry*, **26**(16), 1701–18, 2005.

[117] O. Berger, O. Edholm, and F. Jahnig. *Biophysical Journal*, **72**(5), 2002–13, 1997.

[118] H. J. C. Berendsen, J. R. Grigera, and T. P. Straatsma. *Journal of Physical Chemistry*, **91**(24), 6269–71, 1987.

[119] T. P. Straatsma and H. J. C. Berendsen. *Journal of Chemical Physics*, **89**(9), 5876–86, 1988.

[120] A. H. de Vries, A. E. Mark, and S. J. Marrink. *Journal of the American Chemical Society*, **126**(14), 4488–4489, 2004.

[121] E. Lindahl and O. Edholm. *Biophysical Journal*, **79**(1), 426–433, 2000.

[122] T. Darden, D. York, and L. G. Pedersen. *Journal of Chemical Physics*, **98**(12), 10089–92, 1993.

[123] M. Parrinello and A. Rahman. *Journal of Applied Physics*, **52**(12), 7182–90, 1981.

[124] W. G. Hoover. *Physical Review A*, **31**(3), 1695–97, 1985.

[125] J. P. Ryckaert, G. Ciccotti, and H. J. C. Berendsen. *Journal of Computational Physics*, **23**(3), 327–341, 1977.

[126] M. P. Allen and D. J. Tildesley. *Computer Simulation of Liquids.* Clarendon, Oxford, 1987.

[127] A. A. Chen and R. V. Pappu. *Journal of Physical Chemistry B*, **111**(23), 6469–78, 2007.

[128] B. Efron and R. J. Tibshirani. *An introduction to the bootstrap.* CRC Press LLC, Boca Raton, FL, 1998.

[129] R. A. Böckmann and H. Grubmüller. *Angewandte Chemie International Edition*, **43**(8), 1021–4, 2004.

[130] C. Anézo, A. H. de Vries, H. D. Höltje, D. P. Tieleman, and S. J. Marrink. *Journal of Physical Chemistry B*, **107**(35), 9424–33, 2003.

[131] J. F. Nagle and S. Tristram-Nagle. *Biochimica et Biophysica Acta (BBA) - Reviews on Biomembranes*, **1469**(3), 159–95, 2000.

[132] S. A. Pandit, D. Bostick, and M. L. Berkowitz. *Biophysical Journal*, **84**(6), 3743–50, 2003.

[133] A. Seelig and J. Seelig. *Biochemistry*, **13**(23), 4839–45, 1974.

[134] D. P. Tieleman, S. J. Marrink, and H. J. C. Berendsen. *Biochimica et Biophysica Acta (BBA) - Reviews on Biomembranes*, **1331**(3), 235–70, 1997.

[135] Y. N. Vorobjev and J. Hermans. *Journal of Physical Chemistry B*, **103**(46), 10234–42, 1999.

[136] E. Isaacson and H. B. Keller. *Analysis of numerical methods.* Dover Publications, Inc., Mineola, N. Y., 1966.

[137] J. AAqvist. *Journal of Physical Chemistry*, **94**(21), 8021–4, 1990.

[138] B. Roux. *Biophysical Journal*, **71**(6), 3177–85, 1996.

[139] M. Rappolt, G. Pabst, H. Amenitsch, and P. Laggner. *Colloids and Surfaces A*, **183-5**, 171–81, 2001.

[140] R. Sano, S. M. Masum, T. Tanaka, Y. Yamashita, V. Levadny, and M. Yamakazi. *Journal of Physics: Condensed Matter*, **17**(31), S2979–89, 2005.

[141] S. Mitaku and S. Aruga. *Biorheology*, **19**(1/2), 185–96, 1982.

[142] J. Israelachvili. *Intermolecular and surface forces.* Academic Press, San Diego, CA, 1992.

[143] H. I. Petrache, N. Gouliaev, S. Tristram-Nagle, R. Zhang, R. M. Suter, and J. F. Nagle. *Physical Review E*, **57**(6), 7014–24, 1998.

[144] J. P. Hansen and I. R. McDonald. *Theory of Simple Liquids*, volume 2. Academic Press, San Diego, CA, 2000.

[145] J. F. Nagle and M. C. Wiener. *Biochimica et Biophysica Acta*, **942**(1), 1–10, 1988.

[146] P. Mukhopadhyay, L. Monticelli, and D. P. Tieleman. *Biophysical Journal*, **86**(3), 1601–1609, 2004.

[147] S. Mabrey, P. L. Mateo, and J. M. Sturtevant. *Biochemistry*, **17**(12), 2464–68, 1978.

[148] H. Leontiadou, A. E. Mark, and S. J. Marrink. *Biophysical Journal*, **92**(12), 4209–15, 2007.

[149] C. E. Capener, I. H. Shrivastava, K. M. Ranatunga, L. R. Forrest, G. R. Smith, and M. S. P. Sansom. *Biophysical Journal*, **78**(6), 2929–42, 2000.

[150] Toby W. Allen, Olaf S. Andersen, and Benoit Roux. *Biophysical Chemistry*, **124**(3), 251–267, 2006.

[151] I. Chandrasekhar, M. Kastenholz, R. D. Lins, C. Oostenbrink, L. D. Schuler, D. P. Tieleman, and W. F. Van Gunsteren. *European Biophysics Journal*, **32**(1), 67–77, 2003.

[152] H. Heller, M. Schaefer, and K. Schulten. *Journal of Physical Chemistry*, **97**(31), 8343–60, 1993.

[153] C. E. Capener and M. S. P. Sansom. *Journal of Physical Chemistry B*, **106**(17), 4543–51, 2002.

[154] J. D. Faraldo-Gómez, G. R. Smith, and M. S. P. Sansom. *European Biophysics Journal*, **31**(3), 217–27, 2002.

[155] J. J. López Cascales, T. F. Otero, B. D. Smith, C. González, and M. Márquez. *Journal of Physical Chemistry B*, **110**(5), 2358–63, 2006.

[156] S. W. Chiu, M. Clark, V. Balaji, S. Subramaniam, H. L. Scott, and E. Jakobsson. *Biophysical Journal*, **69**(4), 1230–45, 1995.

[157] A. Warshel, M. Kato, and A. V. Pisliakov. *Journal of Chemical Theory and Computation*, in press.

[158] T. W. Allen, O. S. Andersen, and B. Roux. *Biophysical Journal*, **90**(10), 3447–68, 2006.

[159] A. Grossfield, P. Ren, and J. W. Ponder. *Journal of the American Chemical Society*, **125**(50), 15671–15682, 2003.

[160] J. W. Ponder and D. A. Case. *Advances in Protein Chemistry*, **66**, 27–85, 2003.

[161] T. Bastug and S. Kuyucak. *European Biophysics Journal*, **34**(5), 377–82, 2005.

[162] A. A. Gurtovenko and I. Vattulainen. *Journal of the American Chemical Society*, **129**(17), 5358–9, 2007.

[163] Volker Wagner, Anwyn Dullaart, Anne-Katrin Bock, and Axel Zweck. *Nat. Biotechnol.*, **24**(10), 1211–1217, 2006.

[164] Kumaresh S. Soppimath, Tejraj M. Aminabhavi, Anandrao R. Kulkarni, and Walter E. Rudzinski. *J. Control. Release*, **70**(1-2), 1–20, 2001.

[165] I. Chen Wang, Lin A. Tai, Don D. Lee, P. P. Kanakamma, Clifton K. F. Shen, Tien-Yau Luh, Chien H. Cheng, and Kuo C. Hwang. *J. Med. Chem.*, **42**(22), 4614–4620, 1999.

[166] Pallab Pradhan, Jyotsnendu Giri, Gopal Samanta, Haladhar D. Sarma, Kaushala P. Mishra, Jayesh Bellare, Rinti Banerjee, and Dhirendra Bahadur. *J. Biomed. Mater. Res. B*, **81B**(1), 12–22, 2007.

[167] Patrick M. Winter, Anne M. Morawski, Shelton D. Caruthers, Ralph W. Fuhrhop, Huiying Zhang, Todd A. Williams, John S. Allen, Elizabeth K. Lacy, David D. Robertson, Gregory M. Lanza, and Samuel A. Wickline. *Circulation*, **108**(18), 2270–2274, 2003.

[168] Samira Bührer-Sékula, Henk L. Smits, George C. Gussenhoven, J. van Leeuwen, S. Amador, Tsuyoshi T. Fujiwara, Paul R. Klatser, and Linda Oskam. *J. Clin. Microbiol.*, **41**(5), 1991–1995, 2003.

[169] Kyung M. Woo, Ji-Hae Jun, Victor J. Chen, Jihye Seo, Jeong-Hwa Baek, Hyunmo Ryoo, Gwan-Shik Kim, Martha J. Somerman, and Peter X. Ma. *Biomaterials*, **28**(2), 335–343, 2007.

[170] James D. Weiland, Wentai Liu, and Mark S. Humayun. *Annu. Rev. Biomed. Eng.*, **7**(1), 361–401, 2005.

[171] Shelton D. Caruthers, Samuel A. Wickline, and Gregory M. Lanza. *Curr. Opin. Biotech.*, **18**(1), 26–30, 2007.

[172] Jeffry G. Weers. *J. Fluorine Chem.*, **64**(1-2), 73–93, 1993.

[173] Margherita Rossi. (Springer Berlin Heidelberg,). chapter 27, pages 229–239. 1 edition, 2007.

[174] Anne M. Neubauer, Shelton D. Caruthers, Franklin D. Hockett, Tillman Cyrus, J. David Robertson, J. Stacy Allen, Todd D. Williams, Ralph W. Fuhrhop, Gregory M. Lanza, and Samuel A. Wickline. *J. Cardiovasc. Magn. Reson.*, **9**(3), 565–573, 2007.

[175] Lin Yang and Huey W. Huang. *Science*, **297**(5588), 1877–1879, 2002.

[176] Elizabeth J. Bolen and Peter W. Holloway. *Biochemistry*, **29**(41), 9638–9643, 1990.

[177] Richard D. Chambers, Graham Sandford, and Aneela Shah. *Synthetic Commun.*, **26**(10), 1861–1866, 1996.

[178] Erik Lindahl and Olle Edholm. *J. Chem. Phys.*, **113**(9), 3882–3893, 2000.

[179] Andrey A. Gurtovenko. *J. Chem. Phys.*, **122**(24), 244902+, 2005.

[180] Seokmin Shin, Nancy Collazo, and Stuart A. Rice. *J. Chem. Phys.*, **96**(2), 1352–1366, 1992.

[181] Arvind Hariharan and Jonathan G. Harris. *J. Chem. Phys.*, **101**(5), 4156–4165, 1994.

[182] Shengting T. Cui, J. Ilja Siepmann, Hank D. Cochran, and Peter T. Cummings. *Fluid Phase Equilibr.*, **146**(1-2), 51–61, 1998.

[183] William L. Jorgensen, David S. Maxwell, and Julian Tirado-Rives. *J. Am. Chem. Soc.*, **118**(45), 11225–11236, 1996.

[184] Kirk A. Peterson, Detlev Figgen, Erich Goll, Hermann Stoll, and Michael Dolg. *J. Chem. Phys.*, **119**(21), 11113–11123, 2003.

[185] Jean-Paul Ryckaert and André Bellemans. *Faraday Discuss. Chem. S.*, **66**, 95–106, 1978.

[186] Brent H. Besler, Kenneth M. Merz, and Peter A. Kollman. *J. Comput. Chem.*, **11**(4), 431–439, 1990.

[187] Tobias Gregor, Gert Schmalisch, Wolfram Burkhardt, Hans Proquitté, Roland R. Wauer, and Mario Rüdiger. *Intens. Care Med.*, **29**(8), 1354–1360, 2003.

[188] Nicholas S. Faithfull and Jeffry G. Weers. *US Patent 5655521*, August 1997.

[189] Weiping Song, Peter J. Rossky, and Mark Maroncelli. *J. Chem. Phys.*, **119**(17), 9145–9162, 2003.

[190] Gaëlle Henneré, Patrice Prognon, Françoise Brion, and Ioannis Nicolis. *Chem. Phys. Lipids*, **157**(2), 86–93, 2009.

[191] R. Jay Mashl, H. Larry Scott, Shankar Subramaniam, and Eric Jakobsson. *Biophys. J.*, **81**(6), 3005–3015, 2001.

[192] Kalina Hristova, Christopher E. Dempsey, and Stephen H. White. *Biophys. J.*, **80**(2), 801–811, 2001.

[193] See-Wing Chiu, Mark M. Clark, V. Balaji, Shankar Subramaniam, H. Larry Scott, and Eric Jakobsson. *Biophys. J.*, **69**(4), 1230–1245, 1995.

[194] Herman J. C. Berendsen, James P. M. Postma, Wilfred F. van Gunsteren, and Jan Hermans. (D. Reidel Publishing Company,). pages 331–342. 1981.

[195] George A. Kaminski, Richard A. Friesner, Julian Tirado-Rives, and William L. Jorgensen. *J. Phys. Chem. B*, **105**(28), 6474–6487, 2001.

[196] Tom Darden, Darrin York, and Lee Pedersen. *J. Chem. Phys.*, **98**(12), 10089–10092, June 1993.

[197] Michele Parrinello and Aneesur Rahman. *J. Appl. Phys.*, **52**(12), 7182–7190, 1981.

[198] William G. Hoover. *Phys. Rev. A*, **31**(3), 1695–1697, 1985.

[199] Berk Hess, Henk Bekker, Herman J. C. Berendsen, and Johannes G. E. M. Fraaije. *J. Comput. Chem.*, **18**(12), 1463–1472, 1997.

[200] Alan Grossfield and Daniel M. Zuckerman. *Annu. Rep. Comput. Chem.*, **5**, 23–48, 2009.

[201] Norbert Kučerka, Stephanie Tristram-Nagle, and John Nagle. *J. Memb. Biol.*, **208**(3), 193–202–202, 2006.

[202] Balázs Jójárt and Tamás A. Martinek. *J. Comput. Chem.*, **28**(12), 2051–2058, 2007.

[203] Frederic Gerber, Marie P. Krafft, Thierry F. Vandamme, Michel Goldmann, and Philippe Fontaine. *Biophys. J.*, **90**(9), 3184–3192, 2006.

[204] Michael Patra, Emppu Salonen, Emma Terama, Ilpo Vattulainen, Roland Faller, Bryan W. Lee, Juha Holopainen, and Mikko Karttunen. *Biophys. J.*, **90**(4), 1121–1135, 2006.

[205] Andrey A. Gurtovenko and Ilpo Vattulainen. *J. Chem. Phys.*, **130**(21), 215107+, 2009.

[206] Jonathan N. Sachs, Paul S. Crozier, and Thomas B. Woolf. *J. Chem. Phys.*, **121**(22), 10847–10851, 2004.

[207] Alexey S. Ladokhin and Paul H. Holloway. *Biophys. J.*, **69**(2), 506–517, 1995.

[208] Svetlana Baoukina, Luca Monticelli, H. Jelger Risselada, Siewert J. Marrink, and D. Peter Tieleman. *Proceedings of the National Academy of Sciences*, **105**(31), 10803–10808, 2008.

[209] Cameron Laing, Svetlana Baoukina, and D. Peter Tieleman. *Phys. Chem. Chem. Phys.*, **11**(12), 1916–1922, 2009.

[210] Hiroki Yokoyama, Hiromichi Nakahara, Takahiro Nakagawa, Satoshi Shimono, Kunihiko Sueishi, and Osamu Shibata. *J. Colloid Interf. Sci.*, **337**(1), 191–200, 2009.

[211] Marie P. Krafft. *Adv. Drug Deliver. Rev.*, **47**(2-3), 209–228, 2001.

[212] Zhao-xiong Zhou, Bai-gen Zhang, Hao Zhang, Xiao-zhong Huang, Ya-li Hu, Li Sun, Xiao-min Wang, and Ji-wei Zhang. *Acta Pharmacologica Sinica*, **30**(11), 1577–1584, 2009.

[213] Dipanjan Pan, Gregory M. Lanza, Samuel A. Wickline, and Shelton D. Caruthers. *Eur. J. Radiol.*, **70**(2), 274–285, 2009.

[214] I. N. Kuznetsova. *Pharmaceutical Chemistry Journal*, **37**(8), 415–420, 2003.

[215] Jean G. Riessa and Marie P. Krafft. *Biomaterials*, **19**(16), 1529–1539, 1998.

[216] Niv Papo and Yechiel Shai. *Biochemistry*, **42**(31), 9346–9354, 2003.

[217] N. Lavignac, M. Lazenby, J. Franchini, P. Ferruti, and R. Duncan. *International Journal of Pharmaceutics*, **300**(1-2), 102–112, 2005.

[218] Sun-Joo Lee, Brett Olsen, Paul H. Schlesinger, and Nathan A. Baker. *The journal of physical chemistry. B*, **114**(31), 10086–10096, 2010.

[219] C. Dempsey. *Biochimica et Biophysica Acta (BBA) - Reviews on Biomembranes*, **1031**(2), 143–161, 1990.

[220] H. Raghuraman and A. Chattopadhyay. *Biochimica et Biophysica Acta (BBA) - Biomembranes*, **1665**(1-2), 29–39, 2004.

[221] Wolfgang Kabsch and Christian Sander. *Biopolymers*, **22**(12), 2577–2637, 1983.

[222] Alexey Ladokhin. *Biophys. J.*, **76**(2), 946–955, 1999.

[223] H. Tran and R. Pappu. *Biophys. J.*, **91**(5), 1868–1886, 2006.

[224] Horst Vogel. *Biochemistry*, **26**(14), 4562–4572, 1987.

[225] H. Vogel and F. Jahnig. *Biophysical Journal*, **50**(4), 573–582, 1986.

[226] Seiichiro Tanizaki, Jacob Clifford, Brian D. Connelly, and Michael Feig. *Biophysical Journal*, **94**(3), 747–759, 2008.

[227] Danilo Roccatano, Giorgio Colombo, Marco Fioroni, and Alan E. Mark. *Proceedings of the National Academy of Sciences of the United States of America*, **99**(19), 12179–12184, September 2002.

[228] H. Mozsolits. *Biochimica et Biophysica Acta (BBA) - Biomembranes*, **1512**(1), 64–76, 2001.

[229] Amina S. Woods. *Journal of Proteome Research*, **3**(3), 478–484, 2004.

[230] Steve Ludtke, Ke He, and Huey Huang. *Biochemistry*, **34**(51), 16764–16769, 1995.

[231] Fang-Yu Chen, Ming-Tao Lee, and Huey W. Huang. *Biophysical Journal*, **84**(6), 3751–3758, 2003.

[232] Ming-Tao Lee, Wei-Chin Hung, Fang-Yu Chen, and Huey W. Huang. *Proceedings of the National Academy of Sciences*, **105**(13), 5087–5092, 2008.

[233] H. Raghuraman and Amitabha Chattopadhyay. *Biophysical Journal*, **87**(4), 2419–2432, 2004.

[234] Ming-Tao Lee, Fang-Yu Chen, and Huey W. Huang. *Biochemistry*, **43**(12), 3590–3599, 2004.

[235] S. E. Blondelle and R. A. Houghten. *Peptide Research*, **4**(1), 12–18, 1991.

[236] Gregory M. Lanza, Kirk D. Wallace, Michael J. Scott, William P. Cacheris, Dana R. Abendschein, Donald H. Christy, Angela M. Sharkey, James G. Miller, Patrick J. Gaffney, and Samuel A. Wickline. *Circulation*, **94**(12), 3334–3340, 1996.

[237] Alexey S. Ladokhin and Stephen H. White. *J. Mol. Biol.*, **285**(4), 1363–1369, 1999.

[238] Megan M. Kaneda, Yo Sasaki, Gregory M. Lanza, Jeffrey Milbrandt, and Samuel A. Wickline. *Biomaterials*, **31**(11), 3079–3086, 2010.

[239] N. R. Soman, J. N. Marsh, G. M. Lanza, and S. A. Wickline. *Nanotechnology*, **19**(18), 185102+, 2008.

[240] M. M. Kozlov and V. S. Markin. *Biofizika*, **28**(2), 242–247, 1983.

[241] Yonathan Kozlovsky and Michael M. Kozlov. *Biophysical Journal*, **82**(2), 882–895, 2002.

[242] Dina Mirjanian, Allison N. Dickey, Jan H. Hoh, Thomas B. Woolf, and Mark J. Stevens. *The Journal of Physical Chemistry B*, **114**(34), 11061–11068, 2010.

[243] E. Egberts and H. J. C. Berendsen. *The Journal of Chemical Physics*, **89**(6), 3718–3732, 1988.

[244] Volker Knecht and Siewert-Jan Marrink. *Biophys. J.*, **92**(12), 4254–4261, 2007.

[245] C. G. Brouillette, J. P. Segrest, T. C. Ng, and J. L. Jones. *Biochemistry*, **21**(19), 4569–4575, 1982.

[246] Sascha Martens, Michael M. Kozlov, and Harvey T. McMahon. *Science*, **316**(5828), 1205–1208, 2007.

[247] Enfu Hui, Colin P. Johnson, Jun Yao, Mark M. Dunning, and Edwin R. Chapman. *Cell*, **138**(4), 709–721, 2009.

[248] Kathryn C. Crowder, Michael S. Hughes, Jon N. Marsh, Alejandro M. Barbieri, Ralph W. Fuhrhop, Gregory M. Lanza, and Samuel A. Wickline. *Ultrasound Med. Biol.*, **31**(12), 1693–1700, 2005.

[249] J. Killian. *Biochimica et Biophysica Acta (BBA) - Reviews on Biomembranes*, **1376**(3), 401–415, November 1998.

[250] V. Malinin. *Biophysical Journal*, **82**(4), 2090–2100, 2002.

[251] L. Chernomordik, G. Melikyan, and Y. Chizmadzhev. *Biochimica et Biophysica Acta (BBA) - Reviews on Biomembranes*, **906**(3), 309–352, 1987.

[252] L. Chernomordik, M. Kozlov, G. Melikyan, I. Abidor, V. Markin, and Y. Chizmadzhev. *Biochimica et Biophysica Acta (BBA) - Biomembranes*, **812**(3), 643–655, 1985.

[253] Leonid V. Chernomordik and Michael M. Kozlov. *Nature Structural & Molecular Biology*, **15**(7), 675–683, 2008.

[254] J. G. Weers, Y. Ni, T. E. Tarara, T. J. Pelura, and R. A. Arlauskas. *Colloids and Surfaces A: Physicochemical and Engineering Aspects*, **84**(1), 81–87, 1994.

[255] Jeffry G. Weers and Rebecca A. Arlauskas. *Colloids and Surfaces B: Biointerfaces*, **33**(3-4), 265–269, 2004.

[256] J. G. Weers, J. Liu, T. Fields, P. Resch, J. Cavin, and R. A. Arlauskas. *Artificial cells, blood substitutes, and immobilization biotechnology*, **22**(4), 1175–1182, 1994.

[257] C. I. Castro and J. C. Briceno. *Artificial Organs*, **34**(8), 622–634, 2010.

[258] Yong T. Lim, Young-Woock Noh, Jee-Hyun Cho, Jung H. Han, Bang S. Choi, Jina Kwon, Kwan S. Hong, Anisha Gokarna, Yong-Hoon Cho, and Bong H. Chung. *Journal of the American Chemical Society*, **131**(47), 17145–17154, 2009.

[259] T. L. Hwang, Y. K. Lin, C. H. Chi, T. H. Huang, and J. Y. Fang. *J. Pharm. Sci.*, **98**(10), 3735–3747, 2009.

[260] Yong T. Lim, Mi Y. Cho, Ji-Hyun Kang, Young-Woock Noh, Jee-Hyun Cho, Kwan S. Hong, Jin W. Chung, and Bong H. Chung. *Biomaterials*, **31**(18), 4964–4971, 2010.

[261] C. Fraker and C. L. Stabler. Optimization of Perfluorocarbon Emulsions for Cellular Encapsulation. In R. Magjarevic, J. Nagel, Anthony McGoron, Chen-Zhong Li, and Wei-Chiang Lin, editors, *25th Southern Biomedical Engineering Conference*, volume 24 of *IFMBE Proceedings*, chapter 60, pages 165–166. Springer, Berlin, Heidelberg, 2009.

[262] J. Bauer, M. Zähres, A. Zellermann, M. Kirsch, F. Petrat, H. de Groot, and C. Mayer. *Journal of Microencapsulation*, **27**(2), 122–132, 2010.

[263] Jo M. M. Simons, Liselotte M. Kornmann, Koen D. Reesink, Arnold P. G. Hoeks, Maartje F. Kemmere, Jan Meuldijk, and Jos T. F. Keurentjes. *Journal of Materials Chemistry*, **20**, 3918–3923, 2010.

[264] Frédéric Gerber, Thierry F. Vandamme, and Marie P. Krafft. *Comptes Rendus Chimie*, **12**(1-2), 180–187, 2009.

[265] Berenice Venegas, Marla R. Wolfson, Peter H. Cooke, and Parkson L. Chong. *Biophysical Journal*, **95**(10), 4737–4747, 2008.

[266] Tzuhn-Yuan Lin, Wen-Huey Lin, Wayne D. Clark, Richard J. Lagow, Steven B. Larson, Stanley H. Simonsen, Vincent M. Lynch, Jennifer S. Brodbelt, Simin D. Maleknia, and Chien-Chung Liou. *Journal of the American Chemical Society*, **116**(12), 5172–5179, 1994.

[267] Raquel Díaz-López, Nicolas Tsapis, and Elias Fattal. *Pharm. Res.*, **27**(1), 1–16, 2009.

[268] Anne M. Neubauer, Jacob Myerson, Shelton D. Caruthers, Franklin D. Hockett, Patrick M. Winter, Junjie Chen, Patrick J. Gaffney, J. David Robertson, Gregory M. Lanza, and Samuel A. Wickline. *Magn. Reson. Med.*, **60**(5), 1066–1072, 2008.

[269] Peter Caravan, Christian T. Farrar, Luca Frullano, and Ritika Uppal. *Constrat Media Mol. I.*, **4**(2), 89–100, 2009.

[270] Siewert J. Marrink, Alex H. de Vries, Thad Harroun, John Katsaras, and Stephen R. Wassall. *Journal of the American Chemical Society*, **130**(1), 10–11, 2008.

[271] Edward K. Watkins and William L. Jorgensen. *J. Phys. Chem. A*, **105**(16), 4118–4125, 2001.

[272] Thomas Steinbrecher, David L. Mobley, and David A. Case. *J. Chem. Phys.*, **127**(21), 214108+, 2007.

[273] Yuhong Zhang, Scott E. Feller, Bernard R. Brooks, and Richard W. Pastor. *J. Chem. Phys.*, **103**(23), 10252–10266, 1995.

[274] Beate Griepernau and Rainer Böckmann. *Biophys. J.*, **95**(12), 5766–5778, 2008.

[275] Justin Gullingsrud and Klaus Schulten. *Biophys. J.*, **86**(6), 3496–3509, 2004.

[276] Jacob Sonne, Flemming Y. Hansen, and Günther H. Peters. *J. Chem. Phys.*, **122**(12), 124903+, 2005.

[277] Svetlana Baoukina, Siewert J. Marrink, and D. Peter Tieleman. *Faraday Discuss.*, **144**, 393–409, 2010.